Physics – Uspekhi **61** (6) 531 – 581 (2018)

60th ANNIVERSARY OF THE BUDKER INSTITUTE OF NUCLEAR PHYSICS (BINP), SB RAS PACS numbers: 29.25.Ni, 29.27.Ac, 29.27.Fh, 29.27.Hj, **41.75.–i**, 41.75.Ak, 41.75.Cn, **41.85.–p**, 41.85.Ar., 52.50.Dg, 52.50.Gj

Studies of ion and neutral beam physics and technology at the Budker Institute of Nuclear Physics, SB RAS

Yu I Belchenko, V I Davydenko, P P Deichuli, I S Emelev, A A Ivanov, V V Kolmogorov, S G Konstantinov, A A Krasnov, S S Popov, A L Sanin, A V Sorokin, N V Stupishin, I V Shikhovtsev, A V Kolmogorov, M G Atlukhanov, G F Abdrashitov, A N Dranichnikov, V A Kapitonov, A A Kondakov

DOI: https://doi.org/10.3367/UFNe.2018.02.038305

Contents

Abstract. An overview of studies into the physics and technology of ion and neutral beams carried out at the Bunker Institute of Nuclear Physics, SB RAS since 1960 up to now is presented. These studies were initiated by Academician G I Budker for the charge-exchange injection of particles into storage rings. Subsequently, a whole series of ion sources were created and particle beams were produced for applications in accelerators and plasma devices for plasma heating and diagnostics.

Keywords: ion source, neutral beam, negative ion source, positive ion source, polarized beam, plasma source

Yu I Belchenko [1,2], **V I Davydenko** [1,2], **P P Deichuli** [1,2], **I S Emelev** [1], **A A Ivanov** [1,2], **V V Kolmogorov** [1,2], **S G Konstantinov** [1], **A A Krasnov** [1], **S S Popov** [1], **A L Sanin** [1,2], **A V Sorokin** [1], **N V Stupishin** [1,2], **I V Shikhovtsev** [1,2], **A V Kolmogorov** [1], **M G Atlukhanov** [1], **G F Abdrashitov** [1], **A N Dranichnikov** [1], **V A Kapitonov** [1], **A A Kondakov** [1]

[1] Budker Institute of Nuclear Physics, Siberian Branch of the Russian Academy of Sciences, prosp. Akademika Lavrent'eva 11, 630090 Novosibirsk, Russian Federation
E-mail: a.a.ivanov@inp.nsk.su

[2] Novosibirsk State University, ul. Pirogova 2, 630090 Novosibirsk, Russian Federation
E-mail: i.s.emelev@inp.nsk.su

Received 5 February 2018
Uspekhi Fizicheskikh Nauk **188** (6) 595 – 650 (2018)
DOI: https://doi.org/10.3367/UFNr.2018.02.038305
Translated by Yu V Morozov; edited by A Radzig

1. Introduction

Work on the creation of ion sources began at the Institute of Nuclear Physics, SB RAS — now Budker Institute of Nuclear Physics (BINP) — on the initiative of G I Budker and was conducted at the first stage under the guidance of G I Dimov. It was initially designed to develop the sources of negative ion beams for charge-exchange injection of particles, which would be able to provide the maximum intensity of proton accelerators and storage rings. In 1959, G I Budker proposed the charge-exchange method [1], independently of L Alvarez (USA). This technique makes possible high-efficiency injection during a practically unlimited number of turns. Moreover, it allows multiple reinjections of the beam into one and the same single-turn element of the phase space volume of the accelerating ring, which is impossible to do by other methods

due to limitations imposed by Liouville's theorem [2, 3]. To obtain maximum proton current in an accelerator, it is necessary not only to inject the required number of particles but also to ensure their most favorable distribution in the phase space volume of the accelerating ring. These advantages of the charge-exchange method permit the desired distribution of the particles in the phase volume to be reached with a gradual increase in density within the entire volume by multiple scanning of the injected beam across it.

Both hydrogen molecular ion beams and negative ion beams can be utilized for charge-exchange injection. The hydrogen negative ion beams are more convenient to use since they allow avoiding a reduction in the energy of particles as they are captured in the accelerator. At the time when these studies were initiated at BINP, negative ion beam intensity was altogether insufficient for application in the charge-exchange injection scenario. The negative ion beams obtained by charge exchange of protons from an ion source in the 1960s had currents of up to 200 μA [4]. To recall, beam currents of proton sources (most often plasmatrons or duoplasmatrons) amounted to 1.5 A, while currents of high-frequency sources ranged 100–300 mA [5], significantly restricting the potential of the charge-exchange method due to rather small coefficients of proton transformation into negative ions in gas targets (2%) or targets from metal vapors (8%) within the required particle energy range.

Studies on direct extraction of negative ions from ion sources for gaining proton beams were just beginning at that time. For example, experiments on negative ion extraction from duoplasmatron plasma were carried out at the Los Alamos National Laboratory (USA) [6]. They revealed that the maximum current can be drawn from the periphery of the plasma column with an enhanced density of negative ions [7]. The characteristic magnitude of the extracted negative ion currents was a few milliamperes. Under these conditions, BINP set about developing the charge-exchange technique, which required negative ion beams of higher quality and intensity. A number of negative ion sources were created based on direct extraction of negative ions from a gas-discharge plasma having parameters as good as those of the then best devices in the world. But the most promising results were obtained with the implementation of a charge-exchange source of negative ions having an originally designed arc source of the plasma, modified later to develop powerful proton beams. To obtain quiescent dense plasma with an almost 100% degree of ionization, a high-current discharge in the diaphragmed channel was used in this source. Its main advantage was a high density of ion current combined with low ion transverse temperature in the plasma emitter, allowing high-brightness beams to be produced. Thereafter, the intense proton beam was converted in the gas target to a beam of negative ions. The results of research into ion sources intended for charge-exchange injection are discussed in Section 2. It might be added that an overview of the data obtained in the early work on the development of ion sources for charge-exchange injection can be found in Ref. [8].

Further experiments aimed at optimizing the characteristics of proton sources for charge-exchange injection were stimulated by the construction of the BINP ambipolar plasma trap [9]. To create and maintain plasma in the trap, powerful neutral beam injectors based on positive ions were designed [10]. Plasma emitters with a plasma jet expanding from the arc generator were used in these injectors; part of the jet was reflected from the peripheral magnetic field while expanding and thereby made the emissive surface uniform. Ion beams weakly divergent from the surface of the plasma emitter were formed employing four-electrode multislit ion-optical systems with wire grids. In the course of time this work was continued to enhance beam power and duration. To produce long-duration beams, plasma emitters were created based on the utilization of an induction radio-frequency (RF) discharge. In addition, large three- and four-electrode multi-aperture ion-optical systems with ballistic beam focusing were developed. Such focusing made it possible to inject powerful beams of fast atoms through the narrow input ports of modern controlled fission facilities to heat plasma. Results of this work are presented in Section 3.

Special charge-exchange injectors of atomic beams with unique emittance, atom flux density in the beam focus region, and beam-current time modulation parameters of diagnostic value were developed at BINP [11–13]. In the preceding period, beams of powerful injectors for plasma heating had been utilized with rare exceptions for diagnostic purposes (see, for instance, Ref. [14]). BINP-created diagnostic injectors allowed meeting perhaps for the first time to the full extent the specific requirements placed on diagnostic beams of atoms [15]. BINP diagnostic injectors have no equivalent anywhere in the world; they are widely used in various setups for active corpuscular diagnostics in many up-to-date facilities with magnetic confinement of high-temperature plasma. Results of the recent BINP research in this field are presented in Section 4.

In 1971–1973, a unique plasma-surface method for producing intense negative ion beams was invented and developed at BINP. In this way, a new research area was opened up to deal with a variety of ion sources in modern charge-exchange injection systems for accelerators and storage rings. The method is based on the extraction from a plasma of negative ions emitted from the electrode surfaces bombarded by a flux of particles of gas-discharge plasma and their shaping into a negative ion beam [16]. In this case, the negative ions are effectively produced due to the capture of electrons from the electrodes with a lowered work function at electron affinity levels of sputtered and reflected particles [17]. Beams of H^- ions with a current of up to 1 A and a pulse duration of around 1 ms were obtained at an early stage of experiments. The emission current density of H^- ions was brought to 4 A cm^{-2}. Results of these studies conducted at BINP are reported in Section 5.

Special attention in this section is also given to work concerned with a rise in the current extracted from negative ion sources. This research area is related to hot plasma physics and controlled fusion (CF). Large reactor-scale facilities require high-energy neutral beams (of order 1 MeV), which are impossible to generate using positive ion sources due to the low efficiency of neutralization of positive ion beams in the range of energies higher than 120 keV for deuterium.

Special conversion targets are needed for efficient neutralization of accelerated negative ion beams. BINP researchers have been developing such targets since the 1970s. To this effect, G I Dimov proposed to adapt a plasma neutralizer [3]. These pioneering studies by BINP scientists were far ahead of their time. Relevant publications by other authors appeared many years after the first successful experiments of our researchers (see, for instance, Refs [18, 19]). It is indicative in this context that gas targets capable of low-efficiency neutralization ($\sim 60\%$) are likely to be used in the construc-

tion of the International Thermonuclear Experimental Reactor (ITER). At the same time, the plasma neutralizer proposed in Ref. [20] and created at BINP may have an efficiency of $\sim 85\%$. The main results of BINP investigations into high-efficiency conversion targets for high-energy negative ion beams are discussed in Section 6, which reports, in addition, on BINP research concerning the photon neutralizer allowing 100% conversion to be reached. The proposed and experimentally implemented design of the photon neutralizer has advantages over neutralizers of conventional resonant design.

Readers unfamiliar with the terminology of ion source and charged-particle beam physics, wishing to gain some insight into the problems under consideration and the approaches to and methods of addressing them, are advised to look through excellent review articles [21–24].

2. Ion sources for charge-exchange injection of particles into accelerators and storage rings

The charge-exchange method of a proton capture on the accelerator track was discussed by L W Alvarez in 1951 [25]. In this method, a beam of H^-, H_2^+, H_3^+ ions or neutral H^0 atoms is injected into an accelerator or a storage ring so that it passes through a local stripping target, is converted into an ion beam, and is captured by the accelerator magnetic field. The losses in energy and particle scattering in the target during an injection pulse can be rather small, and the target might be 'removed' after the completion of injection to rule out its influence on the particle movement. Importantly, new portions of particles enter the phase space already filled with captured particles; due to this, the brightness of the accumulated beam can be a few orders of magnitude greater than that of the injected one, and limitations imposed by Liouville's theorem [3] prove to be overcome.

It is especially expedient to employ for charge-exchange injection the high-energy hydrogen negative ion beams to ensure that the captured ions have an energy equal to the injection energy. Then, the negative ion beam can be neutralized with a sufficiently high efficiency, if appropriate, in a gas target (see below). In the 1950s–1960s, however, methods for the generation of negative ions were highly inefficient and allowed studying only particle's orbits in a stationary magnetic field without appreciable accumulation of intense beams. Some later authors independently emphasized the attractiveness of proton charge-exchange injection into accelerators (see, for instance, Refs [1, 3] and references cited therein).

Purposeful investigations into proton charge-exchange injection into accelerators was initiated at BINP by G I Budker in 1960 in the framework of the colliding antiproton–proton beam (VAPP) project [26, 27]. Because highly intense beams were to be accumulated, the development of the methods for producing intense hydrogen negative ion beams constituted an important part of the program.

The first sources installed on the injector of the BINP proton storage ring (1.5-MeV Van de Graaff accelerator) were plasma sources capable of extracting hydrogen negative ions from an RF discharge. Early experiments used an RF source of hydrogen negative ions with a 21-μA current and 400-W power [28]. The extraction voltage reached 12 kV. A specific feature of the source was the blocking of secondary electrons in the charge-exchange channel of the 250–300-V extracting electrode. This source mounted on the 1.5-MeV Van de Graaff accelerator allowed a hydrogen negative ion beam with a 12-μA current [29] to be obtained. The beam was introduced into the storage ring in the form of 1–300-μs pulses generated with the aid of a shut-off capacitor mounted in the ion guide. The focused beam was then injected into a neutralizing gas target having a transverse size of 3–4 mm and a spread angle of 2×10^{-3} rad; the target was prepared in the shape of a flow tube 5 cm in length and 1 cm in diameter with diaphragms and differential pumping. The tube was fed with 1-ms gas puffs through an electromagnetic valve. The hydrogen atom beam was sent from the target into the orbit with an accuracy of ± 1 mm and $\pm 2 \times 10^{-3}$ rad in terms of position and angle, respectively. Energy stability reached $\pm 0.2\%$.

For achieving maximum atomic beam escape, negative ion neutralization cross sections were measured by mass-spectrometric technique in certain gases (H_2, N_2, C_2H_2, C_3H_8, CO_2, SF_6, CCl_2F_2) at an energy of 1–1.5 MeV. It turned out that the maximum atomic beam escape amounted to 50–55% and showed only a weak dependence on the kind of gas and energy. Further experiments made use of a neutralizing target with hydrogen or carbon dioxide (optimal layer thickness of 2.5×10^6 and 3×10^{15} molecules per cm^2, respectively). Thereafter, an arc source of negative ions with a 1-mA current in a 1-ms pulse was installed on the accelerator to accumulate high currents. As a result, a negative ion beam with an 800-μA current was produced from the accelerator with this ion source, allowing 10^{12} particles (current ~ 1 A) to be collected in the orbit of the device.

Further charge-exchange injection experiments took advantage of a plasma source with reflective discharge and ion beam current of 8 mA [30]; then, a charge-exchange source of H^- ions [31] with an ion beam current of up to 15 mA was employed, in which a primary beam of positive ions was produced by the high-current source with a diaphragmed arc-discharge channel and multislit extraction system developed under the guidance of G I Dimov. Modernization of the charge-exchange source of negative ions permitted the current to be increased to 20 mA [32] and the beam quality to be improved. Later on, it was made as high as 76 mA [33]. Normalized emittance of a beam with a 50-mA current reached $2 \times 10^{-4} - 2.5 \times 10^{-5}$ cm rad in different directions. The modernized Dimov–Roslyakov source was exploited for charge-exchange injection for many years [8, 34]; its design provided a basis for a series of atomic injectors, described in Section 3.

2.1 Pulsed charge-exchange source of negative ions

An appreciable increase in the negative ion beam current for injection into a storage ring was achieved (see above) with the aid of a pulsed charge-exchange source of hydrogen negative ions [32], shown schematically in Fig. 1. Its main components include a pulsed arc plasma generator, a small-structure three-electrode ion-optical system, and a pulsed charge-exchange hydrogen target. The ion-optical system (IOS) had wire pitch $s = 0.3$ mm, interelectrode distance $d = 2.4$ mm with the wire diameter near the plasma grid of 0.05 mm, and 0.05-mm thick and 0.5-mm high plates close to a louvered extraction grid. The plasma emission diameter (10–22.5 mm) was set by the diaphragm fitted on a plasma grid. At an extracting voltage of 13 kV, the source made it possible to produce a 10^{-4} s proton beam with a 3 A current. After charge exchange in the equilibrium hydrogen target, the H^- ion beam intensity reached 54 mA and normalized beam

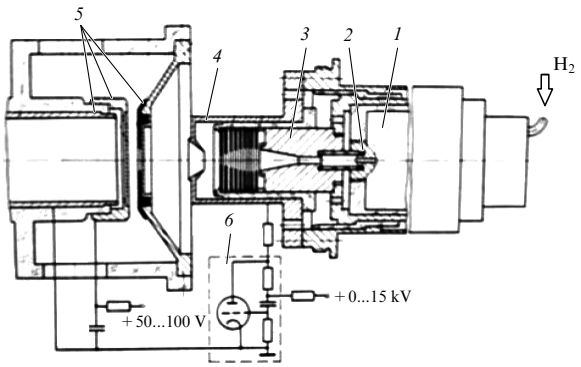

Figure 1. Pulsed charge-exchange source of hydrogen negative ions: *1* is the gas valve, *2* — ignitor, *3* — cathode, *4* — anode, *5* — electrodes of the ion-optical system, and *6* — thyratron protection from breakdowns.

emittance at the 0.9 intensity level came to 0.2 and 0.025 mrad cm in the directions perpendicular and parallel to the grid threads, respectively.

A thyratron circuit for the protection of extracting gap against breakdowns was applied in the source (*6* in Fig. 1). The protective scheme restricting energy release in the IOS prevented the burning of grid wires and markedly reduced high-voltage conditioning time for the extracting gap.

This source was deployed to obtain hydrogen and helium negative ion beams by charge exchange in sodium vapors [33]. It produced hydrogen, deuterium, and helium ion beams with 76, 100, and 12 mA currents, respectively. Moreover, the data available prior to the experiments on the yield of hydrogen negative ions resulting from proton charge exchange were updated and the energy dependence of the yield during charge exchange of hydrogen atoms in sodium vapors was documented.

This pulsed source of hydrogen negative ions with charge exchange in the hydrogen target was employed in the injector of the EG-1.5 accelerator (EG — electrostatic generator) [32] for charge-exchange injection of protons into the storage ring [33]. The injector formed an H^- beam with an energy of 1 MeV, current of 20 mA, and duration of 2×10^{-4} s. The total beam charge of 4×10^{-6} C was consistent with the maximum potential of the electrostatic accelerator front electrode used in the experiment and allowable by the pulsed stabilization scheme [30].

Figure 2 shows the layout of the source. It is enclosed in chamber *6* galvanically coupled to the high-voltage electrode of the EG-1.5 accelerator. Pulsed arc plasma generator *1* with the potential of the chamber is separated from the main chamber volume by a partition to smooth pulsed hydrogen loading of the ion tract and the accelerating tube. Hydrogen consumption in the plasma source is 3×10^{17} molecules per pulse. The buffer volume with the plasma source is evacuated for ≈ 0.1 s through a special tube after each pulse. Ion-optical system 2 forms a proton beam from the plasma with a 16×18-mm oval cross section and 12 keV of energy. Protons enter the charge-exchange tube into which hydrogen is additionally introduced (2×10^{16} molecules per pulse) through electromagnetic valve *3*. The beam escaping from the charge-exchange tube is separated by permanent magnet *4* that has the tube potential. Apertures of the separating magnet of the source and the analyzing magnet at the exit from the accelerator are minimal along the magnetic field. To facilitate the passage of the beam through the magnets, grid

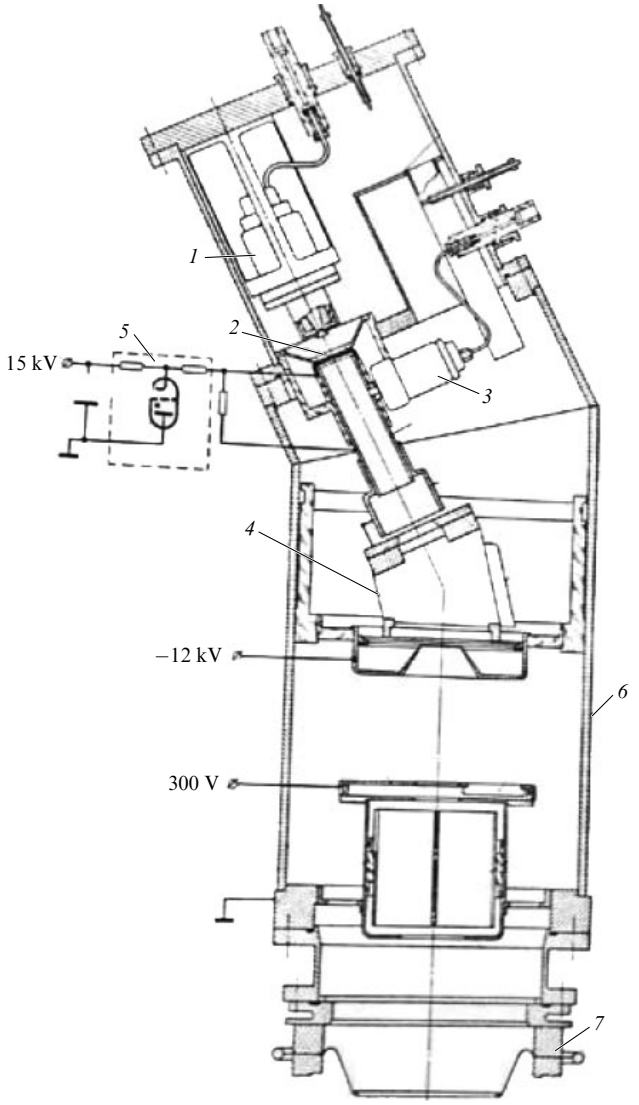

Figure 2. Layout of the ion source at the high-voltage electrode of the EG-1.5 accelerator: *1* is the plasma generator, *2* — IOS, *3* — valve, *4* — magnet, *5* — thyratron-based protection circuit against breakdowns, *6* — chamber casing, and *7* — high-voltage electrode of the accelerator.

wires in the source are arranged parallel to the magnetic field of the separating magnet placed in the plane of the analyzing magnet.

The diaphragm at the exit from the magnet and the special visor serve to receive beam neutral and positive components carrying a 1.5 A current. Further in the gap between the diaphragms the H^- ions are additionally accelerated to 24 keV and delivered into accelerating tube *7* through the guard cylinder containing the electrostatic system of deflection plates, which permits correcting the angles at which the beam enters the tube.

The large distance separating elements of the source from the accelerating tube, together with the good shielding of its electrostatic field by the guide cylinder, illuminates breakdowns at the source elements and overvoltage in its power supply circuit caused by discharges in the accelerating tube.

The implementation of the tandem ion acceleration scheme in the source made possible simplification of the power supply circuit and facilitated its ion-optical matching with the accelerating tube. Beam focusing in the source tract was reduced to a minimum, and the crossover of the beam

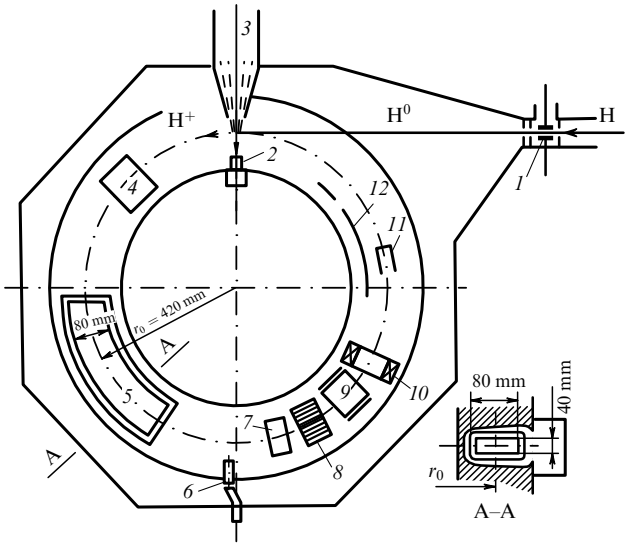

Figure 3. Schematic diagram of a device for the study of charge-exchange injection: *1* is the first stripping target, *2* — supersonic jet nozzle, *3* — jet collector, *4* — circular pickup electrode, *5* — drift tube of high-frequency acceleration, *6* — collimator of the beam light profilometer, *7* — ionization beam intensity measuring device, *8* — ionization profilometer, *9* — pickup monitor, *10* — Rogowski loop, *11* — Faraday cup, and *12* — deflector for suppressing the electron–proton instability.

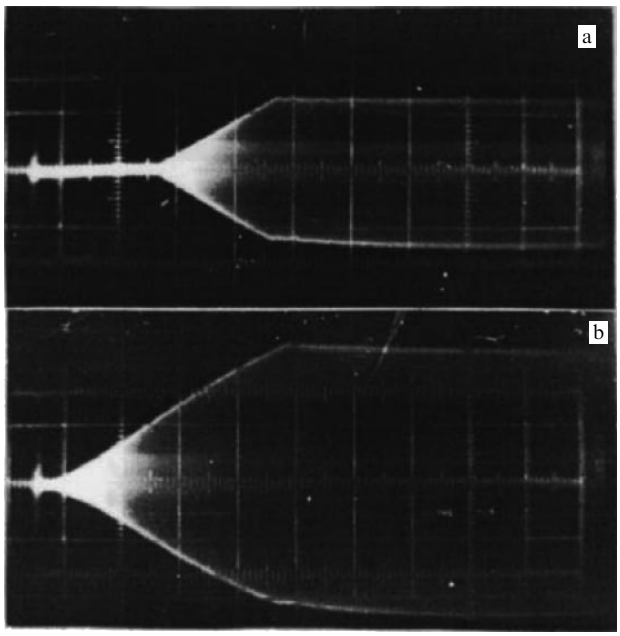

Figure 4. Pickup signal for proton accumulation during 500 (a) and 1000 (b) turns [1].

with a current of 20 mA and energy of 1 MeV was located 2 m from the output end of the accelerating tube, in agreement with its theoretical position and taking into account the beam space charge. The phase volume of the H^- beam at the exit from the accelerator was 0.26×0.1 mrad cm, i.e., greater than the initial one in the source. The injector was used in experiments on ring accumulation of protons with the current exceeding the space charge limit [8, 34].

2.2 Experiments on charge-exchange injection of particles into a storage ring

The charge-exchange injection of protons on the circular track of a storage ring was implemented in experiments [35–37] in 1964. Thereafter, the intensity of the proton beam accumulated by the charge-exchange method was brought to the limit in space charge [8, 38]. The BINP facility for the study of charge-exchange injection is schematically presented in Fig. 3.

The stripping target was a supersonic hydrogen jet switched on during injection. The capture efficiency reached during 2000 turns with the RF compensation for ionization losses amounted to 75% in correspondence with the separatrix area; it was reduced only by 20% during 4000 turns [39]. These experiments demonstrated for the first time the development of electron–proton instability (the so-called electron cloud effect) limiting beam intensity in meson fabrics and other large accelerators and storage rings [40], as well as its feedback-driven suppression.

The accumulated beam existed for 1–1.5 ms; then, the buildup of betatron oscillations dumped the beam from the orbit for a few dozen turns.

Later experiments had the objective of obtaining a circulating proton beam with a compensated space charge.

To suppress the negative mass effect, the electromagnet of the storage ring had strong focusing poles put on to study beam accumulation with the compensation for ionization losses by the induction field. The beam current was accumulated and saturated as horizontal and vertical losses increased. The pickup signal proportional to the circulating beam current during proton accumulation in the ring in the resonance mode is shown in Fig. 4.

The pickup of a vertical beam position recorded the growth in vertical betatron oscillation amplitude till the beam was spilt vertically [38]. This instability arising from oscillations of compensating particles in the beam potential well is fairly well described by the instability theory developed by B V Chirikov [40] for an ion-compensated electron beam. Investigations into collective effects in circulating beams with an ultimate intensity in relation to a space charge, in combination with charge-exchange injection, made it possible to create such a 'super-unequilibrium' structure as a circulating proton beam, compensated for by an electron gas, with an intensity almost an order of magnitude above the value limited by a space charge [38].

Results of investigations with the employment of the charge-exchange method for proton injection are reported in Refs [3, 41, 42]. Reference [41] presents, in addition, a comprehensive review of publications on the development of hydrogen negative ion sources in foreign laboratories.

2.3 Charge-exchange injection into magnetic traps for plasma confinement

Charge-exchange injection of powerful charged particle beams is one of the most promising methods for creating and confining plasma with thermonuclear characteristics in magnetic traps. The plasma confined in a trap plays the role of a target converting injected particles into captured ones during stationary injection. For the primary accumulation of hot plasma, the plasma guns, inductive discharges in gases, and discharges under electron cyclotron resonance (ECR) conditions, etc. have to be used [43]. One of the first applications of charge-exchange technologies in thermonuclear research (plasma accumulation in the Ogra mirror trap) was proposed by G I Budker [44] and implemented under the guidance of I N Golovin [45]. Primary plasma accumulation

was achieved through the generation of fast protons in collisions between accelerated H_2^+ ions and the residual gas. The DCX (Direct Current experiment) facility of the Oak Ridge National Laboratory (USA) was utilized to dissociate H_2^+ ions during their interaction with high-current arc gas-discharge plasma particles [46].

Later studies made use of Lorentz ionization in the magnetic field of a trap with highly excited atoms formed during charge exchange of protons in special targets [47]. The charge-exchange technology for producing hot plasma in magnetic traps was proposed many years ago [48] and has a long history of development. Taking advantage of high ion-to-atom conversion efficiency at low proton energies, injector facilities were created to generate H^0 atomic fluxes with an energy of a few dozen keV and current density of several hundred or thousand amperes per cm^2. Some injectors of hydrogen neutral beams were designed at BINP (see Section 3). They have an energy from 15 to 55 keV, beam current from 1 to 175 A, angular divergence of 10^{-2} rad, and pulse duration of $10^{-2} - 10$ s [49].

In addition, the efficient capture of particles in the trap magnetic field was achieved taking advantage of fast atomic ionization in a preliminarily created highly ionized tokamak plasma [50] or in a preliminarily injected plasma of mirror traps [51]. Charge exchange injection makes it possible to create arbitrary particle distributions over energies and in space, exert bulk effects on the state of a plasma, and maintain its current. For further progress to reactor parameters and conditions, atomic beams with an energy of at least a few hundred keV are needed. At such energies, the effectiveness of conversion of hydrogen isotope positive ions into atoms turns out to be unacceptably low (see Section 6). The sole alternative is to generate high-energy atoms from accelerated negative ions.

The closed force line configuration with the reversed magnetic field in a circulating electron beam was proposed by the American researcher N C Cristophilos for thermonuclear fusion in the 1950s and was realized by the injection of an electron beam with a current of a few dozen kiloamperes into a magnetic field [52]. In doing so, instabilities destroying the circulating beam during slow accumulation were avoided by injecting beams for which focusing by their own magnetic field was essential during injection. These findings gave an impetus to the development of thermonuclear fusion systems based on the configuration with closed magnetic force lines and circulating closed ion beams [53, 54]. It is proposed to obtain such configurations relying on charge-exchange injection, which implies conversion of well-formed H^- particle beams with a current density of several hundred or thousand amperes per cm^2 and energies of a few hundred keV. The neutral beam injectors developed at BINP for this purpose are considered in Section 3.

To conclude the present section, it is worthwhile to mention achievements reached at the initial stage of ion source research at BINP. The foregoing discussion was unconcerned about the development of surface-plasma negative ion sources for implementing projects on charge-exchange injection into accelerators and other applications. The world's first sources of this type were designed and created in BINP; they provided a basis for successful research that ended in the creation of sources with unique characteristics for modern accelerating facilities and high-energy beam injectors for controlled fusion (CF). These pioneering studies were carried out by G I Dimov's group comprising Yu I Belchenko, E D Bender, V I Davydenko, G E Derevyankin, V G Dudnikov, M E Kishinevskii, A S Kupriyanov, and other researchers. They are presented in detail in Section 5.

All that has been said before fully applies to the charge-exchange sources of negative ions discussed in the present section, whose unique characteristics were later used to design up-to-date diagnostic and heating injectors for CF research. Their main component was a high-current gas-discharge plasma source [31, 32] for creating a plasma emitter with a low ion transverse temperature and high degree of plasma ionization, approaching 100%. Moreover, precision ion optical systems with high ion current density (~ 1 A cm^{-2}) were used for the first time, which allowed taking in full measure advantage of the low temperature of plasma emitter ions for the formation of high-brightness beams (see Section 4 for details).

3. Ion sources and injectors of neutral beams for controlled fusion

The injection of powerful hydrogen or deuterium atom beams is widely used to heat and maintain plasma in magnetic confinement devices. The employment of neutral beams also makes possible the generation of plasma currents [55–58]. Today, the most commonly used energies of hydrogen isotope atomic beams for modern CF reactors lie in the range of 30–150 keV. Such beams are produced using positive ion beams accelerated to the required energy with subsequent charge exchange in a gas target. Future CF reactors will also adapt atomic beams with an energy of ~ 1 MeV that can be rather effectively generated only with putting on the negative ions.

At BINP, work aimed at creating powerful atomic injectors using positive ions in their operation has been stimulated since the 1970s by plans to heat plasma in an ambipolar atomic trap (AMBAL) [9] and a gas-dynamic trap (GDT) [59], under construction at that time.

In the first neutral beam injectors developed at BINP for plasma heating in the AMBAL and GDT facilities, ion sources Start [60–62] and INAK (Russian abbreviation for quasistationary source of neutral atoms) [63]) of identical designs were used. Their creation became possible owing to the development of ideas behind the construction of the ion source described in Section 2 [30–33]. These sources included a plasma generator built around an arc generator with a cold cathode [31, 32] highly modernized to increase plasma yield. To this effect, the magnetic field in the discharge channel was imposed to reduce plasma losses onto its walls [60, 63]. To form the large-area plasma emitter with uniform ion current density, it had an expansion chamber with a peripheral magnetic field ('magnetic wall'). The ion beam was created using a multiaperture (slotted) IOS with wire grids. Such injectors could form 0.1-s beams as powerful as a few hundred kW.

At the beginning, it was necessary to choose the IOS so as to ensure the formation of proton beams with an energy of ≈ 40 keV and emission current density of ≈ 0.5 A cm^{-2}. The application of conventional three-electrode systems encountered difficulties due to the absence of technologies for manufacturing intricately shaped electrodes. Moreover, the employment of the readily available multislit fine-structured three-electrode system was equally difficult in view of the large current and thermal loads. It called for the study of ion-optical properties of the multislit four-electrode IOS with

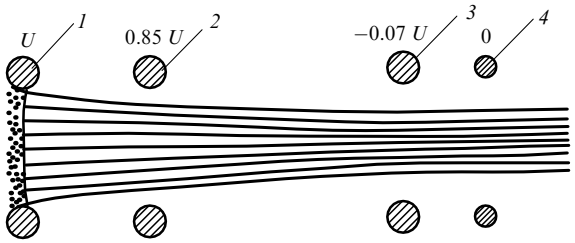

Figure 5. Schematic of four-electrode IOS: *1* is the plasma electrode, *2* — extracting electrode, *3* — accelerating electrode, *4* — grounded electrode, and *U* — plasma electrode voltage.

electrodes of a round cross section [60]. The principal variant of the elementary cell of the IOS of interest is shown in Fig. 5. Such a system differs from an ordinary three-electrode one in that the impulse directed to the central plane of the cell, necessary to make up for the summary action of the scattering output electrostatic lens and the space charge, reaches beam particles in the transverse electric field near the extracting electrode rather than at the very beginning stage of formation, i.e., close to the plasma boundary curved by the specially shaped electrode. The focusing action of the extracting electrode is analogous to the action of the cathode lens in electron optics, with each elementary cell functioning as an immersion lens [65].

To create and maintain a high-temperature plasma in the end magnetic mirror traps of the AMBAL plasma trap, two types of intense fast hydrogen atom beams were provided for. The first one was pulsed beams injected in the beginning of the device working pulse to create a hot long-lived target plasma for the main beams with a pulse duration of 200 μs, equivalent current of 50 A, and atom energy of 20 keV. The second type was represented by quasistationary beams injected during the entire working pulse to accumulate and maintain the hot plasma with a pulse duration of 0.1 s, equivalent current of 20 A, and atom energy of 25 keV. To produce such beams, a special injector was developed with charge exchange of the respective proton beams, which was further modernized for a specific application. The Start-1 experimental proton source is schematically presented in Fig. 6. The plasma in this source is generated by an arc discharge. The generator consists of a cold cathode from an aluminum–magnesium–copper alloy (D16T), a discharge channel 1 cm in diameter formed by isolated copper diaphragms, and an anode with a 9-mm hole for plasma outflow. Pulsed gas puffing into the near-cathode region through the valve [66] and delivery of the high-voltage pulse to the special electrode are followed by discharge ignition to generate a hydrogen plasma jet freely expanding at the exit from the anode hole. To facilitate plasma escape through the anode hole, its source is placed in a longitudinal magnetic field of up to 1 kOe excited by a current pulse in the solenoid. The screen from soft magnetic steel protects the expanding plasma jet region from the influence of the magnetic field. The expanding plasma jet interacts with a 50 Oe peripheral magnetic field excited by a current pulse inside a transparent toroidal coil consisting of 16 windings of insulated copper wire 2.5 mm in diameter located uniformly by the azimuth. Plasma reflection creates a spatially homogeneous plasma emitter of protons in the plane of the plasma electrode of the optical system. The nonuniformity of emission current density inside a circle with an emission diameter of 9 cm does not exceed ±5%.

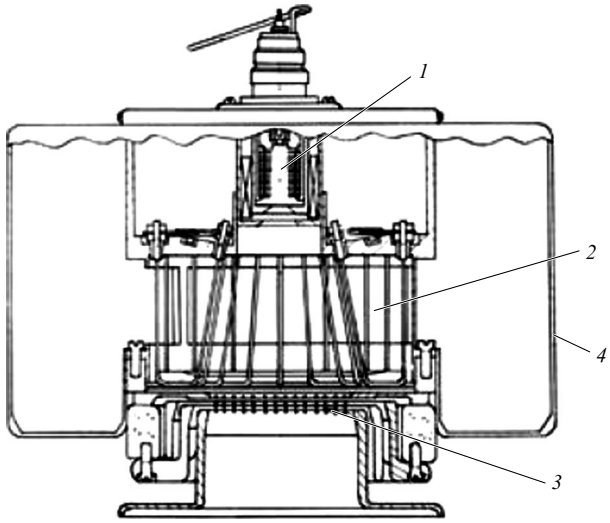

Figure 6. Start-1 proton source: *1* is the arc plasma generator, *2* — 'magnetic wall', *3* — IOS, and *4* — screen electrode.

The 37-A ion current with an ion energy of 25 keV produced in the source under optimal beam formation conditions showed $U^{3/2}$ dependence, whereas the emission current density from the plasma surface reached 0.8 A cm^{-2}. Measurements with the aid of a magnetic analyzer demonstrated that the fraction of protons in the beam amounted to 95%, with its remaining part consisting of hydrogen molecular ions H_2^+ (2%), H_3^+ (1%), and ions with masses of 12–40 (2%). Heavy ions appear to form in the emitting plasma as a result of ionization and charge exchange of gas molecules adsorbed at the plasma electrode and elements of the solenoid generating a peripheral magnetic field and knocked off by the plasma jet. The presence of impurity ions in the beam is responsible for a certain decrease in its optimal current.

The ion temperature of the plasma emitter along the IOS slits is equal to 3 eV, in excellent agreement with the measurements by a transverse velocity sensor, as described in Ref. [67]. Angular divergence of the beam across the slits is twice that along them.

The Start-1 source operated at a frequency of 0.2 Hz given by parameters of the power supply circuit. The results of research were applied to develop a commercial variant of the pulsed proton source Start-2 [61] with a beam current of 75 A, ion energy of 20 keV, and pulse duration of 250 μs. Another modernized version, Start-3, differed from its predecessor only in minor changes in the design of the arc plasma source introduced to ensure evenly timed hydrogen feeding, had a beam current duration increased to 1 ms. Later on, the INAK ion source, shown in Fig. 7, was developed [63]. Its layout is similar to that of Start type pulsed sources but takes into account the possibility of heavier thermal loads. The ion-optical system consists of four electrodes connected by eight alundum ceramic rods. It has multislit plasma, extracting, and accelerating electrodes, while the fourth (grounded) electrode has an open aperture. The slotted electrode structure is formed by molybdenum wires 1 mm in diameter placed with a 3-mm pitch in the grooves of ring mandrels. The strained wires were preliminarily annealed in a vacuum. The wires were attached to circular electrodes so that they could freely extend when heated. The plasma electrode had a tantalum plate with milled grooves deep enough to bury the wires — an analog of the Pierce electrode.

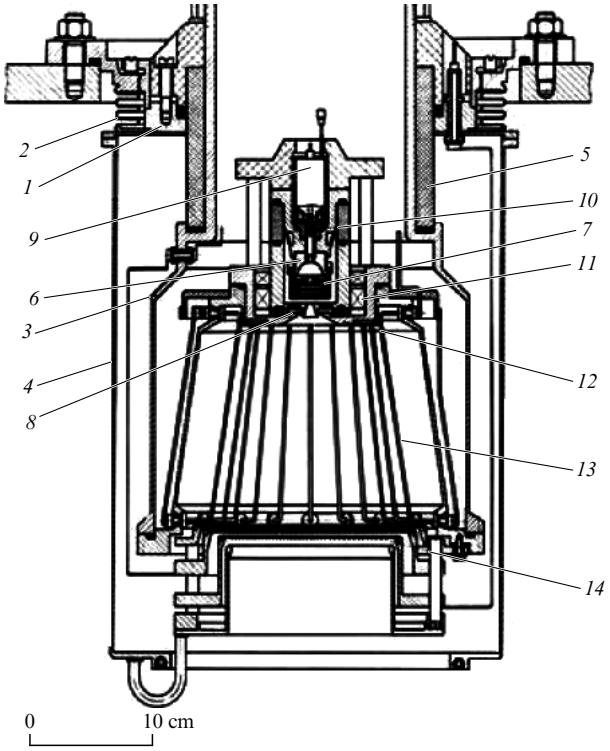

Figure 7. INAK ion source: *1* is the mounting flange, *2* — silphon, *3* — vacuum enclosure of the 'magnetic wall', *4* — screen, *5* — ceramic insulator, *6* — cathode, *7* — discharge channel, *8* — anode, *9* — gas valve, *10* — ignitor electrode, *11* — solenoid, *12* — magnetic shield, *13* — windings of the 'magnetic wall', and *14* — IOS.

When tested on an experimental bench, the quasistationary proton source produced a proton beam with the following design parameters: current of 25 A, energy of 25 keV, and duration of 0.1 s. Analysis of the beam composition showed that it largely consisted of protons (more than 90%), with the molecular ions accounting for less than 10%. The measured gas efficiency of the source was 30%.

The IF-6 injector (6-keV injector with focusing) [68] was intended to maintain ion-hot plasma in a semicusp of AMBAL-M plasma trap. The plasma emitter with a low ion transverse temperature formed by the collisionlessly expanded plasma jet was used to reduce the temperature contribution to the angular divergence of the beam produced in the ion source of this injector (Fig. 8). The beam was formed by the focusing IOS with gaps increasing along the radii. A distinctive feature of this ion source was high plasma utilization efficiency, with roughly half of the plasma jet occurring in the emission region.

The gaps between the plasma and extracting electrodes, as well as between the plasma and accelerating electrodes at the IOS axis, were 1 and 2.5 mm, respectively. They were twice that at the 7-cm peripheral radius of the IOS. The proton beam was formed by 2700 apertures 2 mm in diameter, making up a hexagonal structure with a 2.5-mm pitch. IOS electrodes were made of 0.5-mm thick tantalum; the holes in them were drilled using a precision drilling machine. The IOS was designed so that its electrodes could be heated to 400 °C.

In the experiments, the source being considered produced a pulsed proton beam with 12-A current, proton energy of 6 keV, and pulse duration of 0.2 ms. The proton beam underwent charge exchange into atoms in the pulsed charge-exchange target placed not far ($\sim$ 10 cm) from the IOS to ensure minimal beam spread under the effect of the 3 V cm^{-1} radial electric field presented in it. The atomic beam thus obtained was focused 65 cm from the source and had a diameter of 2.5 cm in the focal region at the $1/e$ level, corresponding to the integral angular divergence of 2×10^2 rad. Measurements of local angular divergence gave evidence that it amounted to $\sim 2.5 \times 10^{-2}$ rad in the central part of the beam and dropped to 1.7×10^{-2} rad at its periphery. The reduction in local angular divergence with increasing beam radius was attributed to decreased aberrations due to the widening of the gap between the IOS electrodes.

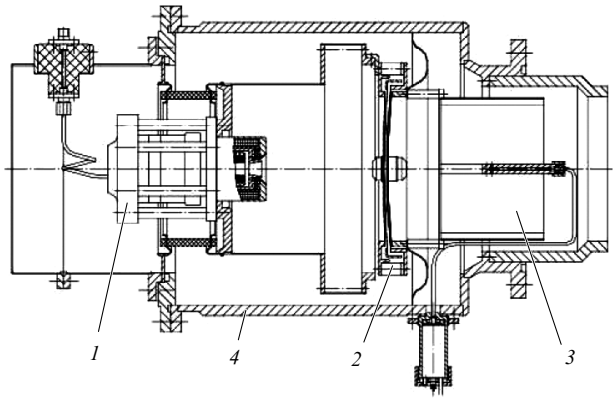

Figure 8. Ion source of IF-6 injector: *1* is the plasma generator, *2* — IOS, *3* — charge-exchange tube, and *4* — casing.

The maximum beam current in the pulsed regime amounted to 36 A at a proton energy of 14 keV. A beam with a 17-A current, proton energy of 8 keV, and pulse duration of 0.1 s was produced during quasistationary testing of the source. Later on, a variant of the ion source with a focal length of 250 cm was developed and tested. It was used to construct a diagnostic injector with an energy of 14–16 keV generating a beam with an atom flux density of up to 0.8 A cm^{-2} in the diagnostic setup using an artificial target in GDT [69].

An early version of the arc plasma generator used in the construction of the Start and INAK ion sources with a cold cathode was described in Ref. [70]. Most of the further changes in the design of plasma generators were intended to enhance their reliability and prolong the service life. The evolution of Start type ion sources from Start-1 to Start-4 reduced to the improvement of the general layout of the gas-discharge chamber as exemplified by the Start-1 and INAK injectors in Figs 6, 7. The plasma is generated in the arc discharge with a hollow hemispherical cathode in a 3-cm long cylindrical chamber 1 cm in diameter. A longitudinal magnetic field of maximum strength up to 1 kG is created in the discharge channel with the use of a special coil. The magnetic field in the plasma generator is essentially nonuniform. The magnetic field in the cathode region is practically nonexistent. The shape of the anode edge is chosen such that magnetic force lines move out from the gas-discharge channel tangentially to the anode. A screen of soft magnetic steel shields from the magnetic field the region where the plasma jet expands. The working gas is fed into both the near-anode and the near-cathode discharge regions through pulsed gas valves [66]. The discharge channel between the cathode and the anode is diaphragmed along its entire length using a set of metallic diaphragm plates under a floating potential. The plasma jet outflows through an axial hole in the anode.

Plasma yield depends on discharge current and longitudinal magnetic field strength in the discharge determined by the current in the magnetic insulation coil. Variation of the magnetic field strength allows plasma yield to be modulated by an order of magnitude at the same discharge power. The formation of the plasma emitter is described in detail in Ref. [60].

The development of injectors for plasma heating was continued in the 1990s when diagnostic injectors with ballistic beam focusing were designed. A plasma emitter based on RF discharge with a pulse duration of up to 10 s was successfully used in the Russian Diagnostic Injector (RUDI). Moreover, permanent NdFeB-magnets became available, which made it possible to generate magnetic fields to control plasma flows in the course of formation of a plasma emitter with the desired properties. Equally important was the appearance of computer codes for optimization of intricately shaped grid electrodes of the IOS and engineering codes for the calculation of electrode heating and deformation. Moreover, engineering programs became available that simplified and speeded up the design process for the development of sophisticated injector complexes. In addition, the mastering of computer-controlled machines made it possible to produce IOS for ion sources with electrodes showing a formerly unattainable accuracy and intricacy of shape. These characteristics are of special importance for triode IOS in which the shape of the plasma meniscus is essential due to its high sensitivity to minute details in the shape of the plasma electrode. Taken together, these innovations greatly promoted the development of the next generation of fast atom beam injectors for the plasma heating, which possess an enhanced beam power and duration characteristics.

The application of novel technologies started from the formation of diagnostic beams of relatively moderate power (up to 160 kW [71–73]). Thereafter, the IOS with ballistic (geometrical) focusing for ion sources of diagnostic injectors was modified to make it applicable in injectors for plasma heating by powerful focused beams of fast atoms. In the early 1990s, BINP developed an injector forming a focused hydrogen atom beam with an energy of 6 keV and a current of ≈ 20 A [68, 74]. One more injector was designed in 2001–2003 for heating plasma by a focused atomic beam with an energy of 25 keV and power of around 900 kW [75, 76]. Both devices are operated with a focused beam a few centimeters in diameter. The possibility of focusing the beam so that it can pass through (as a rule) narrow-diameter vacuum conduits of plasma facilities is of great importance for application of injectors under the real experimental conditions.

In what follows, the BINP injector developed for Madison Symmetric Torus (MST) facility (USA) with ballistic focusing of the beam for plasma heating in the reversed-field pinch experiment and the formation of a fast ion population in GDP plasma is described. A schematic of this powerful heating injector [75] is presented in Fig. 9. To have a spatially homogeneous plasma emitter, plasma reflection from a peripheral multipole magnetic field finds use. Such a field is generated by 32 permanent magnets in the form of $9 \times 12 \times 240$-mm rectangular bars. The magnetic field at the inner wall of the expander is 2 kG and decreases to 100 G upon displacing 2 cm inward. Reflection of the plasma jet from the 'magnetic wall' is responsible for a 1.5-fold increase in the plasma flux onto the emitting surface. The measured inhomogeneity of the plasma emitter does not exceed $\pm 10\%$.

IOS grids are produced from a 0.5-mm thick molybdenum plate with holes made by photoetching. Each grid has more than 3000 holes 2.5 mm in diameter disposed inside a circle with a diameter of 200 mm. The hexagonal structure period of all holes is 3.2 mm, and grid transparency reaches 53%. All electrodes have identical 150-cm radii of curvature; the focal length of the beam formed by such a system must be 120 cm, as follows from the consideration in Section 4. The accelerating electrode being a composite one, this allows effectively increasing its thickness and lowering negative voltage at the pickoff electrode to 300 V.

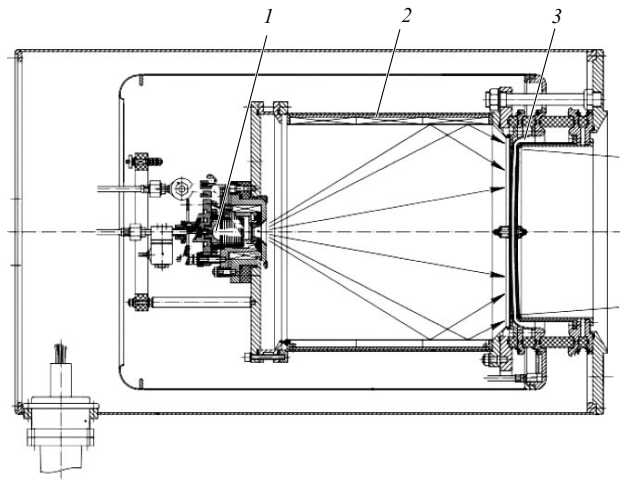

Figure 9. Ion source of MST heating injector and GDP: *1* is the plasma generator, *2* — permanent magnets, and *3* — IOS.

A proton beam with a 50-A current, a particle energy of 25 keV, and pulse duration of 3 ms was obtained when testing the source. The pulse length was measured by a high-voltage modulator. Radial profiles of the atom flux in the beam were determined at different distances from the source using a line of secondary emission detectors and a mobile calorimeter. Figure 10 presents an atomic flux density profile measured at

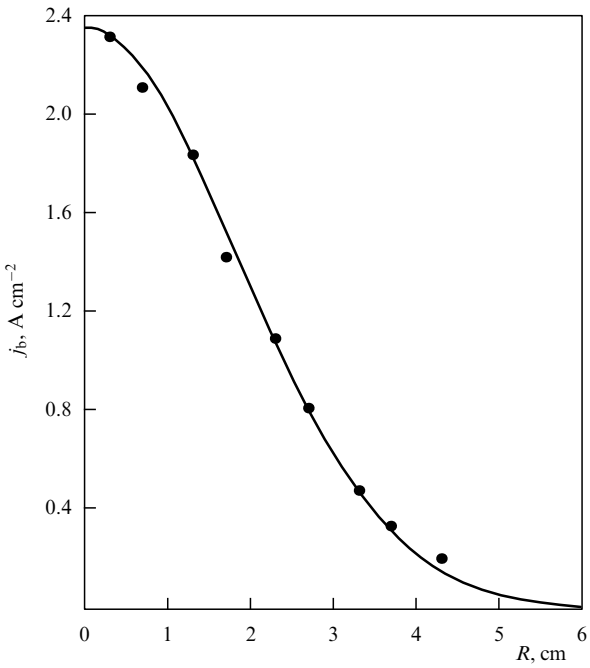

Figure 10. Atomic flux density profile measured at the beam focus 120 cm from the source.

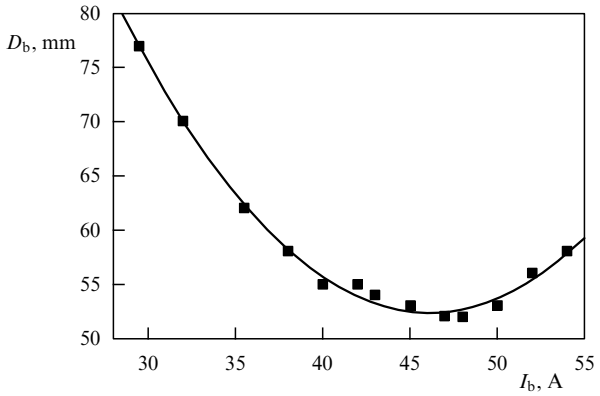

Figure 11. Beam current dependence of beam diameter at the 1/e level.

the beam focus 120 cm from the source. The character of the profile suggests that the beam radius at the 1/e level is 2.5 cm, in agreement with the integral angular divergence of 2×10^{-2} rad. The flux density of fast atoms at the focus is 2.4 A cm^{-2}. Figure 11 illustrates the measured dependence of beam diameter on its current. Evidently, the beam has a minimal width when its current ranges 45–50 A.

The beam composition was measured by a magnetic analyzer; the proton fraction in the ion beam formed amounted to 90%, and H_2^+ and H_3^+ ion fractions accounted for 7% and 3%, respectively. The measured beam neutralization efficiency was 73%, i.e., close to the equilibrium yield of atoms at an energy of 25 keV (76%). The power of the resultant fast atom beam reached 0.9 MW.

Early versions of BINP ion sources were designed to produce beams of relatively short duration (0.01–0.1 s) to meet the parameters of plasma traps [9, 59]. Power and duration restrictions largely arose from a sharp reduction in the plasma source lifetime (mainly due to cathode erosion) and overheating of IOS grids in long pulses. In the 1980s–1990s, a typical requirement in CF research became the multisecond working regime and the power of a single injector module above 1 MW. The development of up-to-date injectors of neutral beams at BINP required correcting almost all elements of the devices. The first structures to be modified were plasma generators and beam-forming electrodes.

3.1 Radio-frequency plasma generator

Taking advantage of RF plasma generators practically eliminates the problem of erosion of structural elements of a plasma source, which makes possible, in principle, work with the use of long pulses, including a stationary regime. BINP researchers developed a series of RF plasma sources for diagnostic and heating injectors differing in current density of the ion emitter and total ion current.

The design of all RF plasma sources is virtually identical [77]. An antenna consisting of several windings maintains a discharge at a frequency close to 4 MHz in the cylindrical ceramic chamber under a pressure of $\sim$ 10 mTorr. Permanent magnets placed at the rear wall of the plasma chamber not only play the role of a magnetic wall insulating the plasma and decreasing its losses, but also enhance the efficiency of its generation, provided an optimal configuration is specially chosen. Metallization of the chamber dielectric wall in early versions of the sources resulted in a change in plasma composition (increased fraction of molecular ions). The

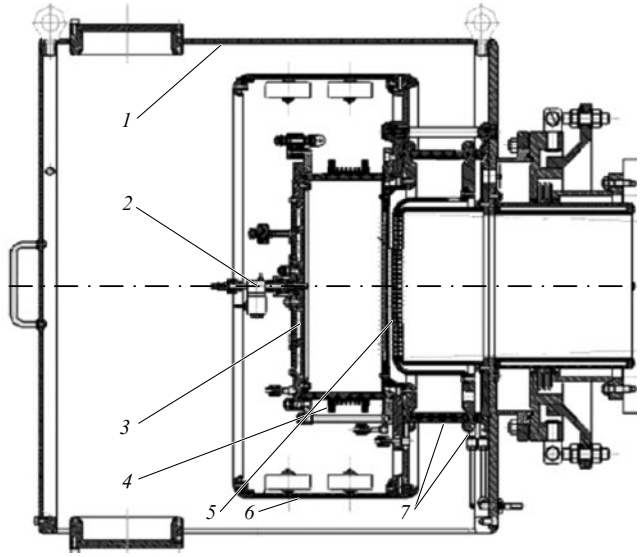

Figure 12. Radio-frequency ion source: *1* is the protective housing, *2* — gas valve, *3* — permanent magnets, *4* — RF antenna, *5* — IOS, *6* — screen, and *7* — IOS insulators.

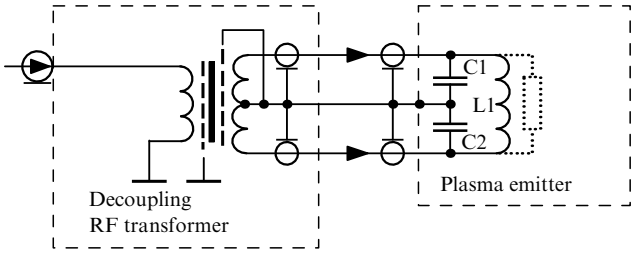

Figure 13. Schematic representation of voltage application to an RF antenna.

results of long-term operation of the injector [78] suggest a decrease from 70% to 40% in the amount of the beam's main component with time.

A Faraday screen was introduced in study [79] to protect the inner surface of the discharge chamber from sputtering and to reduce thermal load on the chamber wall. This resolved the problem of metallization by moderately affecting the molecular composition, but ensuring the long-term stability of the plasma parameters. However, the development of a plasma emitter for an extracted current above 50 A requires a high-power RF generator, which considerably complicates the power supply circuit and increases its cost. The method for doubling plasma emitter density proposed in Refs [79, 80] includes optimization of the magnetic wall geometry at the rear end of the cylindrical plasma chamber. An example of the RF-discharge plasma source proposed in Ref. [80] is presented in Fig. 12.

RF-discharge plasma sources with a Faraday screen and improved magnetic wall were employed in megawatt injectors operated in a second-to-second range [80–82]. The authors of Ref. [82] practised on an RF generator with a semiconductor-based power supply circuit, which significantly simplified the construction. In other cases, the RF generator included a 100-kW tube tetrode.

In all these devices, a symmetric two-feeder power supply system was employed to feed the gas discharge-maintaining antenna (Fig. 13). Powerful RF supply was transmitted

through co-axial cables. An insulating high-voltage transformer was connected to the RF emitter antenna using two co-axial cables, the central cores of which were attached to antenna terminals. Cable braids were linked up with the transformer midpoint and the RF screen of the plasma emitter, which was connected to the common point of capacitors C1 and C2. The capacitors and antenna inductance L1 were tuned to resonance. Out-of-phase currents of the feeders were precisely symmetrized by adjusting the capacitors parallel to the antenna. Such a system allowed obtaining full voltage on the antenna and half of it at each of its terminals with respect to constructional elements. Simultaneously, the level of antenna-driven noise and its influence on the equipment of the CF facility was substantially reduced. In radio engineering, this well-known symmetric scheme is used to feed dipole antennas; its application in the above modification of RF plasma sources proved very successful.

3.2 Development of plasma generators making use of arc discharge with a long-pulse cold cathode

Figure 14 demonstrates the layout of an arc plasma generator operating with a pulse length of up to 2 s [83]. To enhance operating time of the device from a few dozen milliseconds, the volume of the cathode cavity is markedly increased by substituting the hemispherical cavity with a radius of 10 mm with a 22-mm deep cylindrical one 22 mm in diameter. The molybdenum cathode electrode *1* is pressed against a copper flange having a cooling passage.

Intense sputtering of the cathode metal over the insulator installed between the cathode and the floating diaphragm in cold-cathode arc generators represents a serious problem, because this causes a short circuit between them leading to operational disturbances. In the construction under consideration, the insulator has a larger radius, while the protrusion is made at the near-axial diaphragm hole deep into the cathode cavity, which prevents the movement of cathode spots and discharge currents to the cathode edge. The surface of the cathode electrode carries a circular insulator *2* in-built around its edge to prevent as well the penetration of discharge currents into the peripheral region of the gap between the cathode and the diaphragm. All diaphragms of the discharge channel, the cathode, and the anode are water-cooled. Such design prolongs the operational life of the arc plasma generator in the injector up to almost one year in a typical regime of tokamak experiments. The generator is an easily detachable component; it is either replaced or cleaned at the end of its service life. To further increase the running time of the arc plasma generator, a heated composite cathode from lanthanum boride disks interspersed with anisotropic graphite was subsequently used [84]. When the cathode was heated by a passing current, heat was released largely in graphite interlayers. The operational life of the plasma source at a discharge current of ≈ 400 A was eventually increased to 10 s.

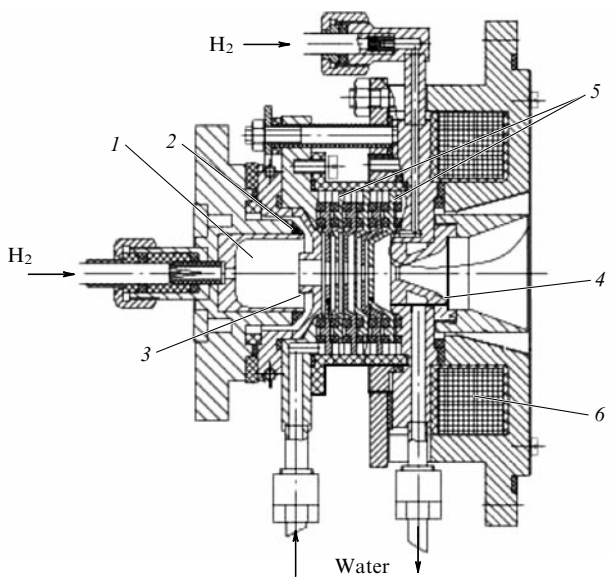

Figure 14. Arc plasma generator: *1* is the copper cathode, *2* — Mo insert, *3* — cathode washer, *4* — anode, *5* — discharge channel washers, and *6* — magnet insulation winding.

3.3 Summation of plasma jets to create the emitter with a high extracted current

The joint work of several arc generators resulted in an increase in both plasma density at the emitter and its area which is of importance for powerful ion sources with the extracted IOS current in excess of 50 A. This method was employed in an earlier study [85]. Reference [86] deals with a plasma source in which plasma jets from four arc generators were combined to produce an ion beam current of up to 180 A. A combination of two plasma jets was successfully realized in Ref. [87]. However, experiments on combining jets in the expansion chamber with a discharge as long as $\geqslant 10$ ms revealed the mutual interference of gas flows from the generators, which decreased plasma density in the emitter region (the first IOS grid). The mutual influence of plasma jets was less pronounced in the case of extremely low working gas feeding into a discharge when its regime became unstable and accompanied by noises in the discharge and beam currents. The situation was significantly improved with a passage to the space discharge regime described in Ref. [87], in which the chamber casing with a magnetic wall functioned as the second anode common for all generators, with part of the arc discharge current branching off to it. In the ion sources described in Ref. [86], where summation of four plasma jets was needed, practically all discharge current was directed to the second anode. The space discharge regime made possible not only jet composition without a loss of plasma, but also an appreciable improvement in the effectiveness of plasma production by each generator. Due to this, the ion current from the source amounts to the desired value at a much smaller arc discharge current. By way of example, a discharge current up to 1100 A was needed at similar parameters to extract a 40-A beam current [87], whereas a discharge current of 650 A proved sufficient to extract a 180-A current beam in the space discharge regime with a composition of four jets [86].

3.4 Ion-optical system

The geometry of an IOS unit cell (slit cell) was chosen by modeling based on the PBGUNS (Particle Beam GUN Simulation) code [89]. An example of an optimized electrode geometry is presented in Fig. 15 for an injector with the beam energy and power varying during a pulse at an energy of 30 keV [89]. In this case, the IOS unit cell is shaped like a 21×3-mm slit cell. Figure 15a shows the trajectories of ions and the electric field equipotential across the slit. The calculated diagram of transverse emittance is presented in Fig. 15b, and the theoretical dependence of beam angular

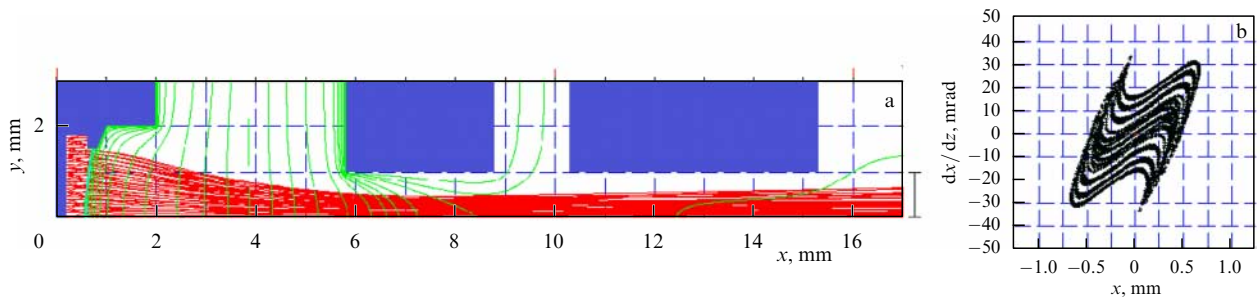

Figure 15. (a) Ion trajectories in an IOS and equipotential pattern and (b) emittance diagram.

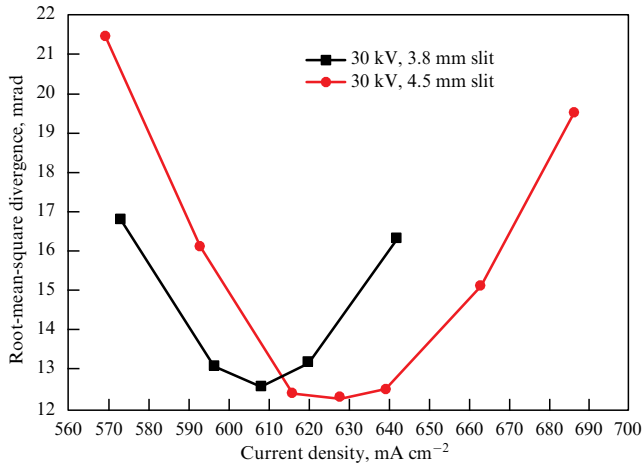

Figure 16. Beam angular divergence across the slits at different beam energies.

divergence across the slit on extractable current density in Fig. 16.

The results thus obtained were verified by calculations with the use of the KOBRA3-INP three-dimensional code for the solution of ion and electron optics problems [90] at a beam energy of 35 keV; the results are presented in Figs 17–19. Calculations of a 3-mm slit cell with the use of the KOBRA3-INP code gave an angular divergence of 13 mrad across the slits, and 12 mrad along them. The following plasma parameters in the ion emitter were adopted: plasma potential of 20 V, ion temperature of 0.7 eV, and electron temperature of 5 eV. Plasma composition was as follows: protons 70%, H_2^+ 20%, and H_3^+ 10%.

Extracted current densities in both calculations were practically identical: around 600 mA cm^{-2} for a hydrogen beam with the mass composition typical of RF plasma sources. In experiments with an ion source, the measured angular divergence across the slits proved to be roughly twice as much as the theoretical one, probably due to imperfections in electrode manufacturing and uncertainties in calculations

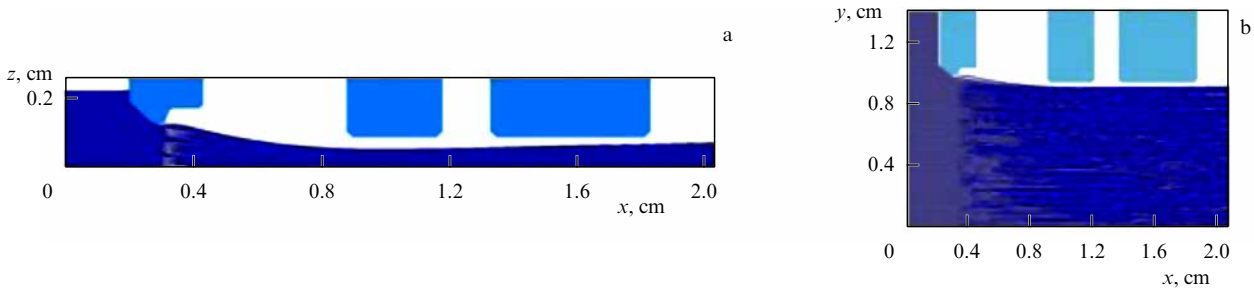

Figure 17. Ion trajectories in the IOS unit cell (in section): across (a) and along (b) the slit. Beam energy is 35 keV.

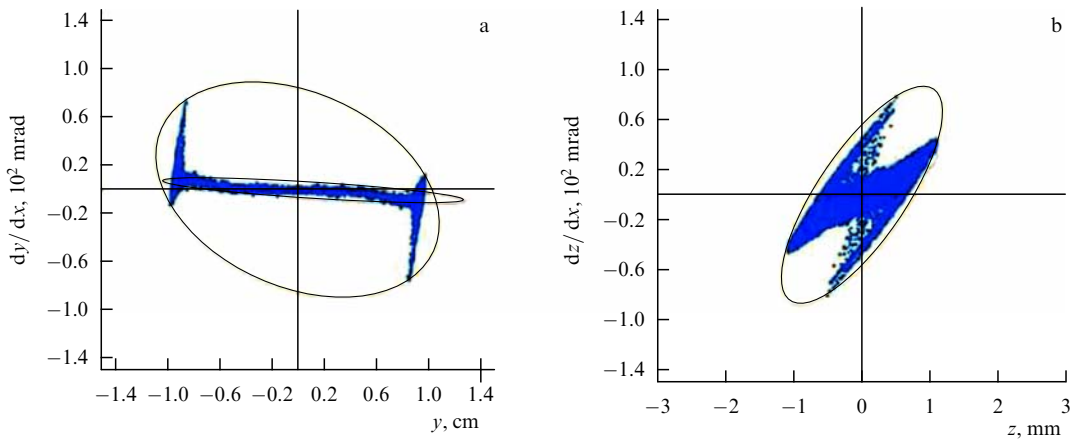

Figure 18. Emittance diagram along (a) and across (b) the slit.

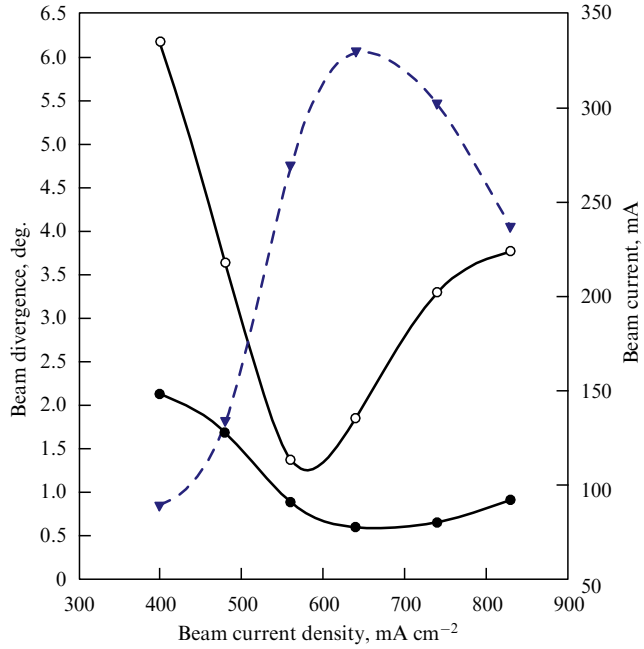

Figure 19. Divergence along (dark dots) and across (light dots) the slit as a function of current density. Ion current density as a function of total current in the cell (triangles).

of the compensation boundary for the space charge near the grounded electrode at the exit from the IOS. Current density calculated with the use of the PBGUNS code also usually differs from the experimentally measured one. This discrepancy is attributable to several factors. For example, the presence of molecular components in the beam and irregularities in the plasma flow are each responsible for roughly a 5% decrease in current density in comparison with the theoretical one, while the loss of particles at the edges of the emission hole accounts for a 30% reduction in current density.

A schematic of the ion source developed is presented in Fig. 20 (in section). The 47-mm long slits in the IOS electrodes are disposed in a circle 250 mm in diameter with the transverse pitch between them being 6 mm. The electrodes are manufactured of heat-resistant chrome-zirconium bronze of BrKhTsr grade (in *Russ. abbr.*). The finished piece is welded to the holder with M0b oxygen-free copper.

Ion injector operation is accompanied by the liberation of large amounts of heat at the IOS electrodes.

Heat is released due to particle scattering by a neutral gas, its ionization in the accelerating gap, and the partial charge exchange of beam particles in the IOS gaps. The characteristic liberated power accounts for roughly 1% of the total ion beam power per electrode [91]. It causes electrode heating and subsequent thermal deformation. Since the electrodes have a spherical shape to ensure beam focusing, thermal deformation results in a change to the accelerating gap, radius of electrode curvature, and mutual position of the slits, which can significantly worsen the quality of the extracted beam. This problem acquires special importance in the absence of an active electrode cooling system, as is the case in the situation being considered.

Manufacturing IOS electrodes with cooling channels is a challenging technological problem. There are several approaches to address it [92, 93], but the optimal solution remains to be found. Active cooling of electrodes is rarely

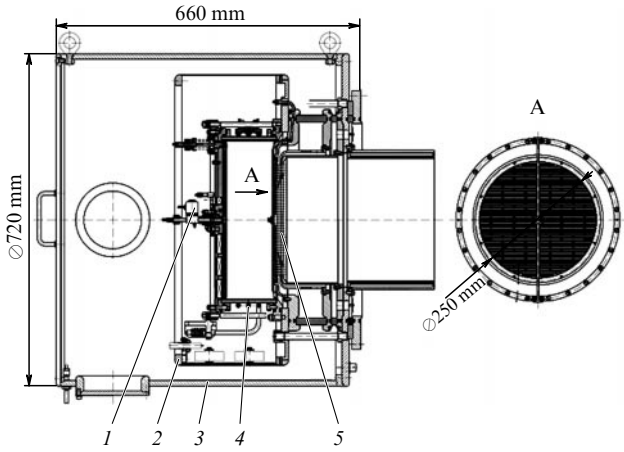

Figure 20. Schematic of an ion source [90]: *1* is the gas valve, *2*, *3* — magnetic screens, *4* — RF antenna, and *5* — IOS electrodes.

practized on ion sources developed at BINP, because it markedly impairs IOS transparency. In most sources, the so-called inertial cooling of electrodes is employed instead of active cooling. In such cases, electrode temperature is limited only by their thermal capacity, and cooling occurs between pulses owing to contact with the actively cooled electrode holder. Clearly, this method can be applied if pulse duration does not exceed a few seconds [94]. Its advantages include enhanced transparency of electrodes and simplification of the technological cycle during their manufacturing. In the case of inertial (passive) cooling, deformation of electrodes needs to be compensated for by a special system of slots cut in the holders, reducing to a minimum strains appeared along the electrode surface and the IOS axis. In the ion source shown in Fig. 20, the plasma electrode has a system of slots cut in the azimuthal direction, while both accelerating and grounded electrodes have a system of radial cuts.

It should be borne in mind that azimuthal cuts significantly deteriorate heat removal from the working part of the plasma electrode. To improve heat removal, the central part of the electrode is mechanically connected to the boss through which the water-cooled tube is inserted. The tube is attached to the ends of the electrode exterior to the cuts to reduce mechanical load on the working part. Radial cuts do not prevent from the removal of heat that occurs without hindrance in the pauses between pulses due to contact with the cooled flange. Grid heating, cooling, and deformation were calculated using the ANSYS Workbench software package [95]. The heat flow onto each grid amounted to 12 kW for 2 s. Results of calculations of the plasma grid behavior on being heated are presented in Fig. 21.

The above system of cuts enables effectively suppressing deformation along the beam axis to noncritical values (calculated values are as follows: plasma grid of 0.01 mm, accelerating and grounded grids of 0.18 mm). Such a duty cycle (2/300 s) is not associated with an appreciable temperature buildup. The temperature of the plasma grid increases by 25 °C, and that of the remaining grids by 7 °C. A similar IOS design is employed in various BINP injectors with a neutral beam duration up to 2 s and power up to 1 MW.

3.5 Special ion sources

3.5.1 Source of carbon negative ions for an accelerator magnetic mass spectrometer. Accelerator mass spectrometers

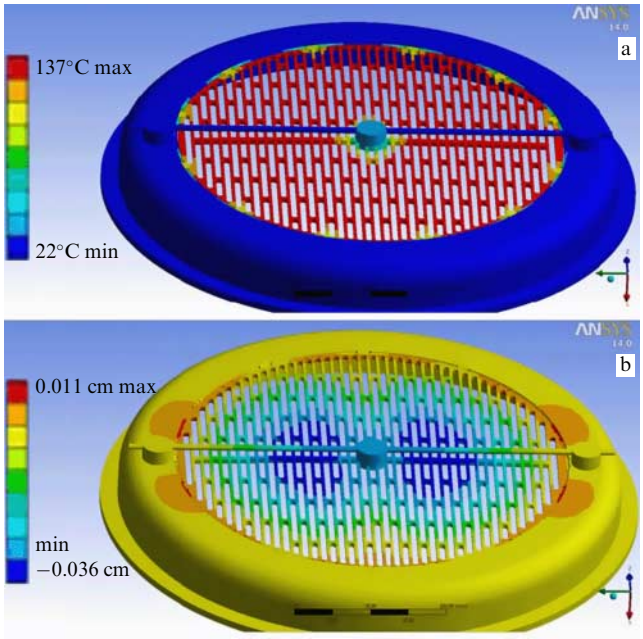

Figure 21. (Color online.) (a) Temperature field of the plasma grid after heating, and (b) plasma grid deformation along the beam axis.

(AMSs) currently available in most developed countries provide a powerful tool for basic and applied research. A high-resolution AMS created at BINP permits studying the very small amounts of substances of interest [96]. At present, this instrument is successfully used for the purpose of radiocarbon dating. The impossibility of separating isobars limits the resolving power of conventional mass spectroscopy, amounting to seven orders of magnitude. The use of AMSs allows this restriction to be overcome and distinguishing between ion fluxes differing by 15 orders of magnitude due to the possibility of counting even individual ions.

The AMS developed by BINP has a special sputter type carbon negative ion source where negative ions of the study substance are generated by a focused beam of positive cesium ions. Cesium is simultaneously adapted in two processes: to sputter the sample, and to create conditions for negative ion generation on its surface. The development of the sputter type source of negative ions required solving several problems arising from the necessity to maintain long-term functioning of AMS components under extreme conditions (high temperature, aggressive medium, strong electric fields). Specifically, an ionizer temperature of $\sim 1100\,^{\circ}$C is needed for thermal ionization of cesium atoms. A specially designed source with a revolving drum for charging 24 targets was created to facilitate continuous alternation of test and working specimens. A schematic of the source mounted into an AMS [97] is shown in Fig. 22, and its general view in Fig. 23.

The source has been successfully exploited for 10 years in the AMS of the Cenozoic Geochronology Multiple-Access Centre, Siberian Branch of the Russian Academy of Sciences (Novosibirsk).

3.5.2 ECR proton source. Over a number of years, BINP has been developing ion sources for various applications, including ion implantation into semiconductors and blistering investigations during bombardment of neutron-generating

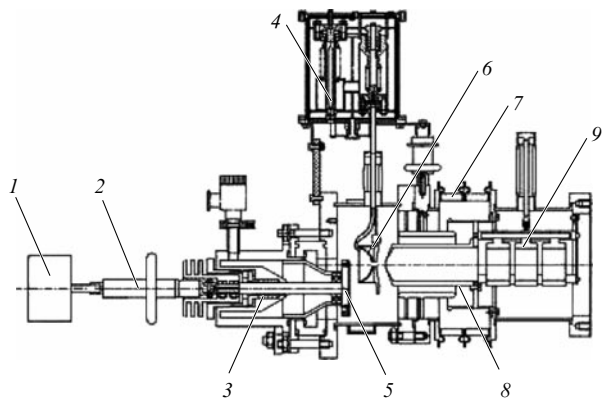

Figure 22. Schematic of the source installed on the AMS: *1* is the stepper, *2* — insulating shaft, *3* — Wilson seal, *4* — cesium furnace with a valve, *5* — drum with target samples, *6* — thermal ionizer, *7* — insulator, *8* — extracting electrode, and *9* — electrostatic lens.

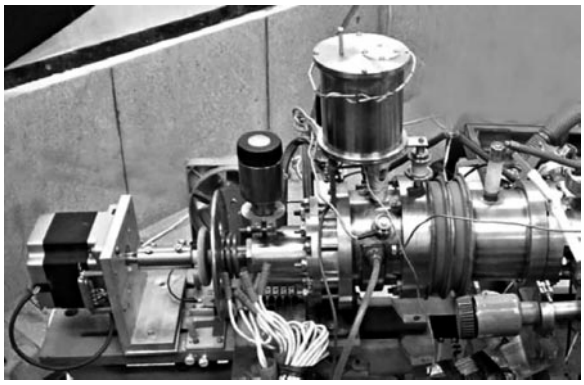

Figure 23. Exterior view of the AMS source.

lithium targets. A special ion source with electron cyclotron resonance (ECR) plasma generation shown in Fig. 24 was developed for these purposes [98]. At a microwave input power of 150 W, the source admits air cooling and produces an extractable ion current of up to 17 mA at an accelerating voltage of 45 kV. At a beam divergence of 0.4° and emittance of 0.13π mm mrad, the proton content is around 70%.

The BINP ECR proton source does not require high-potential power supply devices, while small power consumption in the discharge makes unnecessary the feeding of a cooling liquid with low electrical conduction.

3.5.3 Source of Xe^{+1} ions for the measurement of the potential profile in GDT. The spatial profile of the electric potential is one of the plasma characteristics of value for understanding plasma confinement physics in magnetic traps. At present, the potential distribution in GDT is measured with the aid of a set of Langmuir probes, and plasma potential on the axis by an energy analyzer of ions leaving the GDT magnetic system through its butt ends. However, probes cannot be used in a plasma with the electron temperature raised to 1 keV under the effect of additional ECR heating. Accurate measurements of plasma potential in the middle plane of GDT are performed with a special device using a beam of heavy ions. Its main components are the primary beam injector and the detector of deflected ions.

A three-dimensional model of the xenon ion beam injector [99] is shown in Fig. 25. Xenon undergoes ionization by an arc

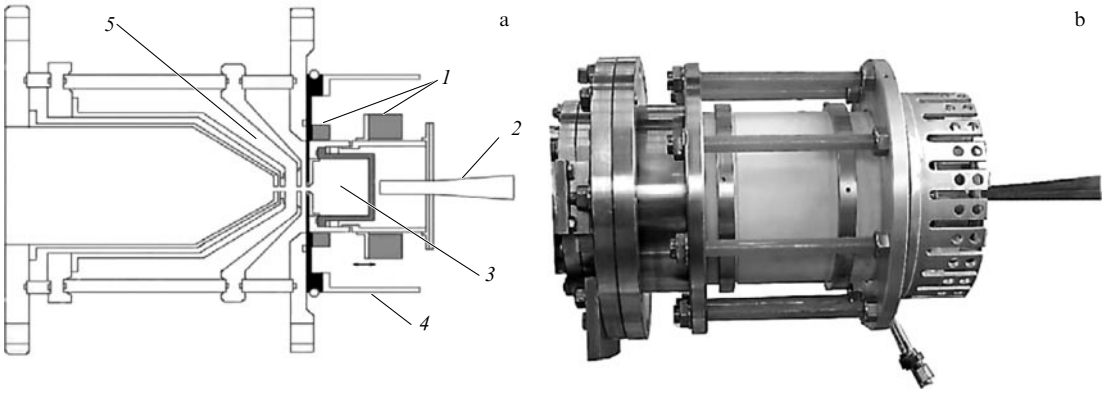

Figure 24. (a) Schematic of an ECR proton source: *1* is the magnetic system, *2* — waveguide, *3* — ceramic gas-discharge chamber, *4* — radiator, *5* — ion-optical system. (b) Exterior view of the ECR proton source.

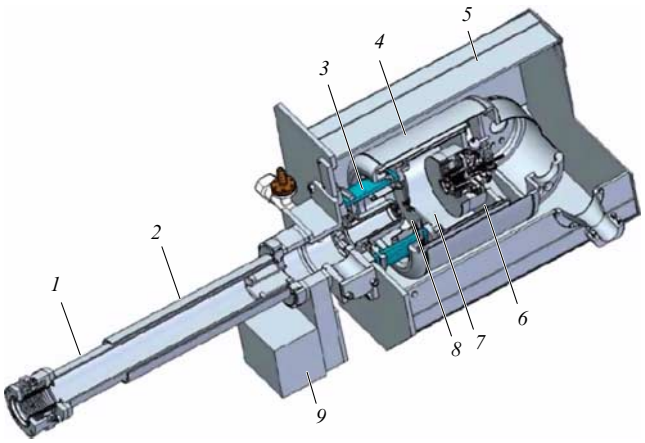

Figure 25. Xe^{+1} ion source for a potentiometer: *1* is the beam tract, *2* — magnetic screen of the beam tract, *3* — isolating unit of the ion source, *4* — electrostatic screen, *5* — magnetic screen, *6* — arc plasma generator, *7* — expansion volume, *8* — ion-optical system, and *9* — vacuum gate.

discharge in plasma generator *6*, freely expands in plasma chamber *7* of a source, and enters ion-optical system *8*, where it is accelerated to an energy of 75 keV. To reduce the influence of the magnetic field on ion formation and transport, the source and the beam tract are protected by screens *2* and *5* made of soft magnetic steel.

The IOS geometry is chosen so as to minimize the beam angular divergence. The size of the beam at the exit from the system is 2×20 mm; the angular divergence equals 4 mrad, and the Xe^{+1} ion current in the system reaches 7 mA.

3.6 Engineering systems of powerful atomic beam injectors

3.6.1 Vacuum pumping systems. High-performance vacuum pumping systems (up to 10^6 l s^{-1}) with titanium arc evaporators [86, 100], cryosorption pumps [75, 80, 82, 89], and bulk getter pumping systems were created to ensure work of powerful BINP injectors.

The operation of an atomic injector is inevitably associated with an accompanying gas flow. Part of it goes out directly from the ion source by virtue of its finite gas efficiency. A large portion of the gas is puffed into the ion beam neutralizer, while another one forms after the beam passes through the neutralizer and ions that escaped charge exchange experience dumping onto the ion collector when acted upon by the deflecting magnet. Furthermore, some amount of the gas is released by desorption from the walls of the beam tract under the effect of beam particles and radiation. The total accompanying gas flux into the chamber of BINP injectors may reach 30 l Torr s^{-1}.

Meanwhile, the conditions of a plasma experiment predetermine characteristics of gas flows from the injector to the host device. This, in turn, imposes specific requirements on the vacuum pumping systems used in injectors. Moreover, it should be borne in mind that atomic injectors are operated in the diffuse magnetic field of a plasma trap, and part of the atoms are lost in re-ionization on the accompanying gas. In addition, there is a risk of the so-called beam blocking effect manifested in the pipe connecting the injector with the plasma trap as avalanche growth of beam re-ionization losses on the gas desorbed by the beam from the pipe walls [101]. All these factors need to be allowed for when choosing the pumping system.

High-performance differential pumping is necessary to meet the conditions arising from the presence of a gas flow. The desired pumping rate usually varies from 10^4 to 10^6 l s^{-1}. Such a rate is ensured by the use of cryocondensation and getter sorption pumps, as well as bulk getter pumps.

3.6.2 Cryogenic pumps. Cryocondensation pumps are extensively exploited as a means of producing or maintaining high vacuum in large vacuum vessels. They find, in particular, application to BINP atomic injectors. Hydrogen pumping occurs as gas molecules adhere to a cryopanel surface having a temperature close to the liquid-helium temperature. To reduce heat flow from the environment, the panel is shielded by chevron baffles at the liquid-nitrogen temperature. The pumping rate is determined by the conductance of the chevron system; therefore, it is almost a third of the rate of that in systems with open cryopanels.

The cooling of the work surface in a cryogenic pump occurs usually due to thermal contact with a liquid-helium tank. In addition, a tank containing liquid nitrogen is needed to cool the chevron baffles. BINP engineers developed diagnostic injectors with filling cryopumps for TEXTOR (Technology Oriented Research) tokamaks ($2 \times 5 \times 10^4$ l s^{-1}), RFX tokamaks (Reversed-Field eXperiment), and Alcator C-Mod and TCV (Tokamak a Configuration Variable), as well as a cryopump for the 9-A H^- ion source at BINP ($2 \times 5 \times 10^5$ l s$^-$).

Recently, a closed helium cycle has been adapted to cryopumps for BINP beam injectors. Heat is removed by a

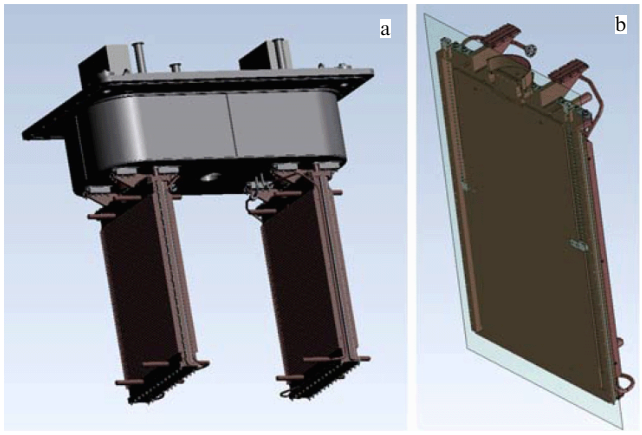

Figure 26. Cryogenic pump (a) of TCV injector [90], and (b) its cryopanel.

commercial cryohead in thermal contact with the pumping panel of the cryogenic pump. Removable thermal power is 1.5 W and the maximum achievable temperature is 3.5 K. Indisputable advantages of such pumps are their low operation costs due to the absence of liquid-helium consumption and lower pressure compared with that in priming cryopumps owing to the low temperature (some 10^{-11} Torr). Cryogenic pumps were installed in the injectors TAE-1 (Tri Alpha Energy 1) [80] (pumping rate $2\times7\times10^4$ l s^{-1}), COMPASS-D (COMPact ASSembly D-shaped vessel) ($2\times6\times10^4$ l s^{-1}) [87], TCV ($4\times6\times10^4$ l s^{-1}) [88]) (Fig. 26), and at the bench of the 120-keV H^- ion source ($2\times6\times10^4$ l s^{-1}) operated by BINP [102, 103].

Drawbacks inherent in pumps of this type ensue from constraints on the removed thermal power. Thus, under specific conditions, an excess heat flow arriving at the cryogenic surface may cause its heating and subsequent evaporation of frozen cryogenic sediment.

3.6.3 Sorption pumps with titanium sputtering. Pumping systems based on hydrogen sorption by a titanium-coated surface are rather frequently employed in BINP injectors of relatively short atomic beams (a few dozen milliseconds) [76, 100]. Let us consider the peculiar features of such systems as exemplified by the pumping system of the injector for the C-2U/W facility [100] with a hydrogen pumping rate of 10^5 l s^{-1} at a warm state, and 4×10^5 l s^{-1} at the liquid-nitrogen temperature.

A copper liner cooled by liquid nitrogen flowing in the channels that make up the liner's carcass is placed in a ⌀1300 × 1400-mm vacuum tank (Fig. 27). The inner ribs of the liner enlarge its area to 5 m^2. Four titanium arc sputterers are disposed along the liner axis. A schematic of the sputtering device is presented in Fig. 28 [100].

A vacuum arc with a 250–300-A current is ignited between the titanium rod and the walls of the liner. Cathode spots move over the rod surface with a speed of around 10 m s^{-1} and sputter the titanium at a rate of $\sim 10^{-2}$ g s^{-1}.

3.6.4 Bulk getter pumps. Bulk getters produced by pressing and baking active metal powders, such as Ti and Ti–V and Ti–Zr–Al alloys, have a well-developed surface due to a porous structure.

The powders can be either compacted into pellets or used for manufacturing more intricately shaped getters, e.g., as

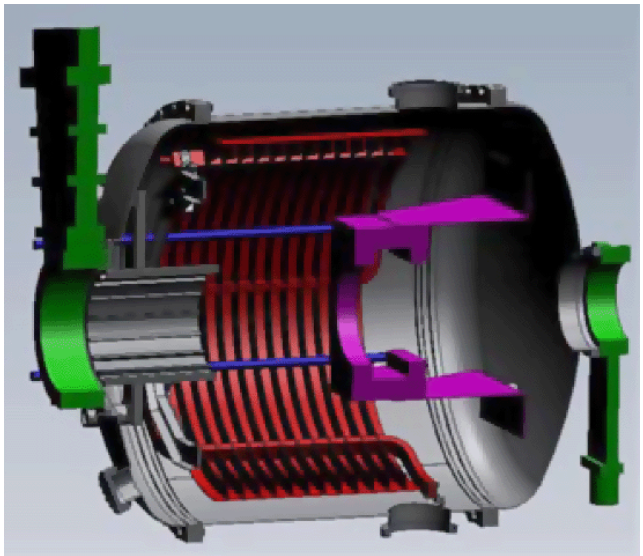

Figure 27. Getter pump.

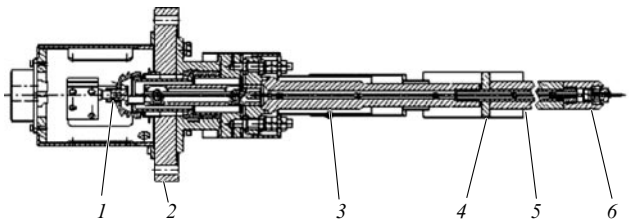

Figure 28. Titanium arc sputtering device: *1* is the lead-in, *2* — flange, *3* — screen, *4* — arc extinguisher, *5* — titanium rod, and *6* — arc ignitor.

porous briquettes on a nickel foil tap or sprayed over a substrate to form a porous layer of the desired thickness. A getter activated by heating to $\sim 400\,^\circ$C exhibits a very high sorption capacity.

It was proposed that a composite pump from nonsputterable getters with a pumping rate of 10^6 l s^{-1} be used to evacuate the accompanying flux from a negative ion source with a current of 9 A and energy of 120 keV [102]. Getter panels were tested in the presence of a negative ion beam with a 1-A current; the results confirmed the validity of engineering solutions behind the design of a composite pump.

3.6.5 Powerful atomic beam dump calorimeters. A beam dump is an indispensable component of both the diagnostic and heating injector beam tracts, needed because, in practice, most shots (training for IOS high-voltage strength, adjustment, testing) are fired in an autonomous mode rather than directly into the plasma of a facility. An atomic beam being neutral, the electrical measurement of its power encounters difficulty, and the beam absorber simultaneously functions as a calorimeter — power meter. The energy of particles entering the calorimeter depends on the molecular composition of the initial beam. Fragmentation of molecular ions following their neutralization in the gas target accounts for the presence of particles in the beam with the total energy corresponding to accelerating voltage and those with energies equivalent to 1/2 and 1/3 of the total energy (in the case of hydrogen or deuterium beams). The relation between these energy fractions is determined either by optical measurements of the

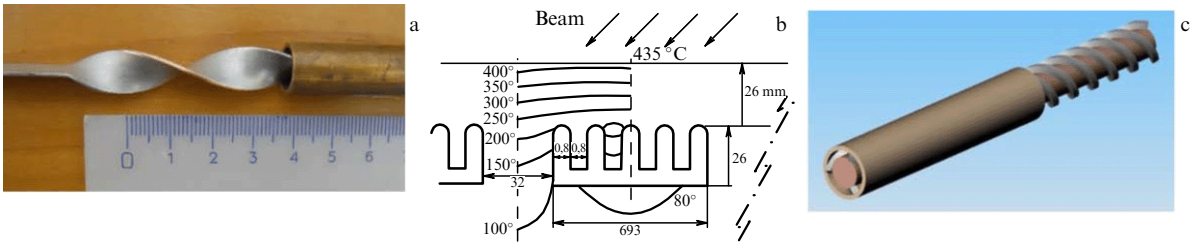

Figure 29. (a) Channel with a swirler. (b) Profiled channel. (c) Annular channel with a spiral swirler.

intensity of Doppler emission lines from beam particles after their neutralization [105] or by mass spectrometry of the initial ion beam, subsequently taking into consideration the energy dependence of the neutralization coefficient. The calorimeter is usually placed at the exit from the injector beam tract, and for implementing the beam inlet to the plasma of a facility, the calorimeter design provides for beam inlet/ejection from its axis.

The main difficulty facing developers of powerful beam dumps arises from the high power density, which may reach a few dozen kW cm^{-2}, and heat extraction crisis in water-cooled devices with a threshold of several kW cm^{-2}. The crisis is associated with a sharp decrease in heat transfer efficiency at the beam collector–cooling fluid interface, overheating, and metal decomposition. Therefore, a heat removal crisis should be ruled out, while the beam dump itself must be compact to avoid beam tract lengthening and operable under moderate working conditions for the cooling fluid supply system. For powerful injectors operating in the per-second regime, BINP developed beam dump calorimeters relatively easy to build and satisfying the above requirements.

Powerful beam dumps of injectors operating in the per-second regime cannot work under thermal inertia conditions: they need to be actively cooled. Their temperature rises to a maximum on the irradiated surface in proportion to beam power density. Therefore, the slope angle between the receiving surface and the beam axis should be decreased and cooling passages arranged as close to the surface exposed to radiation as possible to reduce maximum dump temperature. It is equally important that the beam absorber have the smallest possible size along the beam tract. These requirements are met by the V-shape of the beam receiver at which the surface slope is minimal near the vertex position on the beam axis, where the power density is especially high. However, it is impracticable to utilize a slope angle smaller than 5–7°, because thermal deformations at small angles cause a noticeable change to the slope, enhance local incident power, and contribute to further deformation. The reduction in the distance to the cooling channel is also limited in practice to 1–2 mm to avoid the formation of microcracks in repeated beam heating cycles and microleakage of water into the vacuum.

The known means for increasing the heat transfer coefficient at the wall–water interface and, accordingly, for raising the heat extraction crisis threshold include channels with a screw type flow swirlier (Fig. 29a) used in atomic beam calorimeters [106, 107] or a channel with a well-developed perimeter and small hydraulic diameter (Fig. 29b) used in the calorimeter [108]. The former method is technologically simple and advantageous in terms of the heat transfer coefficient and heat removal crisis threshold. Its disadvantage is the necessity to maintain a high flow rate in the channel (12 m s^{-1} at a pressure of 15 atm) [106]. This leads to overconsumption of water (for a given power output) at insignificant coolant heating and, accordingly, to elevated pressure in the main line. The channel for the second method [107] is difficult to form due to its small hydraulic size (0.8 mm) and the necessity of high pressure (12 atm) for coolant delivery, even if the channel is relatively short ($\sim$ 15 cm). During the practical exploitation of such channels in beam collectors and steam generators, the maximum power density did not exceed 3 kW cm^{-2}, whereas the maximum permissible power values in rotating flow systems amounted to 5–10 kW cm^{-2}.

Construction of a calorimeter for megawatt beams in the neutral beam injection system [80, 109] envisages the use of tubes with a co-axial annular slit and a spiral swirlier of water flow (Fig. 30).

The calorimeter has two shutters, each containing 11 copper tubes connected in parallel to common collectors for water delivery and discharge. The shutters can slide apart to let the beam in. Each tube has an annular channel formed by a rod 6 or 7 mm in diameter inserted into a channel with an inner diameter of 10 mm. The wire spiral (either single or double) inserted into a co-axial slit forms a 1.5- or 2-mm annular gap in the channel and simultaneously serves as the flow swirler. The spiral pitch is chosen, as in the case of the screw type (band) swirler [106], such that a turn of the flow through 180° occurs over a distance roughly equal to two channel diameters. Cooling tubes made by milling from standard copper bars of rectangular cross section have a ⌀10-mm trapeziform channel, unlike the round tubes used in Refs [102, 105]. Such a design allows the beam to be intercepted if the tubes are arranged in one row (rather than two as in Refs [102, 105]) and thereby halves the number of soldered and welded connections in the vacuum. To intercept the beam using a single tube row, the setup shown in Fig. 30a was applied in an earlier variant of the device in which even and odd tubes had different profiles. The setup presented in Fig. 30b was used in later versions of the calorimeter, in which all tubes were of the same type but slightly turned in the shutter plane normally to the beam axis. The gap for the beam between the neighboring tubes disappeared upon deviation

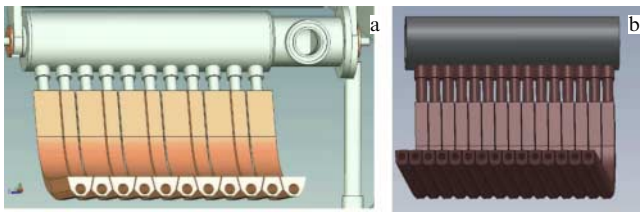

Figure 30. (a) Exterior view of a calorimeter. (b) Beam interception by a single tube row.

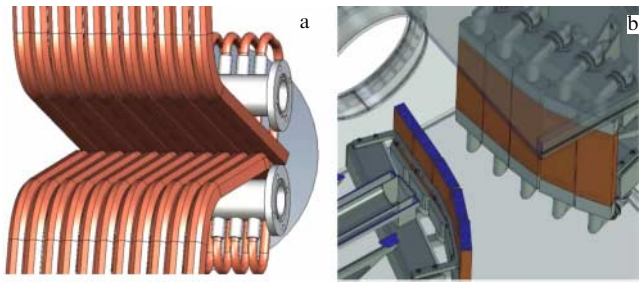

Figure 31. Calorimeter with longitudinally (a) and transversely (b) arranged tubes and ring channels in the plates (opened).

by $\sim 1^\circ$, permitting the beam to be stopped with a single row of tubes (even cylindrical ones).

A different design of the calorimeter was proposed for the injector of a 1-MW beam 2 s in duration [82, 89] (Fig. 31b). In this case, the shutters of the beam absorber are made from copper plates with cooling channels oriented across the beam axis. To let the beam enter the plasma facility, the shutters move apart normally to the beam. Each plate has three cooling channels with an annular gap analogous to that described in the preceding paragraph. The outer diameter of the channel is 16 mm, and the inner one 12 mm. The receiving surface is 75×200 mm^2 in area. The plate tilt angle with respect to the beam axis is varied to ensure a roughly identical load on the surface of all plates. With a typical Gaussian power distribution over the beam radius, the angle $\alpha(r)$ of plate inclination to the axis is given by the relation

$$\alpha(r) = \arcsin\left[K \exp\left(\frac{r^2}{r_0^2}\right)\right], \tag{3.1}$$

where constant $K = \sin\alpha_0$, α_0 is the minimal angle of inclination to the beam axis at the top of the shutters. The angle of inclination to the axis was given in a similar way in the construction with a longitudinal arrangement of the tubes. It permitted reducing to a minimum the longitudinal size of the absorber.

The annular channel with a spiral swirler is easy to fabricate and permits water consumption to be reduced by a factor of 1.5–2 at a similar flow rate, depending on the annular gap size. If it is small in size, the hydrodynamic characteristics of the flow (the Nusselt and Reynolds numbers) ensure a higher heat extraction coefficient than in the case of a cylindrical channel with a band swirler; this allows working at a lower flow rate and, accordingly, at a lower pressure that is known to grow quadratically with increasing rate. For example, the very first tests of the calorimeter described in Ref. [109] demonstrated its ability to work under insufficient pressure (3.5 atm) even at a flow rate as low as 2.5 m s^{-1} and water heating to boiling at the output. In contrast to the hydrodynamic channel, the size of which is smaller (only 0.8 mm in Ref. [108]), the annular gap has the advantage of a vortex type rotating flow, i.e., a higher gain in terms of heat transfer coefficient and heat removal crisis threshold.

In a word, the described shape of the water channel partly integrates the advantages of constructions [106, 107] and mitigates their disadvantages.

3.6.6 Power supply systems. The experience gained with the development of experimental physical devices at BINP and other leading research centers gives evidence that only specially designed systems guarantee an adequate power supply for various constituent components of these installations. Commercially produced articles with relevant characteristics are virtually nonexistent. Moreover, power supply systems for experimental physical facilities are not infrequently integrated into sophisticated engineering facilities using unconventional high-tech electrotechnical and electronic equipment. Therefore, the power supply systems should be designed with a view to making use of the components produced following uniform rules to ensure their compatibility with control systems, as well as electromagnetic compatibility with measuring and other equipment, taking into account that certain experimental physical devices may be sources of all kinds of noise and radiation. Specifically, the work of powerful plasma facilities, such as tokamaks, stellarators, and 'open' type plasma systems, is accompanied by the generation of strong scattered magnetic and electric fields with a very broad frequency range. Moreover, the pulsed and quasipulsed working pattern of these facilities is fought with substantial perturbations in power supply circuits. Design and development of specialized high-voltage power supply systems for experimental physical facilities should be considered an indispensable important area of work.

Neutral beam injectors are important sources of additional plasma heating in plasma facilities and a tool for the diagnostics of plasma characteristics. The main requirements for a source of high-voltage power supply for an atomic injector are formulated as follows. Ion sources of fast atom injectors are optimized for a specific operating voltage (the typical energy range for positive ions is 15–80 keV at a power from several hundred kilowatts to a few megawatts). Therefore, the nominal output voltage depends on the IOS configuration of a given ion source. However, conditions must be created to enable regulation of extracting voltage in a wide enough range. Relatively low voltage is needed for electrode training at the initial switching 'on' event and in the case of seal failure. As a rule, the pulsation level and long-term instability of output voltage should not exceed $\pm 1\%$ of the respective nominal values.

The design of the IOS for ion sources stipulates a maximally possible strength of electric fields which accounts for the so-called high-voltage 'training' regime, i.e., the period of operation with numerous breakdowns. A source of high-voltage power supply must be able to be turned on and off in the full voltage regime and move out of operation for less than 100–200 μs, with automatic recovery of the voltage after a breakdown for a time necessary for the IOS to restore the high-voltage strength (usually 1–2 ms). In the course of 'training', the voltage of a high-voltage source must be gradually raised from the minimal to the nominal level. The output voltage modulation pitch must be on the order of 1% of the nominal value. Neither a single breakdown nor a specified number of successive breakdowns should cause deformation or destruction of IOS electrodes. It is well known that the liberation of energy in the electrode system must not exceed 3–5 J. Both a sharp voltage drop and current gain following a high-voltage breakdown are accompanied by beam incidence on construction elements (mostly grids) and their local overheating.

Not infrequently, it is necessary to form both continuous and 100% amplitude-modulated output voltage to enhance the performance of a recording device and improve the signal-

to-noise ratio; in such cases, modulation frequency of output voltage can be chosen in a wide range of values. The modulation period of a high-voltage source is matched to that of the output power of an RF generator in the case of a high-frequency emitter and to the modulation period of the arc current in the case of an ion arc emitter. The characteristic voltage modulation frequency of high-voltage sources varies from 5 to 300 Hz. The voltage rise and fall time must not exceed 100–200 μs.

A high-voltage power supply source as a constituent component of sophisticated experimental physical facilities must allow remote computer-assisted control of states and status, as well as to the measurement of its output parameters with a desired accuracy and operation speed. There are several different options to choose the basic configuration of a high-voltage power supply source (modulator) for fast atom injectors.

High-voltage power supply sources using step-up transformers operating at the industrial network frequency of 50 (60) Hz are most widely applied. Such transformers may have either a large number of relatively low-voltage secondary windings (if based on the Pulse-Step Modulation scheme) or a single high-voltage rectifier of secondary voltage and a high-speed key intended to be operated with a full output voltage and current. The appearance of commercial high-speed high-voltage semiconductor keys makes it possible to design high-voltage regulators with an output voltage up to 100 kV and a power of several megawatts based on the pulse-width regulation schemes, with the high-voltage semiconductor key playing the role of a high-speed protection element in case of a high-voltage load breakdown. Such power supply sources can operate in both pulsed and continuous modes. Figure 32 presents a functional flow diagram of the power supply source of this type intended for a powerful atomic injector created at BINP [80].

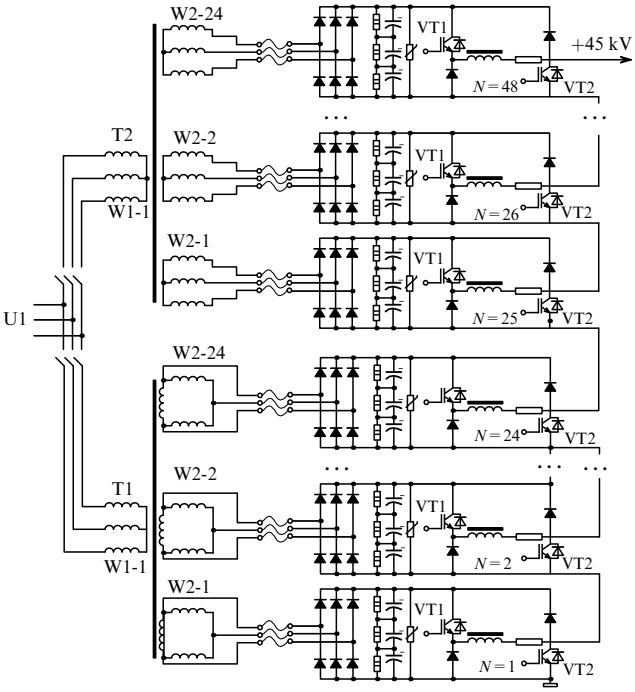

Figure 32. Functional flow diagram of the power supply source for a powerful quasistationary atomic injector: U1 is the input network, T1, T2 are the input transformers, W1-1 is the primary winding connection circuit, W2-*N* is the secondary *N*th winding connection circuit, VT1, VT2 are the slave keys, and $N = 1, 2.....48$ is the winding number.

This setup was utilized as a basis for almost ten high-voltage power supply sources of atomic injectors with a particle energy of 40 keV or higher, an equivalent atomic current higher than 25 A, and running time of 1–2 s.

In the 1970s, engineers at BINP developed the DINA-2 diagnostic injector with a single high-voltage rectifier of secondary voltage and a vacuum tube-based high-speed key [110, 111] designed for operation with full output voltage and current (DINA is the Russian abbreviation for Diagnostic Injector of Neutral Atoms). The diagnostic injector described in Ref. [111] had a beam modulation frequency up to 0.5 MHz. The vacuum tube modulator [112] was employed to create charge-exchange injection ion sources.

Also used are high-voltage power supply sources with pulsed boost transformers. Powerful high-voltage pulses up to a few milliseconds in duration can be produced if appropriate by a reliable and cheap method using a pulsed step-up transformer to whose primary winding the voltage of the preliminarily charged forming line is applied by a ion speed key (Fig. 33). The forming line voltage and transformation coefficient of the transformer determine the secondary winding voltage. Sometimes, additional high-voltage stabilizers based on series-connected varistors are put on.

The schematic presented in Fig. 33 was employed at BINP to develop and put into operation several high-voltage power supply sources for diagnostic neutral beam injectors [113–115] and Start type plasma heating injectors [116].

In the sources considered in Refs [110–116], the arc discharge was fed from the forming line with high-precision maintenance of current in the pulse peak (with an accuracy higher than ±5%).

Moreover, pulsed sources of controlled high voltage based on a distributed or sectioned capacitive energy storage device are adapted in several BINP injectors (Fig. 34), which contain a large number of relatively low-voltage capacitor batteries previously charged to the desired voltage. The batteries are connected in series with the use of semiconductor keys to produce high-voltage pulses of the necessary duration. The semiconductor keys can also be used as an element of a high-frequency pulse-width modulation (PWM) voltage regulator, which permits stabilized high-voltage pulses to be obtained. An important characteristic of the schemes with the use of capacitive storage devices is low power consumed from the industrial network and pulsed output power varying from a few hundred kilowatts to several megawatts.

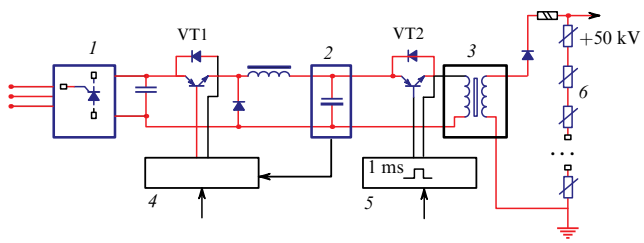

Figure 33. Functional flow diagram of a pulsed transformer-based high-voltage source: *1* is the network rectifier, *2* is the discharging capacitor or forming line, *3* is the pulsed step-up transformer, *4* is the VT1 key-based charge transformer control system, *5* is the VT2 key-based discharge transformer control system, and *6* is the varistor assembly for stabilizing output voltage. VT1 key-based device for charging the forming line.

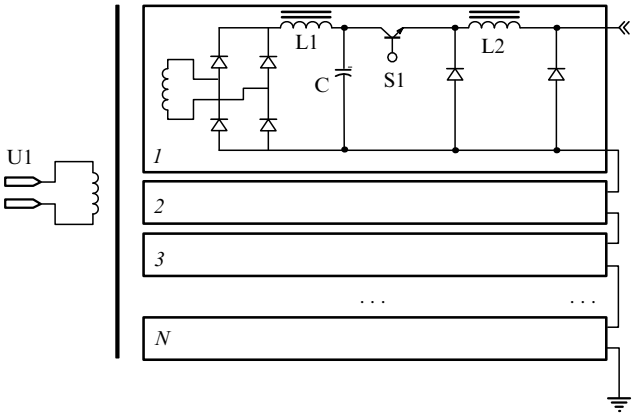

Figure 34. High-voltage source based on the sectioned capacitive energy storage device: U1 — high-frequency charging voltage (usually 20 kHz), L1 — charging current-limiting choke, C — capacitive storage, S1 — semiconductor key, and L2 — protective choke. 1, 2, ..., *N* — identical rectifier sections.

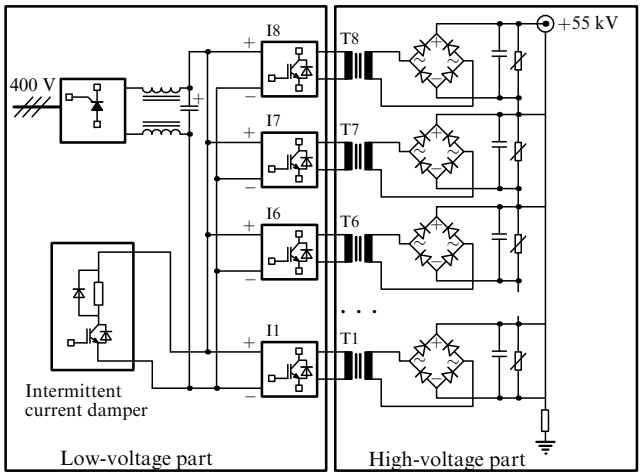

Figure 35. Functional flow diagram of high-voltage power supply source with the use of I1–I8 high-frequency inverters. T1–T8 — step-up transformers.

The use of the S1 key (see Fig. 34) as an element of the PWM regulator operating with a high voltage-conversion frequency allows reaching a stability of the output voltage of better than 1%. Power supply circuits of powerful atomic injectors operating with pulse durations of a few dozen milliseconds were put to practice in several laboratories investigating high-temperature plasma.

In addition to the above setups, certain injectors were armed with pulsed and stationary high-voltage power supply sources based on high-frequency semiconductor voltage converters (inverters) and isolation step-up transformers with series-connected diode rectification circuits (Fig. 35). Such module constructions make it possible to create high-power (up to a few megawatts) supply sources with a wide-range control of output voltage and high-quality output parameters. The power of a single semiconductor converter and a boost transformer operating at a frequency of up to 20 kHz is usually below 50 kW, which makes such a design highly attractive owing to its flexibility and ease of assembly and maintenance.

Insulated-gate bipolar transistor (IGBT) inverters I1–I8 (see Fig. 35) operating with a timing phase shift relative to each other are designed to generate PWM-controlled high-frequency voltage (16 kHz in the case being considered). This voltage is applied to the primary windings of step-up transformers T1–T8 of the high-voltage rectifier. The number of series-connected rectifiers (hence, the number of inverters) in such circuits is chosen to be from 6 to 12, depending on the required output power of the high-voltage source. The schematic presented in Fig. 35 includes eight rectifying cells and inverters. Constant voltage applied to the input of each of the eight parallel-connected transistor inverters is regulated in the range from 0 to 550 V using a network-enabled thyristor rectifier with a partially damped *LC* filter. Such two-step regulation (using a phase-controlled thyristor rectifier and PWM by transistor converters) ensures vast rearrangement of high output voltage (from 10 to 60 kV) and its reliable stabilization. The functional setup of the high-voltage power supply source presented in Fig. 35 was used to develop and put into practice up to ten atomic injectors for plasma heating and diagnostics in different BINP laboratories and several universities [117–119].

4. Beam injectors for plasma diagnostics

Detailed investigations into the plasma behavior in magnetic traps are carried out using various diagnostic techniques. Much attention is given to methods of active corpuscular diagnostics based on the application of special fast atom beams. These methods are employed to determine plasma characteristics from results of the study of its interaction with diagnostic beam atoms. They provide reliable information about local plasma parameters. Methods of active corpuscular diagnostics have been extensively developed in recent decades.

Parameters of fast atom beams are determined by the type of diagnostics and plasma characteristics. As a rule, beam intensity must be high enough to obtain an acceptable signal-to-noise ratio, which is of special importance in studies requiring high temporal resolution. The beam size must be small enough to ensure good spatial resolution. The choice of both beam composition and particle energy depends on the objectives of the diagnostics. For example, of special interest for beam emission spectroscopy of impurities are hydrogen atom beams with an energy of 50–60 keV, close to the maximum charge-exchange cross section energy for the excitation of the 8–7 optical transition in C^{5+} ions. This energy is also sufficient for penetration of the fast atom beam into the plasma in on-going experiments with a plasma volume radius of 0.5–1 m and mean density on the order of 10^{20} m^{-3}. It was shown that the injection of a diagnostic atomic beam with an equivalent current of ~ 1 A into the plasma guarantees reasonably high signals from detectors of the spectroscopic system [120, 121]. Nevertheless, moderately powerful beams should be involved to avoid local plasma heating. As a rule, this requirement is consistent with the necessity of obtaining a high enough signal from the detector system, provided that the atomic beam flux is limited to a few equivalent amperes.

Diagnostic fast atom beams with an energy up to 100 keV are formed by the charge-exchange method. In the ion source of a diagnostic injector, the multiaperture IOS forms an ion beam with a current of several amperes from the plasma emitter surface. Then, the ions of the beam thus produced are turned into atoms by charge exchange in the gas target. This

technique is also used to heat plasma in powerful fast atom beam injectors. However, generating a narrower beam in diagnostic injectors implies its focusing with minimal angular divergence. Furthermore, modulation of the diagnostic beam and a highly stable atomic energy are needed in many experiments. These requirements account for the specific characteristics of diagnostic injectors.

The development of DINA-series detectors for plasma physics experiments was initiated at BINP more than 30 years ago. The first injectors of this series had a pulse duration of 0.1–0.2 ms and a beam energy of 10–25 keV [111, 113, 115, 122], consistent with characteristic parameters of the plasma achieved in then-available toroidal systems and open traps. In ion sources of those injectors, plasma emitters were formed by an expanding plasma jet from the arc source. Ion cooling in collisionless jet expansion caused a drop in ion temperature to ~ 0.2 eV [123]. Ion beams were formed in finely structured multislit three- or four-electrode IOSs. The low ion temperature of plasma emitters accounted for the small angular divergence along the slits (~ 5 mrad). In some injectors, part of the beam that escaped charge exchange on the gas leaving the source was focused by a magnetic lens to be further neutralized in the pulsed charge-exchange target. In the DINA-3 injector with a beam magnetic focusing for the T-10 tokamak [115], the atomic flux density 1.5 m from the injector was 250 equivalent milliamperes (mA equivalent) per cm^2. The same injector was used with tokamak-10 to measure local ion temperature from Doppler broadening of charge exchange atom lines [124] and the Rutherford scattering of fast atoms [125].

DINA injectors continued to be designed and developed during the 1990s, when special attention was given to the lengthening of beam current pulses. Because magnetic focusing of the formed proton beam proved inefficient upon a rise in pulse duration due to charge exchange on the gas outgoing from the ion source, ballistic beam focusing was employed in new injectors of the DINA series with the use of a multiaperture ion-optical system having spherically curved electrodes (see Fig. 36). The use of a focusing multiaperture IOS allowed increasing the length of the beam current pulse by almost an order of magnitude. The pulse duration in the DINA-5F injector [126] was 3 ms at an atom energy up to 30 keV and an atomic flux up to 3 A equiv. DINA-6 and -7 injectors [127] formed atomic beams consisting of a sequence of up to twenty 1-ms pulses.

The DINA-5F injector (Fig. 37) includes an ion source and a charge-exchange tube (neutralizer). The ion source forms a focused beam of ions to be further converted into atoms in the pulsed gas target of the charge-exchange tube. The plasma emitter in the source is created by an arc plasma generator installed 10 cm from IOS.

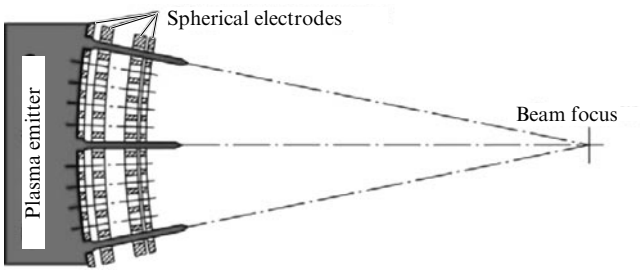

Figure 36. Schematic of ballistic beam focusing.

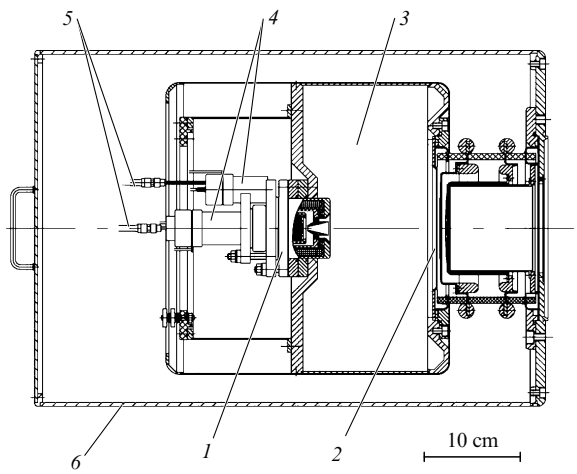

Figure 37. Ion source of DINA-5F diagnostic injector: *1* is the arc plasma generator, *2* — IOS, *3* — expander volume, *4* — pulsed gas valves, *5* — gas tubes, and *6* — casing.

The multiaperture four-electrode system with spherical electrodes focuses the beam at a distance of 130 cm. Each electrode of the ion-optical system has 547 holes 2.5 mm in diameter that form a hexagonal structure with a 3.2-mm pitch and an outer diameter of 8 cm. The electrodes are made of 0.5-mm thick molybdenum. The holes in the electrodes are photoetched. The spherical electrodes are shaped by hot stamping in a vacuum at the Mo recrystallization temperature. The bell-shaped radial distribution of proton current density in the plasma jet outflowing from the source is approximated by the expression [60]

$$j(r,z) = \frac{I}{\pi^2 z^2 (1 + r^2/z^2)^2} ,$$

where I is the total proton current in the jet. This means that the optimal formation of a proton beam requires, as prescribed by the 2/3 law, that IOS gaps be enlarged by increasing the radius in accordance with the expression $d(r) = d_0(1 + r^2/z^2)$, where d_0 is the gap size on the axis. An IOS with decreasing radii of curvature of the plasma, extracting, and accelerating electrodes should be adapted for the optimal formation of the proton beam with increased use of a plasma jet. The radii of curvature of the plasma, extracting, and accelerating electrodes are 400, 120, and 50 cm, respectively, for a hydrogen injector, and 160, 120, and 60 cm for a helium injector.

The ion source of the hydrogen DINA-5F injector forms an ion beam with an energy of 30 keV and 4 A equiv. current, while the helium injector produces a beam with an energy of 20 keV and 4.5 A equiv. current. The measured angular divergence of both beams is 1.6×10^{-2} rad, atomic flux density at the focus at a distance of 130 cm is 210 and 300 mA equiv. cm^{-2} for hydrogen and helium beams, respectively. The hydrogen beam composition was determined with the use of a magnetic analyzer and a stripping helium target placed in front of it. The measured number of total-energy hydrogen atoms is above 90% due to rather high plasma density, accounting for the high dissociation rate of molecular ions in the anode hole region of the arc plasma generator.

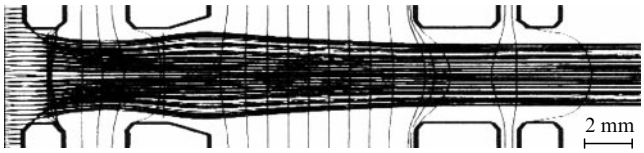

Figure 38. Ion trajectories in an optimized IOS.

In the MST reversed-field pinch experiment (Madison, USA), a DINA-5F hydrogen injector was employed to rapidly measure ion temperature from Doppler broadening of impurity lines and the magnetic field strength from the dynamic Stark effect [128]. A helium injector was applied to measure the ion temperature by the Rutherford scattering method. The time resolution of both diagnostic procedures was 10 μs.

In 1992–1997, the RUDI diagnostic injector [129] was developed to form hydrogen atom beams with an energy of 50 keV, 1 A equiv. current, and pulse duration of up to 10 s for a beam spectroscopy of impurities with the TEXTOR tokamak (Julich, Germany). A substantial increase in the beam lifetime in comparison with that in the DINA injectors was achieved by exploiting the plasma emitter in the RUDI ion source based on a high-frequency induction discharge and mutiaperture IOS with 'thick' electrodes allowing due to a high heat capacity the temperature elevation to be limited during a pulse. The geometry of thickened extracting and accelerating electrodes of the IOS was optimized using results of numerical simulation of elementary beam formation in a cell [130]. Figure 38 demonstrates the electrode geometry and ion tracks in the optimized ion-optical system. Emission current density in this case was 100 mA cm^{-2} with a beam formed angular divergence of 9 mrad.

A schematic of the RUDI injector is presented in Fig. 39. Its left part shows the ion source and the vacuum chamber of the injector with auxiliary systems, while the right part depicts the plasma cross section in the TEXTOR-94 tokamak. The focus of the diagnostic beam being offset by 4 m from the ion source is close to the plasma center. The vacuum chamber of the injector contains water-cooled elements, viz. a neutralizer, magnetic separator of ions, deflected ion dump, and movable calorimeter. The turbomolecular and cryogenic pumps are attached to the vacuum chamber of the injector. The neutralizer channel is partially filled with the gas outflowing from the gas-discharge chamber of the ion source; additional filling is effected through a pulsed gas valve. The magnetic separator of ions and the collector of ions that escaped charge exchange are installed on a special platform inside the vacuum tank. Each cryogenic pump at the top of the injector volume operates at a hydrogen pumping rate of 24×10^3 l s^{-1} in the molecular regime.

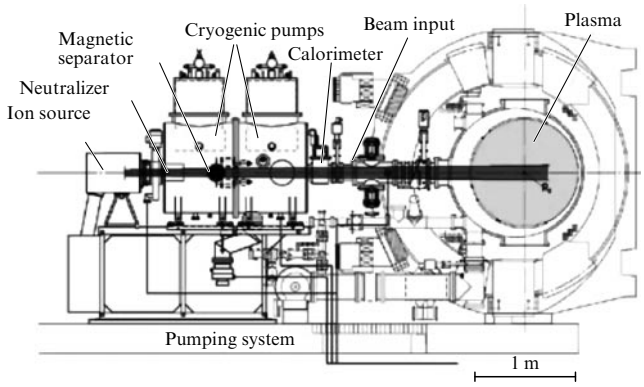

Figure 39. Schematic of RUDI diagnostic injector.

This injector installed on the TEXTOR tokamak was utilized to measure radial profiles of ion temperature and the concentrations of impurity ions by beam spectroscopy. After modernization of the injector, including replacement of the RF plasma emitter by an emitter with an arc generator producing 10-s pulses [131] and taking advantage of a multislit ion-optical system instead of an IOS with round apertures, atom flux density in plasma increased by a factor of 2, which allowed reliable measurement of the plasma poloidal rotation speed in the tokamak [132].

The RUDI injector was exploited as a basis for designing and putting into operation a diagnostic injector of a hydrogen atom beam for the TCV tokamak (Lausanne, Switzerland) with an energy of up to 52 keV, current up to 1.4 A equiv., and pulse duration of 2 s [133]. The RUDI-X diagnostic injector was intended for the large W-7X stellarator. Its beam had a hydrogen atom energy of 60 keV, equivalent current up to 2.4 A, and pulse duration up to 5 s. The diagnostic injector developed and tested for the tokamak T-15 [134] forms a hydrogen neutral beam with similar parameters.

Modern active corpuscular diagnostics face a number of ambitious challenging problems, including elucidation of fast ion distribution function in the plasma using artificial targets in the presence of a high background flux of charge-exchanged atoms and measurement of limiting magnetic fields in a high-pressure plasma based on the dynamic Stark effect.

The artificial target method is currently the most adequate technique for the measurement of the local distribution function for a fast ion population in the plasma. In this method, a diagnostic beam of fast atoms is injected into the plasma, and a beam of fast atoms formed as a result of charge exchange of fast ions on this beam is registered by an analyzer. However, the injection of powerful heating beams of hydrogen atoms and appreciable hydrogen inflow into the plasma are associated with a high background flux of charge-exchanged atoms. For reliable measurement of the fast ion distribution function under these conditions, the injected diagnostic beam must have a maximally high flux density and be capable of responding to rapid modulation to ensure reliable differentiation between the active signal from the charge-exchanged atoms and the varying passive signal of the background. A diagnostic injector of focused hydrogen atom beams with an energy of 40 keV, atomic flux of ~ 8.5 A equiv., and modulation at 10 kHz is currently under construction at BINP. Several fast modulation techniques described in Ref. [135] will be tested in experiments.

The combined method making use of the dynamic Stark effect and laser-induced fluorescence technique may prove crucial for the measurement of magnetic fields as strong as a few gauss. Superimposed atomic and laser beams are used for diagnostic purposes. A laser beam serves to excite the upper energy levels of beam atoms. Scanning the laser wavelength allows measuring the magnetic field at a given point from an outburst of induced emission. Combined diagnostics for measuring weak fields in plasma facilities with a relatively high pressure are a quite realistic objective. At present, ultra-

Table 1. Characteristics of diagnostic injectors.

Injector	DINA-5F	DINA-6 and -7	RUDI (TEXTOR)	RUDI (TCV)	RFX injector
Year of creation/ modernization	2001	1996	1998/ 2014	1999	2004
Energy of atoms, keV	30 (H) 20 (He)	30; 40	50	53	50
Ion current, A	4 (H) 4.5 (He)	2.5; 1.8	1.7	2.7	5.5
Duration, s	0.0035	20×10^{-3}	10	2	0.05
Focal length, cm	130	250; 400	400	400	400
Atom flux density at the beam focus, mA cm^{-2}	210 (H) 300 (He)	50; 15	15	20	50
Beam modulation	None	66 Hz	External	External	External
Beam composition $H^+/H_2^+/H_3^+$, %	90/5/5	90/5/5	60/20/20	60/20/20	90/5/5
Diagnostic procedures	Rutherford scattering, impurity spectroscopy, Stark effect	Impurity spectroscopy	Emission spectroscopy, impurity spectroscopy	Impurity spectroscopy	Emission spectroscopy, impurity spectroscopy, Stark effect

small energy spread (less than 50 eV for a deuterium atom beam with an energy of 50 keV and a flux of 4 A equiv.) is achieved using the DINA-5M injector by virtue of active voltage stabilization in a high-voltage modulator [136]. This spread in energy corresponds to the lower boundary ($\sim$ 30 G) of the magnetic field being measured.

Characteristics of certain diagnostic injectors are collated in Table 1.

Injector of high-brightness hydrogen fast atom beams for a source of polarized H^- ions. An injector of high-brightness hydrogen atom beams based on diagnostic injectors with a plasma emitter having low transverse ion temperature and formed by a collisionlessly expanding plasma jet from an arc plasma generator and multiaperture IOS with ballistic focusing was developed and tested for a source of polarized H^- ions with optical pumping at Brookhaven National Laboratory [137]. In the source of polarized H^- ions with optical pumping, polarization of atoms with an energy of several keV occurs as protons capture polarized electrons of optically oriented rubidium in a 2.5–3 T magnetic field. An intense proton beam in the magnetic field is formed by stripping the focused high-brightness hydrogen atom beam injected into a solenoid in a helium cell. The hydrogen atom beam is produced by an injector placed outside of the solenoid.

The brightness of ion beams formed in the ion sources of diagnostic injectors with an energy of 20–30 keV was limited by the current emission density of $\sim 100-200$ mA cm^{-2}. In an injector of atomic beams for the source of polarized ions with optical pumping, a high normalized brightness of the proton beam was reached owing to enhanced current emission density and small beam angular divergence at a relatively low energy of protons. The injector of a high-brightness hydrogen atomic beam, schematically depicted in Fig. 40, produces a focused beam of hydrogen atoms with an energy of 5–8 keV, equivalent current of 2–3.5 A, pulse duration of 500 μs, and a repetition rate of 1 Hz. A plasma emitter with a low ion transverse temperature ($\sim$ 0.2 eV) is created in the proton source by a hydrogen plasma jet outflowing from the anode hole of the arc generator. Due to the large expander volume, the density of hydrogen atoms outflowed from the source is rather small, and the plasma jet weakly interacts with the effluent gas. The plasma jet is formed in the arc generator with a cold molybdenum cathode analogous to that described in Ref. [115]. The proton beam in the injector is formed by the fine-structure multiaperture four-electrode ion-optical system with ballistic focusing. The unit cell of the IOS was optimized with the aid of the PBGUNS numerical code. The grids are made from 0.38-mm thick molybdenum plates. Each IOS electrode has 1866 holes 0.8 mm in diameter making up a hexagonal structure with a step of 1.1 mm and diameter of 5 cm. The transparency of the ion-optical system is 50%. The holes in the electrodes are made by photoetching, and the spherical electrodes are shaped by heat stamping in a vacuum at the Mo recrystallization temperature (1100 °C). Radii of curvature of the plasma, extracting, and accelerating electrodes are 180, 140, and 100 cm, respectively. The electrodes are carefully welded to the stainless steel holders with the aid of a pulsed

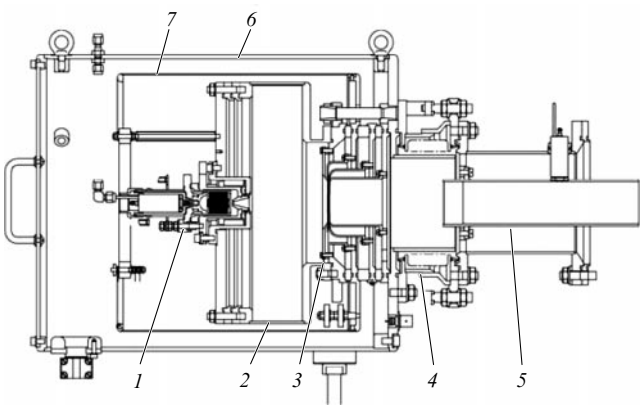

Figure 40. Fast atom injector: *1* is the arc plasma generator, *2* — expansion chamber, *3* — IOS, *4* — adjusting unit, *5* — charge-exchange target, *6* — outer magnetic screen, and *7* — inner magnetic screen.

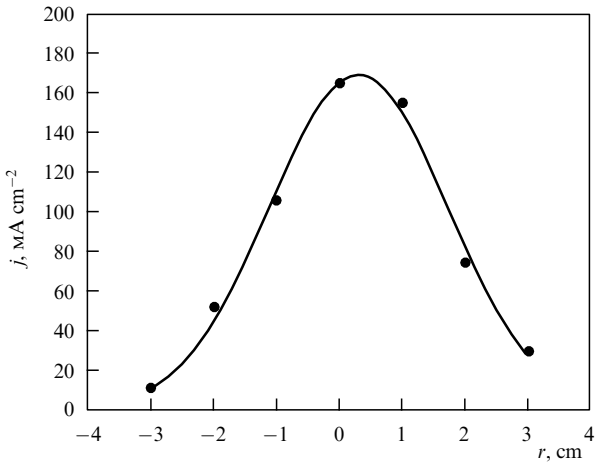

Figure 41. Measured atom flux density profile 200 cm from the ion-optical system.

CO_2 laser. The gaps between the electrodes in the center of the IOS are 0.5 mm, 1.4 mm, and 0.6 mm. The voltage across the plasma electrode is close to voltage U of the high-voltage modulator applied to the anode; the voltage across the extracting and accelerating electrodes is $0.9U$ and $0.02U$, respectively.

The newly formed proton beam undergoes charge exchange on hydrogen atoms outflowing from the expansion chamber through IOS electrodes and additional holes in the electrode holders. The final charge exchange of beam ions occurs in the pulsed gas target of the neutralizer. The pulsed gas valve is located directly on the neutralizer tube to facilitate gas feeding into the target.

The fast atom source was tested at an atom energy of 5–8 keV and equivalent beam current of 2–3.5 A [138]. The beam angular divergence and focal length were found from beam intensity profiles measured by secondary emission detectors at two distances. Figure 41 shows a beam atom flux density profile measured at a distance of 200 cm from the IOS. It is fairly well approximated by the Gaussian curve. The local angular divergence of the beam was 10 mrad, and the focal distance was 200 cm. The measured values agree with the theoretical ones. Results of the test give evidence that the time of reliable continuous operation of the source depends on erosion of the cold cathode in the arc generator. Durability testing showed that a cathode undergoing arc erosion becomes inoperable after $\sim 10^7$ discharge pulses with an arc current of 420 A. A cathode operating at a 1-Hz repetition rate should be replaced after 3–4 months of continuous work.

The injector of hydrogen fast atom beams has been in operation since 2013 in the source of polarized ions with optical pumping of the Relativistic Heavy Ion Collider (RHIC) [139].

Successful experiments on generating intense low-energy hydrogen negative ions were carried out with an injector of a focused high-brightness hydrogen atom beam. The ion source of this injector formed a proton beam with an energy of 10 keV, 4.7 A current, emission current density of 470 mA cm^{-2}, and focal length of 200 cm. The beam thus obtained was further sent to the hydrogen target for a charge exchange. The measured current of hydrogen negative ions flowing through a diaphragm 2 cm in diameter placed at a distance of 200 cm was 75 mA, i.e., much higher than in the case of conventional beam transport. This can be accounted for by the efficient transport of the negative ion beam in the positive potential of the beam plasma. It is expected that the hydrogen negative ion beam current at an energy of 20–30 keV can reach a few hundred milliamperes.

5. Development of the surface-plasma method for generating intense negative ion beams

5.1 Pilot studies designed to produce negative ions from discharges in crossed fields

Active pilot studies aimed at the elaboration of new methods for producing negative ion beams were carried out at BINP in parallel with the development of hydrogen negative ion sources for charge-exchange injection (see Section 2). Specifically, investigations of plasma sources with discharges in crossed fields were initiated. It was known by that time that such discharges can be used to create thin sheets of dense plasma with an elevated electron temperature. Electron-induced dissociation of molecules in such sheets was associated with the efficient formation of negative ions and their escape to the periphery of the plasma sheet [7].

The layout of the source with a magnetron geometry of electrodes proposed by G I Dimov in 1965 is depicted in Fig. 42. The gas-discharge chamber (GDC) of the source consisted of concentric electrodes (inner — cathode, and outer — anode). Hydrogen was fed into the GDC using a pulse valve designed at BINP [66] through a channel in the anode. The source was placed in the center of a magnetic field up to 0.1 T created by Helmholtz coils. A negative 2–10 kV potential was applied to the GDC casing and the accompanying electron interception plates, while the extracting electrode was grounded.

Langmuir probes were adapted to measure plasma potential and density, as well as the electron temperature in the discharge of the cylindrical magnetron. It was found that the electron temperature in the near-cathode region amounted to 7–10 eV, but decreased to 1–2 eV closer to the anode.

In 1967, an H^- ion beam with a current up to 1 mA was obtained from this source with a pulsed magnetron discharge (current 4 A, voltage 675 V, hydrogen pressure ~ 0.5 Torr) through 0.7×15-mm emission slit oriented parallel to the cathode axis.

In 1969, the cylindrical magnetron source was modernized (Fig. 43) by introducing a three-electrode system for negative ion beam extraction and formation: a voltage up to 5 kV was

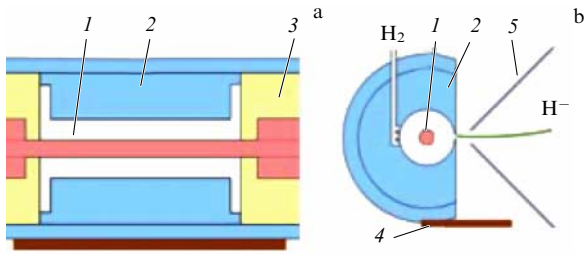

Figure 42. Layout of cylindrical magnetron source. (a) Axial section along the magnetic field. (b) Section across the magnetic field: *1* is the cathode, *2* — anode with holes for feeding gas and a slit for negative ion extraction, *3* — end insulators, *4* — plate for intercepting accompanying electrons, and *5* — extracting electrode.

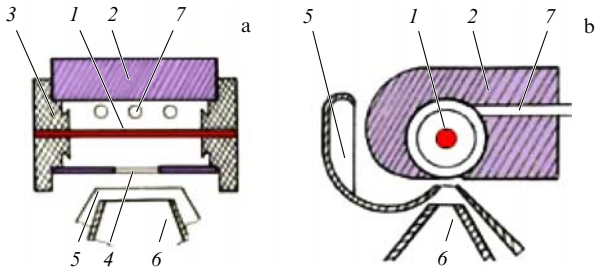

Figure 43. Modernized cylindrical magnetron. (a) Section along the magnetic field. (b) Section across the magnetic field: *1* — cathode, *2* — anode, *3* — end insulators, *4* — emission slit, *5* — extracting electrode, *6* — accelerating electrode, and **7** — gas input channels.

applied across the extracting electrode, and up to 15 kV across the accelerating electrode.

To improve interception of the accompanying electrons, a ridge was formed at the extracting electrode to dump electrons along the magnetic field. The geometry of the end insulators was also altered so that their sputtering with the cathode material could not establish a short circuit across the interelectrode gap. Annular probes mounted at the discharge ends were used to measure plasma potential distributions along the radius of the discharge channel.

The typical plasma potential distribution along the radius of the cylindrical magnetron discharge is plotted in Fig. 44. This confirmed the fact that magnetron discharge plasma has an electric field fostering negative ion displacement to the plasma periphery. This evidence, together with the presence of hot electrons near the cathode and colder electrons in the beam extraction region discovered earlier, threw light on conditions in the magnetron discharge that promote the intense generation of negative ions.

The modernized source with a 1×10-mm^2 longitudinal emission slit (Fig. 43) produced an H^- ion beam with a current up to 7 mA and pulse duration of 1 ms with the accompanying 250-mA electron flux extracted together with negative ions.

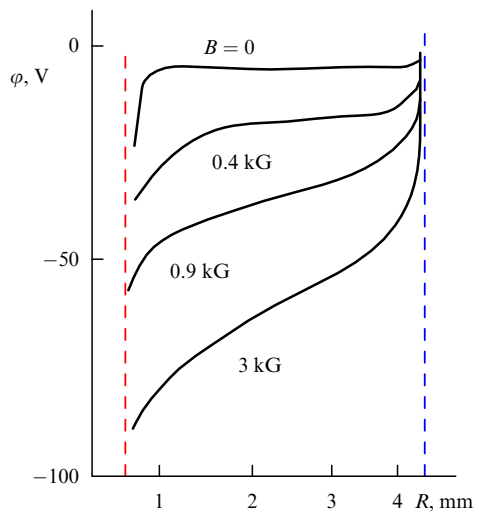

Figure 44. Potential distribution along discharge channel radius. Numbers alongside the curves denote magnetic field value in the discharge region. Dashed straight lines show positions of cathode ($R = 0.5$ mm) and inner anode ($R = 4.5$ mm) surfaces.

In 1971, the geometry of gas-discharge electrodes in the magnetron source was radically altered. It was proposed to use a magnetron discharge with a plane cathode (planotron) to increase the width of the plasma sheet and negative ion extraction region. This new source is depicted in Fig. 45.

The cathode was shaped like a flattened spool with a plane central part and end plates (*1* and *1a* in Fig. 45). Projections from the cathode side plates restricted the discharge zone from the ends and maintained electron oscillations in the magnetic field of a discharge. Such a geometry made possible the closed drift of electrons in crossed electric and magnetic fields around the central flat part of the cathode. The size of the tantalum cathode was increased to 16 mm in the direction perpendicular to the magnetic field, while the length of the electron oscillation zone along the magnetic field between the plates was shortened to 10 mm. The enlargement of the cathode in the direction perpendicular to the magnetic field made possible negative ion extraction through emission slits oriented along the length normally to the magnetic field lines. This slit orientation ensured a more efficient absorption of electrons on its side walls and a reduction in the accompanying electron flux extracted together with the negative ions.

To suppress the electron flux entering the emission slit from the plasma by diffusion across the magnetic field, anode protrusions were installed in the anode region of the discharge; this region adjoined the emission slit and protrusions formed the near-anode region with lowered electron temperature and plasma density (*2a* in Fig. 45).

The smaller size of the gas-discharge chamber along the magnetic field allowed using electromagnets with profiled pole tips and optimizing the geometry of the magnetic field in the negative ion generation and beam formation area. It turned out that the electric strength of the source increased if a nonuniform magnetic field with dome-shaped force lines in the direction from the extraction electrode to the anode was created in the extraction region. To form the concave field, pole tips with projections were used (*6* in Fig. 45). Such a field prevented oscillations and the accumulation of electrons in the ion extraction region and ensured a rapid dump of electrons from the extracting gap onto the extraction electrode (*4* in Fig. 45).

A reduction in the flux of accompanying electrons and special profiling of the magnetic field ensured high electric strength of the source extraction gap and allowed the operational range of discharge parameters and extracting voltages to be expanded.

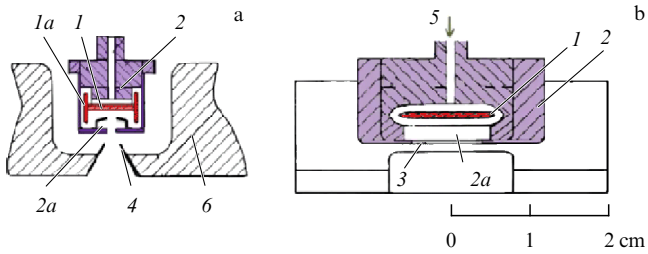

Figure 45. Layout of a negative ion source with the planotron geometry of electrodes. (a) Section along the magnetic field. (b) Section across the magnetic field: *1* is the central part of the cathode, *1a* — cathode side plates, *2* — anode, *2a* — near-anode cavity, *3* — emission slit, *4* — extracting electrode, *5* — gas input channel, and *6* — magnet pole tips.

A discharge in the planotron source with a flat tantalum cathode generated a hydrogen negative ion beam with a 4.5-A current and maximum negative ion current density of 90 mA cm^{-2} in emission slits. The accompanying electron flux did not exceed 16 mA. This experimentally observed fact of the manyfold reduction in the accompanying electron flux was crucial for the further development of negative ion sources. The data obtained confirmed promising prospects for the use of high-current discharges in crossed fields for bulk generation and extraction of negative ions.

5.2 First sources with cesium addition

Pilot experiments on the extraction of negative ions from discharges in crossed fields, including the introduction of various hydrogen-containing molecules and alkali metal hydrides into GDC, were carried out in 1969–1971. Sources with planotron and Penning geometry of electrodes were tested under conditions of diborane (B_2H_6) feeding, thermal decomposition of lithium hydride (LiH) and cesium borohydride ($CsBH_4$), metallic cesium evaporation, and cesium release from cesium chromate–titanium ($Cs_2CrO_4 + Ti$) pellets.

An experiment with a cesium pellet attached to the central cathode plate (*1* in Fig. 45) proved successful. Pellet heating in a high-current pulsed discharge caused cesium release and a 3-to-4-fold increase in the current of negative particles extracted from the planotron source.

Further work was aimed at elucidating factors influencing the intensity of negative ion generation in high-current discharges upon cesium addition, and targeted modification of the modes of cesium delivery into the discharge and GDC geometry resulted in a manyfold increase in extracted current [16]. The following changes were introduced in the design of the planotron source for this purpose (Fig. 46).

(1) To enhance generation of negative ions, cesium vapors were fed into GDC from pellets placed in the cathode cavity. The central plate of the cathode was shaped like a pencil case *1* (Fig. 46a) with cesium pellets placed in it. Uniform heating of the pencil case and the tablets by the discharge led to the distributed delivery of cesium onto the emission surface through longitudinal slits between the case and its cover.

(2) The cathode was made of molybdenum, known to efficiently capture cesium from the ion flux bombarding the cathode and to be resistant to discharge breakdown into an arc. The use of molybdenum facilitated the formation of a stable Cs coating at the cathode and supported the work of the pulsed planotron discharge at much higher discharge currents without discharge breakdowns into the low-voltage arc regime.

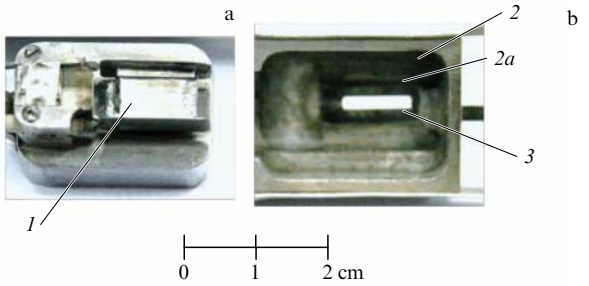

Figure 46. First surface-plasma source with the planotronic geometry of electrodes. (a) Cathode attached to anode base. (b) Anode frame with emission slit. *1* — central cathode plate, *2* — anode frame, *2a* — side protrusions forming near-anode cavity, and *3* — emission slit. Extracting electrode and magnet poles are not shown.

(3) It was stated that cesium feeding to the discharge should be followed by source electrode training with high-current discharges that ensure cesium redistribution over the cathode surface and optimization of its cesium coating.

(4) The experiments made it possible to determine the optimal geometry of the near-anode cavity for the more efficient extraction of negative ions. It was shown that lateral protrusions or the side walls of the anode insert (*2a* in Fig. 46) must delimit the near-anode cavity from the ends and allow negative ions to draw together from the plasma in the emission slits.

These innovations enabled the beam current from the planotron source with 1×10-mm^2 emission slits to be amplified from 15 to 300 mA, with the accompanying electron flux being lower than the negative ion beam current [16].

To determine the operational characteristics of the planotron source in the purely hydrogen regime, an analogous planotron with an Mo cathode and 'open' near-anode cavity was created and used in experiments in a vacuum chamber cleaned to remove all traces of cesium. In the purely hydrogen regime of experiments in a vacuum chamber, this planotron source with a 500 V voltage and 80 A current produced a hydrogen negative ion beam with a 22 mA current and maximum hydrogen negative ion current density in the emission slit of 0.27 A cm^{-2} [140]. The accompanying electron current was below 100 mA.

A comparison of results obtained in purely hydrogen [140] and mixed hydrogen–cesium [16] regimes revealed that the addition of cesium into a discharge with a planotronic geometry of electrodes increased hydrogen negative ion beam current by a factor of 10 or more; simultaneously, the optimal hydrogen density in the discharge decreased by a factor of 5, while both discharge voltage and power dropped threefold.

Such significant improvement in characteristics of negative ion sources gave an impetus to research on the surface-plasma mechanism of negative ion generation and contributed to further perfection of surface-plasma sources.

5.3 Surface-plasma mechanism of negative ion generation in high-current discharges

To elucidate mechanisms of intense negative ion generation discovered in high-current discharges, characteristics of the source were evaluated using electrodes of various geometries and materials, as well as different methods of cesium feeding into the discharge and different configurations and strengths of the magnetic field. The energy spectra of extracted negative ions and intensities of hydrogen and cesium ion fluxes to gas-discharge electrodes were measured [141, 142].

One of the key facts in favor of the surface origin of the negative ion flux being generated was the discovery of two characteristic groups in the energy spectrum of the resultant beams, corresponding to the cathode and anode regions of negative ion generation in the discharge (Fig. 47).

The energy of the low-energy group of accelerated H^- ions (left part of Fig. 47) corresponded to the extracting potential, i.e., these ions formed at the anode or in the near-anode region of the discharge. The position of this group was unrelated to the discharge voltage and its intensity increased with increasing hydrogen feeding into the discharge (Fig. 47b). The energy spread for the anode group was

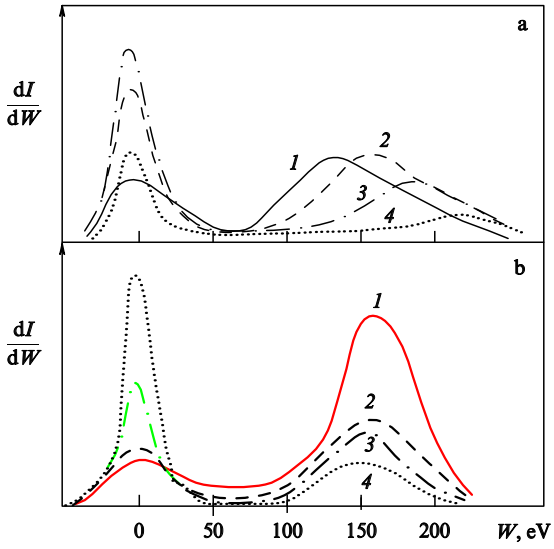

Figure 47. Energy spectrum of a beam of negative ions from a planotron source (a) at different discharge voltages: *1* — 120 V, *2* — 150 V, *3* — 160 V, and *4* — 210 V; (b) at different hydrogen inputs (molecules per pulse): *1* — 10^{16}, *2* — 1.2×10^{16}, *3* — 1.7×10^{16}, and *4* — 2.2×10^{16}. Ion energy $W = 0$ corresponds to the anode potential.

characterized by the level of discharge voltage fluctuations. The position of the group with higher-energy ions (right part of Fig. 47) corresponded to the cathode potential and varied with changes in discharge voltage. The intensity of the cathode group of negative ions decreased with a rise in discharge voltage, i.e., with making thinner the cathode cesium coating. The energy width of the cathode group was several times that of the anode group, which suggested a wide energy scatter of negative ions formed at the cathode.

It was revealed that the removal of the central cathode plate and the work of the source in the Penning discharge regime resulted in a twofold decrease in intensity of the extracted hydrogen negative ion beam, while the energy spectrum of extracted negative ions contains only the anode group. This intense generation of negative ions in the near-anode region found application in the development of Penning sources of negative ions for accelerators (see below). In the source with a purely hydrogen discharge, most extracted negative ions had an energy corresponding to the extracting potential.

Direct extraction of positive ions through a cathode hole in the source with the Penning geometry of electrodes confirmed that in high-current discharges in crossed fields, the ion current to the cathode accounts for the main part of discharge current, while discharge voltage is concentrated largely in the narrow near-cathode layer, with a discharge voltage drop responsible for the acceleration of positive ions toward the cathode and the maintenance of the discharge by virtue of secondary emission at the cathode [143].

The analysis of factors influencing the intense generation of negative ions in discharges and the above characteristics of the energy spectrum of negative ions extracted from discharges in crossed fields allowed formulating the following major components of the surface-plasma mechanism underlying this generation [142, 144, 145]:

(1) intense generation of negative ions in gas discharges is due to their emission from electrodes as a result of plasma-surface interaction in the discharge;

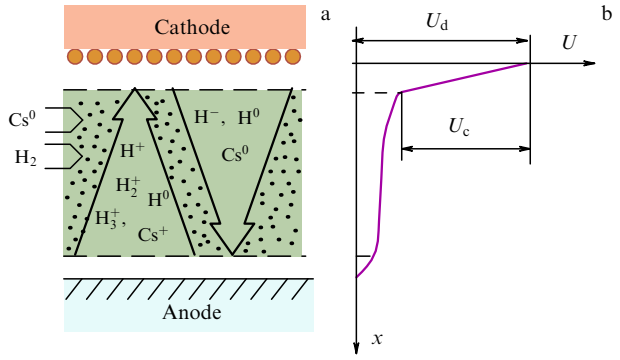

Figure 48. (a) Schematic of the surface-plasma generation mechanism and H^- ion collection in a discharge with narrow near-electrode layers. (b) Potential distribution in the interelectrode gap. U_d is the discharge voltage, and U_c is the near-cathode voltage drop.

(2) the plasma maintains the bombardment of the electrodes by fast ions and atoms needed for conversion into negative ions, while the electric fields of narrow near-electrode layers of the discharge ensure acceleration of intense positive ion fluxes from the plasma onto the emitting electrode, and the negative ions being formed from the emitting electrode into the plasma and the extraction region;

(3) the bombardment of the emitter surface by fast plasma particles, including cesium ions, promotes the formation and maintenance of the optimal cesium coating at the emitting electrode responsible for generating negative ions;

(4) reflection of plasma particles and hydrogen dispersion from the near-surface layer of electrodes give rise to intense secondary particle flows leaving the surface with an elevated energy ($1-10^2$ eV);

(5) the enhanced speed with which secondary particles move away from the surface is responsible for the high degree of their ionization, even for ions with a low electron affinity (see Section 5.4);

(6) the additional acceleration of intense secondary negative ion fluxes by the narrow layer of the near-electrode potential drop and the electric field with a high strength in the layer provides for the transport of negative ions through the plasma and their collection in the beam formation/extraction zone.

A schematic diagram of the surface-plasma mechanism illustrating H^- ion generation in a hydrogen–cesium discharge with narrow near-electrode layers is presented in Fig. 48.

This mechanism gave the name surface-plasma sources (SPSs) to such devices. The discovery of intense generation of hydrogen negative ions on the electrode surface in a gas discharge stimulated numerous studies of elementary negative ion emission processes. Specifically, particle charge states were investigated in the processes of sputtering and reflection from the surface under different conditions, including those that resemble processes realized in the negative ion sources. A comprehensive bibliography and the main results of this work are presented in reviews [146, 147].

5.4 Kinetic emission of negative ions

One of the first theoretical studies that demonstrated the mechanism and presented calculations of the thermodynamically nonequilibrium kinetic emission of negative ions from a metal surface for $S < \varphi$ (where S is the electron affinity of an atom, and φ is the surface work function) was done at BINP

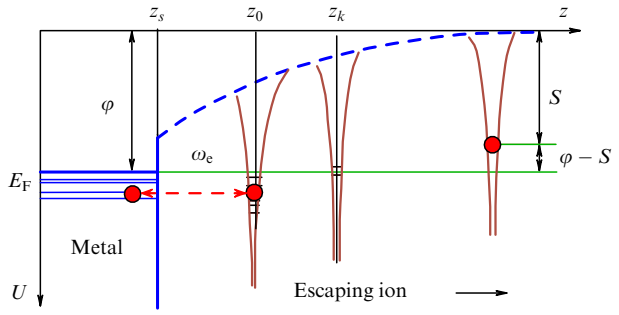

Figure 49. Model of thermodynamically nonequilibrium kinetic emission of negative ions.

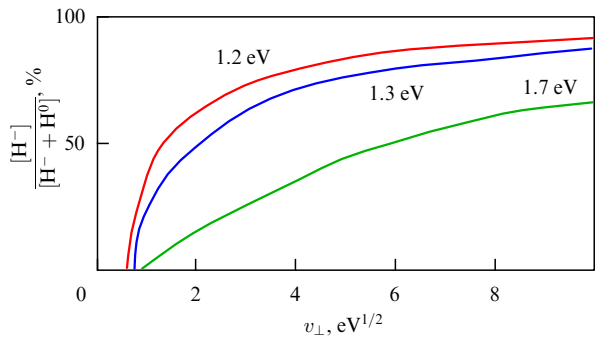

Figure 50. Degree of hydrogen negative ionization in the case of kinetic emission from a metal surface plotted versus the initial speed of negative ion movement away from the emitters with work functions 1.2, 1.3, and 1.7 eV, respectively [148].

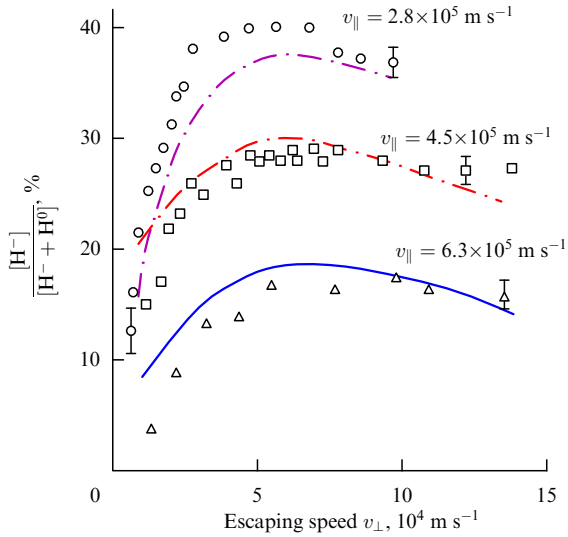

Figure 51. Degree of hydrogen particle negative ionization in the case of their reflection from a W + Cs surface versus initial speed of movement away from the emitter for three incident proton speeds parallel to the emitter. Curves — calculated results, and symbols — experimental data [150].

[148]. Kinetic emission was calculated in Ref. [148] using the plane conducting surface approximation with a potential well for metal electrons located behind it. The model of thermodynamically nonequilibrium kinetic emission of negative ions is schematically presented in Fig. 49. It shows the near-surface barrier of image forces associated with emission of a charged particle and the relative position of outer electron energy levels in a negative ion for three different distances from the metal surface. The potential well of electrons in the metal is bordered by a plane conducting surface with the z_s coordinate. Part of the work function φ of electrons leaving the metal is given by the image force potential (dashed curve); z_0 is the initial position of a negative ion. The figure shows that the electron affinity level for $z > z_k$ is above the Fermi level in the metal.

To leave the metal, the electron must perform work function φ, part of which is the image force potential $-e^2/(4z)$ (dashed curve in Fig. 49). The outer electron level in a negative ion lowers near the metal surface and broadens as shown for three characteristic positions of negative ions, denoted by circles in Fig. 49. In an atom near the metal surface, the outer electron level can descend below the Fermi level E_F of electrons in the metal, so such an electron can pass from the metal onto the level in the negative ion. To be able to emit, the negative ion must have a kinetic energy higher than $\varphi - S$, which it can acquire in sputtering and reflection processes.

The outer electron energy level in the negative ion heightens with distance from the surface and becomes higher than the Fermi level in metal for distances $z > z_k$ (see Fig. 49). The rate of electron exchange between the ion and the metal, i.e., the width of the electron affinity level, decreases exponentially with distance from the surface: $\omega_e = \omega_0 \exp(-z/\lambda)$. To capture an electron at the electron affinity level during movement away from the surface, the atom must pass through the capture area $z_k - z_0$ for a time longer than electron exchange time $1/\omega_{e1}$; to conserve the electron at the affinity level, the atom must rapidly (for time $< 1/\omega_{e2}$) move away over the distance $z - z_k + 3\lambda$, where electron exchange practically stops.

The model was applied to calculate the formation of hydrogen negative ions for the case of nonequilibrium kinetic emission. Relevant formulas for the fraction of negative ions in a flow of hydrogen particles leaving the surface with the work function φ were derived in Ref. [148]. The fraction of negative ions in a flux of hydrogen particles leaving the surface was calculated using these formulas and is shown in Fig. 50 for different work function values, depending on the initial speed of the particle moving away from the surface. It follows from the figure that the degree of hydrogen negative ionization may be higher than 15% at an initial energy of > 4 eV of negative ions flying off and emitter work function of < 1.7 eV; it increases appreciably as the emitter work function continues to decrease. Measurements of the degree of negative ionization of hydrogen particles in the case of slide reflection from W + Cs surfaces performed in 1982–1985 showed that the degrees of negative ionization calculated by M E Kishinevskii [148] agree with the experimental data within the range of initial escape energies $E < 15$ eV [149].

Further development of the theory of kinetic emission of negative ions and experimental studies on the charge composition of secondary emission particles showed that, at high velocities of particles incident on the emitter, the speed of an incident ion parallel to the emitter surface also affects the efficiency of negative ion formation. The observed degree of hydrogen negative ionization in the case of reflection from the W + Cs surface depending on the initial escape velocity of negative ions and the respective calculated curves are presented in Fig. 51 for three incident particle speeds parallel to the emitter [150].

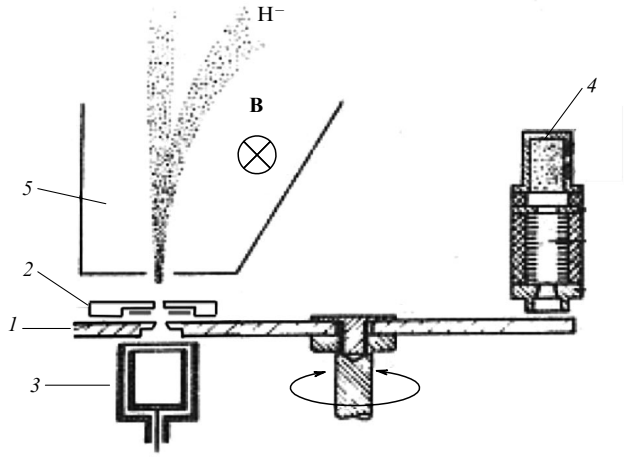

Figure 52. Schematic of experiment to study the emission of H^- ions upon activation of the emitter surface by hydrogen plasma: *1* — rotating emitter, *2* — cesium ion and atom feed unit, *3* — cesium ion flux meter, *4* — plasma gun, and *5* — magnet poles [152].

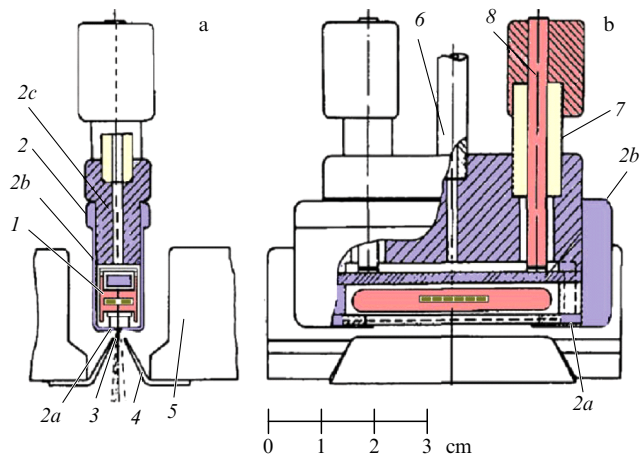

Figure 53. Modified planotron source with lengthened electrodes. (a) Section along the magnetic field. (b) Section across the magnetic field: *1* — cathode with a hollow central part, *2* — anode frame, *2a* — anode insert with an emission slit shaping the near-anode cavity close to the emission slit, *2b* — inner anode creating an electric field above a cathode, *2c* — anode frame, *3* — emission slit, *4* — extracting electrode, *5* — magnet poles, *6* — gas feeding tube, *7* — anode–cathode insulators, and *8* — cathode holders.

A series of experiments designed to study kinetic emission of H^- ions during bombardment of tungsten and tantalum emitters by accelerated Cs^+ ions was conducted by BINP researchers in 1975–1977 [151, 152]. To reduce the emitter surface work function, cesium ions were fed continuously either by sputtering or through emitter pores.

The schematic of an experiment on the activation of the emitter surface by hydrogen plasma is presented in Fig. 52. A rotating disk was utilized as the emitter of H^- ions. The site of interest on the disk was successively exposed to the source of cesium vapors, then to the plasma gun to introduce hydrogen onto the surface, and thereafter to the source of cesium ions with an energy of 1–2 keV. Hot tungsten plates were used for cesium surface ionization. Positive voltage (1–2 kV) with respect to the rotating disk was applied to the cesium feeder (*2* in Fig. 52) to accelerate Cs ions toward the emitter. The same voltage was used to extract from the emitter surface H^- ions formed via sputtering of hydrogen introduced into the emitter; the ions were analyzed following separation in the magnetic field [152].

In experiments on negative ion desorption from a hydrogen plasma-activated Mo–Cs emitter, the secondary emission coefficients of hydrogen negative ions were $Y^- = 1.2-1.45$ [152], i.e., 2–3 times larger than those observed earlier in studies on the sputtering of the coat formed by cesium and hydrogen deposition from a gas over the surface [151]. The data obtained provided a basis for the creation of a continuously operating sputter type source of H^- ions that generated negative ions by virtue of secondary ion–ion emission [152].

Experiments conducted with this device confirmed the high efficiency of surface negative ion generation under conditions of electrode surface bombardment by H–Cs plasma.

5.5 Pulsed surface-plasma sources with H^- generation at gas-discharge electrodes and at an emitter with an independent potential

In subsequent modifications of the planotron source, gas-discharge electrodes and their holders were made more rigid, which allowed increasing their size severalfold in the direction perpendicular to the magnetic field and reducing the gap between the central cathode plate and the anode insert that determines the thickness of the dense plasma sheet, i.e., the destruction of negative ions formed at the cathode during their movement to the emission slit.

In the planotron shown in Fig. 53, the central cathode plate was enlarged to $40 \times 4 \times 6\ \text{mm}^3$, which, in turn, enabled the length of the emission slits to be increased to 30 mm, while the gap between the central plate and the anode insert determining the thickness of the dense plasma sheet decreased to 0.5 mm. Such a source with $0.9 \times 30\ \text{mm}^2$ emission slits produced an H^- ion beam with a 880 mA current [17, 153] and a ~ 1.7-A flux of accompanying electrons.

A planotronic source with the geometry shown in Fig. 53 was tested in experiments on negative ion extraction from a $3 \times 10\text{-mm}^2$ wide slit separated into sections by 0.7-mm wide plates. The negative ions were extracted from the sectioned slit with the aid of a single-aperture electrode. This planotron produced a negative ion beam with a 1 A current; it was possible to maintain an extracting voltage of 50 kV at the 3-mm high extracting gap [153].

The experimentally obtained fact of intense negative ion generation from a high-current discharge with the Penning electrode geometry and small negative ion energy scatter in the beam [16] was employed to design and create intense pulsed sources of H^- ions for accelerators [154]. Later on, Penning discharges with hollow cathodes were used to develop stationary sources of negative ions for accelerators [155]. A schematic of a pulsed Penning surface-plasma source (SPS) developed at BINP is presented in Fig. 54 [154, 156].

The source produced H^- ion beams with a nominal intensity of 100 mA, pulse length of 100–250 μs, and repetition rate up to 100 Hz [156]. The failure-free service life of the source reached 10^8 pulses. In the Penning surface-plasma source, only a small part of the negative ions formed at the cathode and accelerated toward the plasma by the near-cathode potential can enter the emission slits. The recorded intense H^- ion beam forms in the near-anode region by

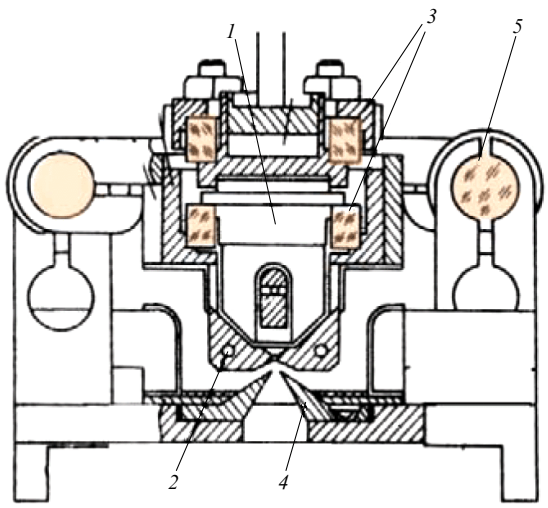

Figure 54. Schematic of a pulsed Penning SPS: *1* — cathode, *2* — cooled anode, *3* — cathode–anode insulators, *4* — extracting electrode, and *5* — high-voltage insulator.

resonant charge exchange of fast 'cathode' ions on the atomic gas and also due to conversion of atoms on the anode surface close to the emission slits. The two processes, i.e., charge exchange in the near-anode region and generation at the anode, yield negative ion beams characterized by small energy scatter. Careful optimization of the beam extraction/formation conditions in the Penning source allowed H^- ion beams to be obtained with a record-breaking normalized brightness of 3×10^7 A cm^{-2} rad^{-2} [157]. The pulsed source with the Penning geometry of electrodes developed at BINP was installed at the 600 MeV linac of the Moscow meson factory [158] and became a prototype for analogous sources used at meson factories in Los Alamos [159] and Oxford [160].

The next step in the development of surface-plasma sources at BINP was the design of an SPS with high-current discharge and an emitter with an independent potential [144] (Fig. 55). The narrow plasma sheet was created by a reflective discharge in the magnetic field with hollow cathodes. Both hydrogen and cesium were fed through canals in hollow cathodes. The independent emitter of negative ions was placed with a small gap ($\delta = 0.1 - 1$ mm) close to the plasma sheet boundary determined by the size of windows in the anode inner casing. Cesium was delivered to the surface of the independent emitter with the aid of an additional cesium source. Extraction of negative ions was performed by a single-aperture extracting electrode (not shown in Fig. 55) through a sectioned emission slit located opposite the emitter.

Negative bias voltage with respect to anode (up to ~ 300 V) was applied to the emitter, which determined both the current and energy of positive ions extracted from the plasma sheet and bombarding the emitter. The maximum current in the emitter circuit recorded at emitter voltages $> 80 - 100$ V amounted to 80 A, which was roughly 20% of the reflective discharge current. In this case, the main part of the current in the emitter circuit (up to 90%) was constituted by positive ions, whereas secondary electrons were deflected in the magnetic field and returned to the emitter.

The current of the beam of negative ions from the source with the independent emitter of negative ions depended on the reflective discharge current, the distance between the emitter and the plasma sheet, and the emitter voltage [144]. Variations of emission density of negative ion current obtained from the source with an independent emitter and 3×30-mm^2 sectioned slit, depending on the emitter voltage, are illustrated in Fig. 56. At a relatively short distance ($\delta = 0.7$ mm) between the emitter and the plasma sheet (bottom curve in Fig. 56), the negative ion beam current did not depend on the emitter voltage and was determined by the processes of negative ion formation in the near-anode region characteristic of the Penning SPSs (see above). As the emitter approached as close to the plasma layer as $\delta = 0.1$ mm (top curve in Fig. 56), the negative ion beam current increased with U_{em} and became saturated at $U_{em} \approx 70 - 80$ V. A 2.5-fold increase in negative ion current density associated with a rise in emitter voltage was due to both the enhanced generation of negative ions on the emitter surface as a result of positive ion acceleration and the increased generation of negative ions on the walls of sectioned emission slits related to the flow of fast particles reflected from the emitter surface.

At small emission slits, from the source with an independent 0.37×10-mm^2 emitter and a reflective discharge with a 450-A current, a negative ion beam was produced with the emission density of 5.4 A cm^{-2} [144] that was ≈ 1.5 times higher than that obtained earlier in the planotron source. On the whole, however, the energy efficiency of negative ion generation in the source with an independent emitter was

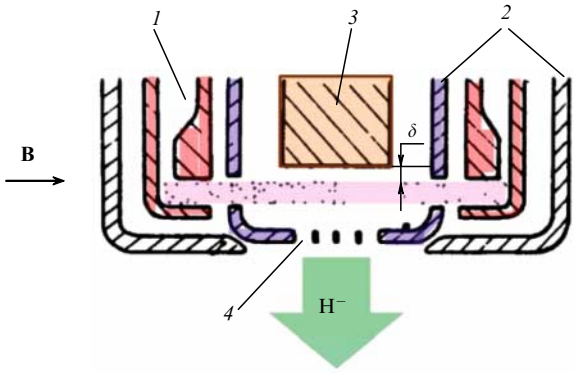

Figure 55. Negative ion source with an independent emitter: *1* — hollow cathodes, *2* — inner and outer anode frames, *3* — emitter with controlled bias voltage with respect to anode, and *4* — sectioned emission slit.

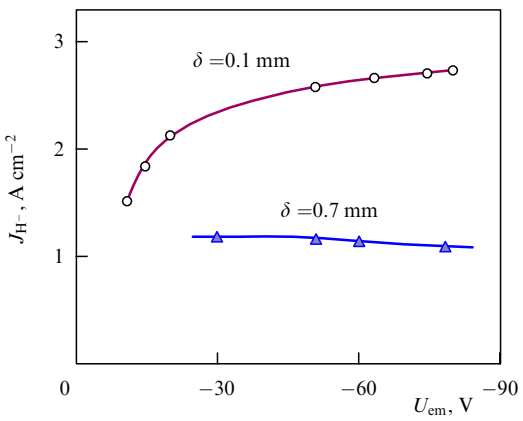

Figure 56. Dependence of current emission density j_{H^-} of negative ions extracted from a source with an independent emitter as a function of voltage U_{em} across an emitter. Values alongside the curves denote gaps δ between the emitter and plasma sheet in mm.

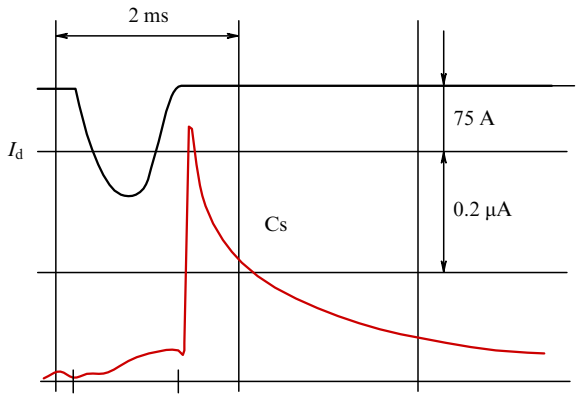

Figure 57. Oscillogram of discharge current I_d and Cs atom flux from the emission slit recorded by a surface ionization detector [164].

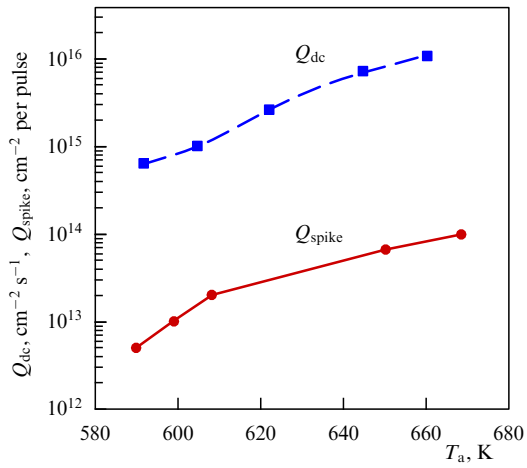

Figure 58. Stationary thermodesorption cesium flux Q_{dc} from the source and the amount of cesium Q_{spike} carried out in a pulse after switching off the discharge plotted vs anode temperature T_a [165].

rather low, while the maintenance of the optimal cesium coating on the surface required much greater amounts of cesium to be introduced into the emitter region.

Since 1980, the development of a stationary source of negative ions with multipole plasma confinement and negative ion generation at the independent emitter (converter) has been based at the Lawrence Berkeley National Laboratory (Berkeley, USA) [161]. Other such sources have been successfully employed for charge-exchange injection of negative ions in proton accelerators in Japan and the USA [162, 163].

Cesium behavior in high-current SPS discharges was studied by measuring Cs ion fluxes onto the source electrodes, evaluating the consumption of cesium atoms passing through the emission slits, and identifying the spectral lines of cesium atoms and ions. A surface ionization detector of cesium was used to measure its flux outgoing through the source emission slit [164]. These studies confirmed (Fig. 57) that cesium ionization and blockade by the dense plasma of a high-current discharge were responsible for its small carrying-out from the source during a discharge pulse, whereas switching off the discharge resulted in a short-term cesium blowout through the emission slits [164]. Blowout amplitude and duration after switch-off increased with anode temperature.

The consumption of cesium passing through the emission slit of the pulsed planotronic source depended on anode temperature, which markedly affected stationary cesium outflow between the working pulses, as well as its pulsed blowout, the amplitude and duration of which depended on the cesium deposition rate onto the cooled parts of the anode after switching off the discharge [165]. The dependences of the stationary thermodesorption cesium flux from the source and the amount of cesium carried out in a pulse after switching off the discharge are demonstrated in Fig. 58. Cesium consumption in the planotronic source related to its outflow through the emission slits at the repetition rate < 10 Hz of pulses and anode temperature $< 300\,^{\circ}$C is a function of stationary flux Q_{dc} and does not exceed 0.5 mg cm^{-2} hr^{-1}.

Experiments on ion extraction through diagnostic windows in the cathode and anode with a subsequent analysis of ion fluxes in a magnetic mass spectrometer gave evidence that cesium is almost completely ionized during a discharge and transferred onto the cathode by the discharge electric field; thereby, a dynamically stable optimal cesium coating of pulsed SPS cathodes is maintained [165].

The rate of coating formation and the amount of the optimal cesium coating at the cathode in a pulsed high-current SPS were calculated in Ref. [142]. Under the high-current discharge conditions, the thickness θ of cesium coating of the cathode is described by the relationship between cesium capture and sputtering rates:

$$N_{Cs}\frac{d\theta}{dt} = (1-\theta)(\alpha_+ j_{Cs^+} + \alpha_0 j_{Cs_0}) - \theta\left(\gamma_{Cs-Cs}\, j_{Cs^+} + \sum \gamma_{Cs-H_i}\, j_{H_i}\right), \tag{5.1}$$

where N_{Cs} is the single-layer cesium coating on the surface, with the first term on the right-hand side of the equation characterizing cesium capture from ion (j_{Cs^+}) and atom (j_{Cs_0}) fluxes bombarding the surface, and the second term describing its sputtering by cesium and hydrogen ions. Coefficients α_+, α_0 characterize cesium capture per incident ion or atom, and coefficients γ_{Cs-Cs}, γ_{Cs-H_i} concern its sputtering by incident cesium and hydrogen ions. During a discharge pulse, $j_{Cs^+} \gg j_0$, and the solution of Eqn (5.1) assumes the standard form

$$\theta = \theta_{eq} - (\theta_{eq} - \theta_0)\exp\left(-\frac{t}{\tau_{eq}}\right), \tag{5.2}$$

where quantities θ_{eq} and τ_{eq} characterize the amount and time of formation of the equilibrium cesium coating at the cathode in a pulsed high-current SPS:

$$\theta_{eq} = \left[1 + \frac{\gamma_{Cs-Cs}}{\alpha_+} + \frac{\sum \gamma_{Cs-H_i}\, j_{H_i}}{\alpha_+ j_{Cs^+}}\right]^{-1}, \qquad \tau_{eq} = \frac{N_{Cs}}{(\alpha_+ + \gamma_{Cs-Cs})\, j_{Cs^+} + \sum \gamma_{Cs-H_i}\, j_{H_i}}. \tag{5.3}$$

Substituting coefficients α_+, α_0 and the measured values of j_{Cs^+} and j_{H_i} fluxes to the cathode shows that in high-current discharges in crossed fields (with planotronic, semiplanotronic, and Penning geometries of the electrodes), the equilibrium cesium coating of cathode optimal for negative ion generation is $\theta_{eq} \approx 0.50-0.55$ of the single-layer one and is achieved for $\tau_{eq} = 10^{-4}$ s [142].

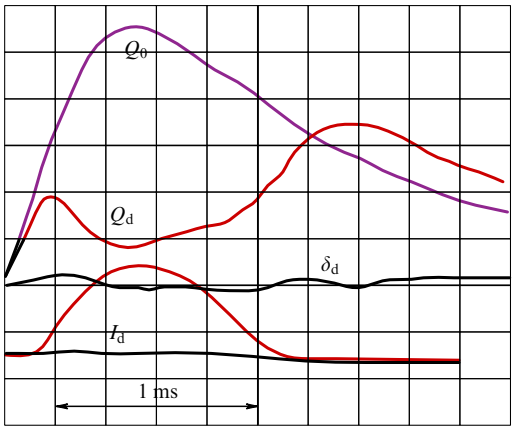

Figure 59. Oscillograms of the difference signal from a detector of hydrogen flux from the emission slit of a planotronic source in the absence of discharge (Q_0) and during and after passing the discharge pulse (Q_d): I_d — discharge current, and δ_d — signal of the detector at equal thermocathode emission currents characterizing noise compensation efficiency in the presence of high-current discharge.

The effects of rapid cesium ionization in pulsed high-current discharges of SPSs and cesium ion transfer to the cathode, as well as cesium dynamics in SPSs, were confirmed by spectroscopic measurements performed at BINP and the Sukhumi Physical–Technical Institute [166, 167].

Hydrogen fluxes from a pulsed SPS were measured with the aid of the BINP differential ionization detector with improved signal-to-noise ratio [168]. Oscillograms of the difference signal from the hydrogen flux detector of the planotronic source obtained during and after passing a discharge pulse are presented in Fig. 59. During the pulse, hydrogen is kept in the side gaps of the gas-discharge chamber by plasma pressure. As discharge current decreases, the 'plasma' valve opens and accumulated hydrogen escapes through the emission slits. Figure 59 shows that the hydrogen flux from the source and its respective density in the emission zone can decrease by a factor of 5–10 compared with the values before ignition of the discharge. Such a decrease in hydrogen density in the emission zone and beam formation region reduces the stripping of H^- ions as they pass through the plasma and are extracted from the source.

The above variants of SPSs with the planotronic geometry of electrodes make use of a discharge in crossed fields with closed electron drift. In this case, only a small part of the ions produced at the electrodes is formed into a negative ion beam, even with the employment of wide sectioned emission slits. The necessity to close the $\mathbf{E} \times \mathbf{B}$ drift of electrons complicates the construction and makes difficult the placement of feedthroughs (for hydrogen and cesium delivery) or electrode cooling tubes.

To increase the efficiency of plasma utilization in SPSs and create a construction more convenient for the placement of feedthroughs to the source and intense electrode cooling, it was proposed that a high-current discharge without $\mathbf{E} \times \mathbf{B}$ drift closure, in which the high-current plasma is generated on one side of the cathode in the immediate proximity to the emission slits to be used. Such a geometry taking advantage of only one side of the gas-discharge gap in the planotron was called a semiplanotron [169, 170].

The geometry of the first semiplanotron is shown schematically in Fig. 60. The high-current discharge is initiated at the 'triggering' end of the GDC (*1a* in Fig. 60) and spreads over the gas-discharge groove *1b* owing to electron drift in crossed electric and magnetic fields. The drift ceases at the oblique tail end *1c* of the gas-discharge gap and the plasma decays.

To facilitate ignition of the discharge in the absence of closed $\mathbf{E} \times \mathbf{B}$ electron drift, hydrogen and cesium were supplied into its triggering region, while the ignition dimple was made deeper than on the main part of the cathode for better electron confinement in the oscillation zone between its opposite cathode protrusions shaping the ignition dimple. The groove was semicylindrical in shape to concentrate negative ions propagating from the cathode to the emission slit (such a design was proposed for electrons by the British researcher W C Crookes away back in 1879). The 0.7-mm deep, 3-mm wide groove had a radius of curvature of 2 mm. The electric field created parallel to the magnetic field by virtue of the skewness of the tail part of the cathode *1c* caused an electron dump from the cathode groove onto the anode along the magnetic field lines. The conditions created at the part of the gas-discharge gap opposite the emission slit also prevented electron oscillations and the generation of parasitic discharges.

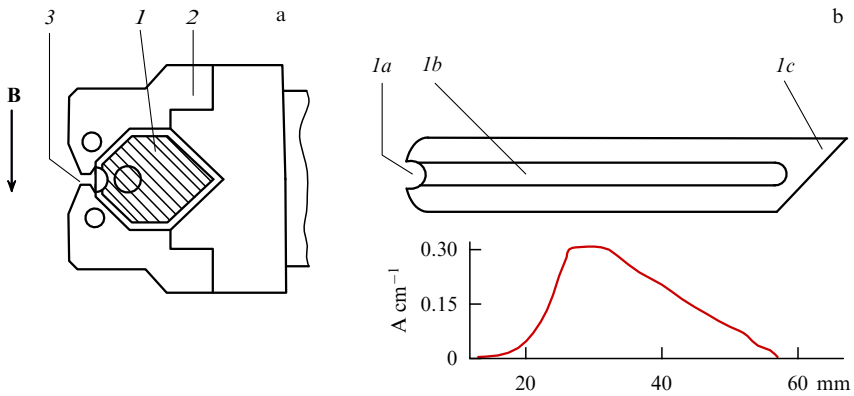

Figure 60. (a) Geometry of gas-discharge chamber of the first semiplanotronic source. Arrow shows the direction of source magnetic field **B**. (b) Emission slit view of cathode and distribution of negative ion beam current along the slit during ion extraction through the 1×40 mm^2 slit: *1* — cathode, *2* — anode, *3* — emission slit, *1a* — ignition dimple, *1b* — cathode groove, and *1c* — oblique tail end of cathode.

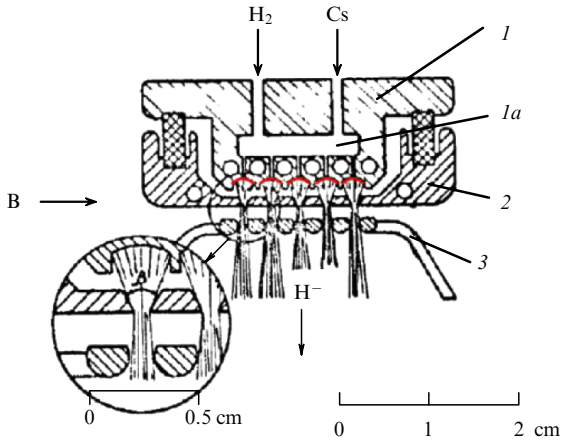

Figure 61. Geometry of the five-groove semiplanotron: *1* — cathode, *1a* — cathode distribution cavity, *2* — anode, and *3* — multislit extracting electrode. Arrow shows direction of magnetic field **B**.

Negative ions were extracted through emission slits of different lengths. Current density distribution of negative ions extracted through the 1×40-mm^2 emission slit is plotted in Fig. 60b. Negative ion current density reached a maximum value in the middle part of the emission slit opposite the middle part of the cathode groove. A negative ion beam with ≈ 0.9 A current comparable with the beam current obtained in a planotron with a 0.9×30-mm^2 emission slit and cathode of the same area but much higher discharge current (450 A) was obtained from the 0.72×45-mm^2 slit of the semiplanotron at a discharge current of 120 A and total cathode working area of 2.5 cm^2 [17]. This confirmed the working efficiency of the semiplanotron discharge in the absence of closed $\mathbf{E} \times \mathbf{B}$ electron drift and gave evidence of the effectiveness of ballistic focusing of negative ions formed at the cathode with a semicylindrical emission surface.

5.6 Pulsed surface-plasma sources with ballistic focusing

The next step in pulsed SPS research was to develop and investigate multiaperture semiplanotrons with ballistic focusing of negative ions produced at the cathode into slotted or round emission holes. Figure 61 is a schematic representation of the first multigroove semiplanotron making use of a discharge without closed $\mathbf{E} \times \mathbf{B}$ electron drift and ballistic focusing of negative ions into emission slits [170–172]. In this source, a high-current discharge was ignited in the absence of closed $\mathbf{E} \times \mathbf{B}$ electron drift between the 1.5×6-cm^2 multigroove cathode surface and the anode with five sawed emission slits 0.8×50 mm^2 in size each. To achieve a more uniform distribution of hydrogen and cesium along the gas-discharge gap, the cathode body had a cavity connected with the GDC by narrow channels of the slotted configuration through which hydrogen and cesium vapor were fed into the discharge.

The distributed delivery of hydrogen and cesium following cathode activation by the discharge (see below) made it possible to achieve an evenly burning high-current discharge over the entire surface of cathode grooves with a maximum yield of H^- ions and uniform current distribution along the emission slits. One-dimensional ballistic focusing enhanced the efficiency of utilization of the cathode working surface in the semiplanotron and reduced thermal loads on the gas-discharge electrode of the source. Negative ions drew together in emission slits from 40% of the cathode working area, and the H^- beam with a 2.6-A current was obtained at a relatively low discharge current (100 A) [172]. To compare, less than 15% of the cathode area could be utilized in a planotron with the flat cathode, while the negative ion yield at a 100-A discharge current was 0.8 A [144].

To reduce the density of hydrogen coming out from multiaperture SPSs to the beam formation zone and heighten the gas efficiency of sources, the semiplanotronic source was created with a two-dimensional ballistic focusing of negative ions onto the round emission slits. Such a source, in accordance with the arrangement of the spherically concave holes on the cathode surface was called the 'honeycomb' [173]. Figure 62 illustrates changes in the geometry of gas-discharge electrodes upon transition from a one-dimensional ballistic focusing to the two-dimensional one; it also compares multiaperture electrodes of the groove- and honeycomb-shaped SPSs with similar sizes of the cathode emission surfaces.

Each of the multislit and honeycomb sources having identical cathode emission surface areas (~ 10 cm^2) shown in Fig. 62 produced negative ion beams of roughly equal intensity with the virtually coincident discharge current dependences of the beam currents (Fig. 63) [173]. Generating negative ions was observed as more efficient at the 'cathode' section of the dependences in Fig. 63 at 5–50 A discharge currents, where the beam current increased linearly at a rate of 1.5 A for every 50 A of discharge current. In the range of discharge currents > 150 A, there was a linear 'anode' section of negative ion beam current growth at a rate of ≈ 1.5 A for every 300 A of discharge current.

A transition of the cathode section of the current dependence to the anode one observed in the 60–150-A discharge current range was due to increased plasma density in the gas-discharge gap and enhanced stripping of

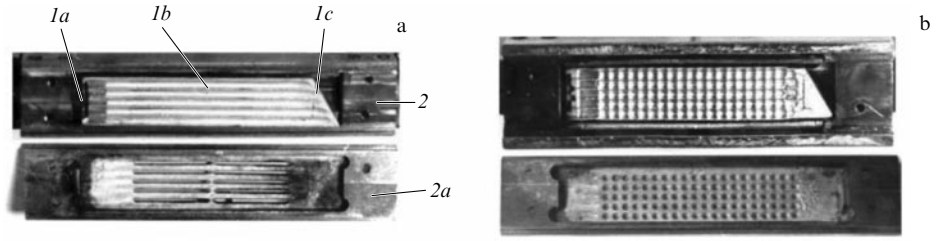

Figure 62. Photographs of gas-discharge electrodes of semiplanotrons with cylindrical (a) and spherical (b) geometrical focusing: *1a* — cathode ignition dimple, *1b* — grooves or rows of spherically concave depressions at the cathode, *1c* — cathode skewed tail, *2* — anode frame, and *2a* — anode cover with emission holes.

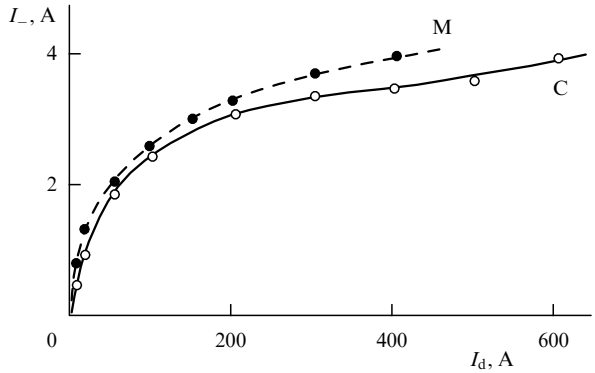

Figure 63. Dependence of the negative ion beam current I_- on discharge current I_d for five-slit semiplanotron M and honeycomb source C with the same cathode area.

negative ions formed at the cathode during their passage through the plasma sheet. The enhanced stripping of fast cathode negative ions accelerated by the near-cathode drop in discharge voltage was associated with the observed proportional enhancement of the flux of fast atoms bombarding the anode and the walls of emission slits, which led, in turn, to an increase in the anode group in the negative ion beam.

In the cathode section of the dependences (see Fig. 63), the mean power of the thermal load on the cathode at a 50-A discharge current did not exceed 0.5 kW cm^{-2}, while the energy 'price' of negative ion generation in the discharge was below 4 keV per ion.

In the honeycomb source, it proved possible, due to the four-fold decrease in the emission hole area (in comparison with that in the multislit semiplanotron), to reach a more uniform distribution of current emission density over the cathode surface and obtain H^- ion beams with high gas efficiency. For example, in the case of extraction of a beam with a 2.5–3-A current through 100 emission holes with a total area of 0.5 cm^2, the measured integral hydrogen flux from the source during a discharge pulse was 3×10^{19} molecules per second ($\approx$ 10 A equiv. in terms of atoms); in other words, the gas efficiency expressed in terms of the number of atoms reached 25–30 %.

The high emission density of the negative ion beams thus obtained, reduced power released at the electrodes, low consumption of working substances (hydrogen and cesium), and shielding of the main working surface of the cathode from external fast particle fluxes, as well as the possibility of a many-fold increase in beam current due to a greater number of cells, taken together stimulated further investigations and modernization of honeycomb SPSs.

Modeling and experimental studies of the efficiency of ballistic focusing in honeycomb SPSs were undertaken. A three-dimensional MODA code using the main principles of the MARLOWE code was developed at BINP [174, 175] for the quantitative assessment of factors influencing ballistic focusing. The formation of negative ions by proton sputtering and reflection from hydrogen-saturated targets was simulated, the sputtering and reflection coefficients calculated together with energy spectra of sputtered and reflected particles. The effect of the near-cathode discharge voltage drop, the shape and thickness of this layer, the composition of ion current onto the cathode, and the geometry of gas-discharge electrodes on the effectiveness of negative ion

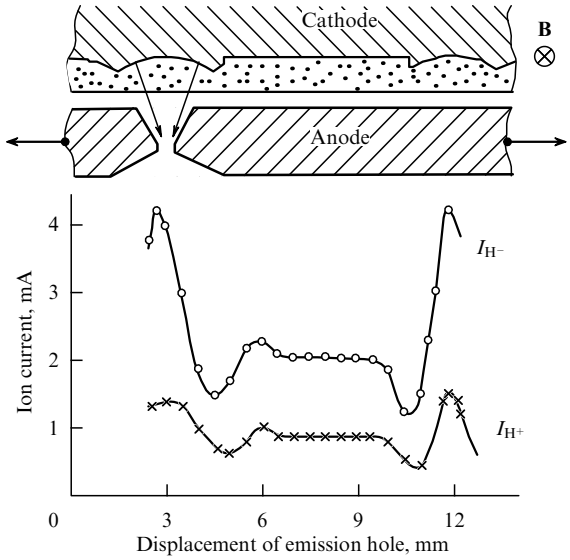

Figure 64. Beam current distribution of negative (I_{H^-}) and positive (I_{H^+}) ions extracted from a honeycomb source at different positions of the emission hole with respect to spherically concave and flat cathode areas. Extracting positive ions reversed the polarity of voltage applied to the GDC.

accumulation in SPS emission holes have been established [174, 175].

Experiments carried out to check the efficiency of geometric focusing in SPSs included the extraction of negative ions from the honeycomb source, in which part of spherical cathode concavities was substituted by plane surface areas, as demonstrated schematically in the upper part of Fig. 64 [176]. It was established that a negative ion beam extracted from the emission hole located opposite a spherically concave depression at the cathode is 2–3 times bigger than that extracted from the hole opposite the plain site (I_{H^-} dependence in Fig. 64). The current of positive ions extracted in the case of altered polarity of voltage applied to a GDC was also higher in the case of ion extraction from the hole located opposite a spherically concave depression on the cathode surface (I_{H^+} dependence in Fig. 64).

Measurements of the energy spectrum of negative ions extracted from such a source were made at different positions of the emission hole relative to the center of spherically concave depressions. A change in the total current I_{H^-} of an ion beam extracted from one of the emission holes of the honeycomb source and the current of the cathode (C) and anode (A) groups registered by an electrostatic energy analyzer in the case of displacement of the emission hole with respect to the spherically concave depression over the cathode surface is shown in Fig. 65 [177]. If the emission hole is positioned opposite the focal point, roughly 80% of the extracted negative ions had a mean energy of 175 eV (at a discharge voltage of 150 V), which suggests that the ions were formed on the cathode surface. The energy of 20% of the ions in the extracted beam corresponded to the anode potential. If the emission hole was displaced to the 'minimum' point corresponding to a 1.5-mm shift in Fig. 65, the intensity of the cathode group of negative ions (C in Fig. 65) decreased by a factor of 10, while the mean energy of the ions of this group increased to 240 eV because of the wider angular spread of negative ions formed by the reflection of fast particles.

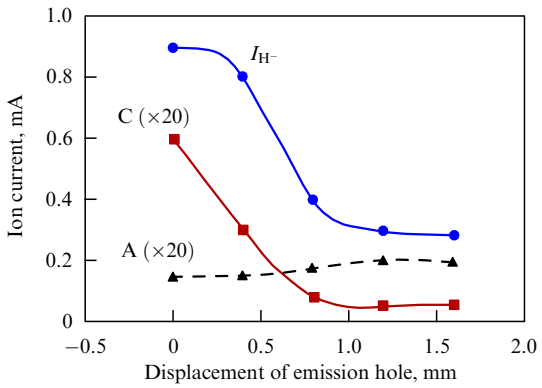

Figure 65. Variation of the negative ion beam current I_{H^-} and current of cathode (C) and anode (A) groups of the beam recorded by an electrostatic energy analyzer upon displacement of the emission hole relative to the center of the spherically concave depression on the cathode surface [177].

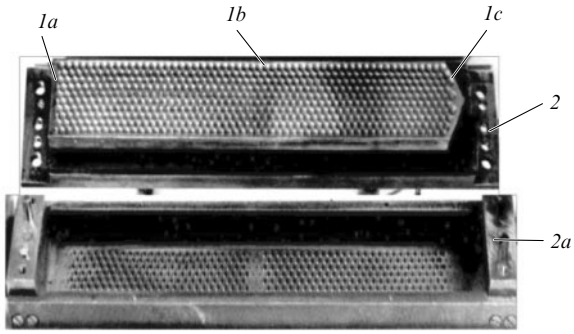

Figure 66. Photographs of gas-discharge electrodes of a pulsed honeycomb source with 600 unit cells for beam extraction. *1a* — ignition dimple at the cathode, *1b* — cathode surface with 600 spherically concave depressions arranged hexagonally, *1c* — electron dump region, *2* — anode frame, and *2a* — anode cover with 600 emission holes.

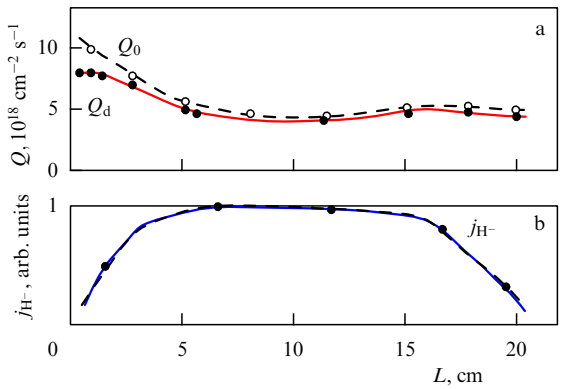

Figure 67. (a) Flux density distribution of hydrogen outgoing from different parts of an MHS (in terms of the atoms): Q_0 — before discharge ignition, and Q_d — during the discharge pulse. (b) Distribution of beam current density j_{H^-} in emission holes along the MHS length.

Conversely, the anode group (A in Fig. 65) grew 1.5 times upon such displacement, and its intensity was thrice that of the cathode group [177].

The experimentally found efficiency of ballistic focusing (the ratio of the beam current from a honeycomb source to that from an analogous source with a flat cathode) was 3–3.5 for the total negative ion beam, 10–12 for a group of negative ions 'sputtered' from the cathode, 1.5–2 for a group of negative ions 'reflected' from the cathode, and 0.8–0.9 for the anode group of negative ions [176]. Geometrical focusing was most efficient for the group of negative ions sputtered from the cathode due to a smaller energy and angular spread of the particles formed by sputtering from the cathode surface [174].

A pulsed multiaperture honeycomb source (MHS) with an enlarged electrode area and 600 negative ion beam extraction and formation unit cells was developed in 1983 [178, 179]. The basic setup of an MHS is analogous to that of the earlier multiaperture semiplanotron sources (see Fig. 61). The high-current glow discharge of an MHS is localized in a lengthy (3×20 cm^2) gap between the cathode surface and the anode cover with emission holes. The discharge space is bounded from the edges by the ignition dimple, side cathode protrusions, and electron dump region, as shown in Fig. 66.

An outer electromagnet created in the discharge space a 0.05–0.15-T magnetic field parallel to the plane of the gas-discharge gap. The height of the side cathode protrusions determining the thickness of the electron oscillation region in the discharge at the main part of the cathode was 1–2 mm. To facilitate triggering a discharge in the ignition dimple, the height of the cathode side protrusions was increased to 4–5 mm, and the effective cathode emission surface area to 54 cm^2. Hydrogen was fed into the gas-discharge gap from several pulsed electromagnetic valves through the cathode distribution cavity; a plate with a varied pitch of the bypass holes was placed inside the cavity to shape the necessary hydrogen density profile along the gas-discharge gap.

Spherically concave depressions with a 3.5-mm radius of curvature of the surface were hexagonally arranged over the cathode surface, with their diameters overlapping to more efficiently utilize the available area. Conical emission holes 0.9 mm in diameter were drilled at beam focusing sites taking into account trickle flow displacements in the magnetic field. The total area of the emission holes was 3.8 cm^2. Negative ions were extracted using a louvered electrode system. To enhance the electric strength of the 1.3-mm extracting gap with an area of 3.3×20 cm^2, the louvers were made of profiled molybdenum and heated by in-built ohmic heaters [178].

Discharge current in the MHS varied in a range up to 700 A, and working discharge voltage from 150 to 200 V. The main factors determining the efficiency of negative ion generation were the thickness and homogeneity of the cesium coating at the cathode, hydrogen distribution over the lengthy gas-discharge gap, and uniformity of the discharge (especially ionic) current distribution over cathode emission surface. Optimization of above factors resulted in producing the H^- ion beam with a current above 11 A, pulse duration up to 0.8 ms, and a pulse repetition rate of 1 Hz; this beam was accelerated up to the energy of 25 keV. Total detected current of negative ions amounted to 12 A (taking into account the current of heavier impurity negative ions). The mean negative ion current density in the emission holes of the MHS was ≈ 3 A cm^{-2}, and mean negative ion density in the beam was 180 mA cm^{-2}.

Beam current density distribution j_{H^-} in the emission holes along the MHS length is illustrated in Fig. 67b. A sharp drop in emission at the edges of the emission zone was due to reduced plasma density in the initial and dump regions of a discharge, resulting from nonuniform cathode 'self-activa-

tion' by the discharge. Figure 67a shows the density distribution of the hydrogen flux outgoing from the MHS (in terms of the atoms) prior to discharge ignition (Q_0) and during discharge pulse (Q_d); it was measured by noise-immune detectors. At a beam current of 11 A, the hydrogen flux from emission holes (in terms of the atoms) was $Q_d \sim 3 \times 10^{20}$ atoms per second; accordingly, the pulsed gas efficiency reached $\eta = I_{H^-}/Q_d \geqslant 20\%$. Cesium blocking by discharge plasma accounted for its insignificant carrying-out during a discharge pulse, while consumption of cesium produced in the MHS was determined by the thermodesorption flux during interpulse intervals and did not exceed 10 mg hr^{-1}.

5.7 Stationary surface-plasma sources for accelerators

The first stationary surface-plasma source of negative ions with continuous discharge and beam extraction was designed and studied at BINP in 1990 [180]. The plasma in this source was created by a discharge from a GDC having a semiplanotron geometry. To facilitate triggering of the discharge, the rear side of the cathode had an ignition dimple parallel to the magnetic field, which was fed with hydrogen and cesium vapor. Negative ions were generated at the spherically concave cathode surface and focused into a conical emission hole with a 1-mm passage diameter. Negative ions were drawn out by a 20-kV voltage using a conical extracting electrode. H^- ion beams with a 2.5-mA current were obtained from a 100-V hydrogen–cesium discharge with a 0.8-A current. At a discharge power below 100 W, the source did not need cooling. A few one-day cycles of operational testing of the source were carried out, confirming the good prospects for practical applications of such an SPS.

Stationary operational testing of a negative ion SPS with the Penning geometry of electrodes and plasma injection into a GDC through cathode cavities and holes was undertaken in 1992–1994 [181, 182]. In this modified ion source with an enlarged plasma volume, the multiaperture extraction of negative ions through several conical holes in the anode cover was used. A stationary H^- ion beam with a 19-mA current was obtained at a discharge power of 300 W (5 A, 60 V) [181]. An analogous source with a plasma volume of $16 \times 36 \times 9$ mm^3 and stationary ion extraction through 18 emission holes 2.6 mm in diameter each served to generate an H^- ion beam with a 50-mA current and discharge power of 560 W (7 A, 80 V) [182].

The year 1998 witnessed the beginning of development of stationary surface-plasma sources of negative ions with plasma injection from heated hollow cathodes. At first, procedures for the stationary generation and extraction of negative ions were tested using a semiplanotronic source with four large spherically concave depressions and a heated hollow cathode installed in the ignition dimple of the cathode of the semiplanotron discharge shown in Fig. 68. The cathode was heated adapting an ohmic heater, while hydrogen and cesium were fed into the cathode cavity and through narrow slits into the semiplanotronic discharge zone. Stationary high-current discharge was triggered and maintained by plasma injection from the hollow cathode into the ignition dimple. Extraction of the ion beam from a stationary discharge with a current of 12 A through four 2×10-mm^2 emission slits produced 4 separate H^- ion beams each with a current higher than 10 mA [183].

In 2002, an SPS with heated hollow cathodes and the Penning geometry of the GDC was constructed and tested. Its

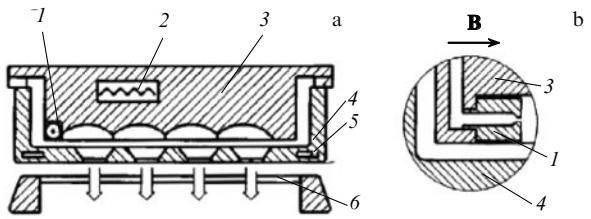

Figure 68. Semiplanotronic source with a hollow cathode and four spherically concave depressions for geometrical focusing of negative ions. (a) Section across the magnetic field. (b) Geometry of ignition dimple and hollow cathode (section along the magnetic field) [183]. Arrow shows direction of a magnetic field: *1* — hollow cathode, *2* — cathode heater, *3* — cathode with four spherically concave depressions, *4* — anode, *5* — cooling canals, and *6* — extracting slit electrode.

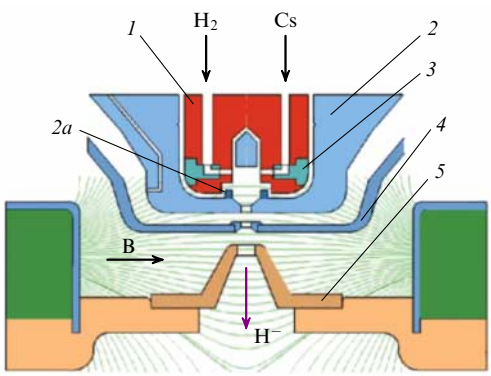

Figure 69. Layout of a stationary negative ion source with the Penning geometry of discharge and hollow cathodes. Section along magnetic field (direction indicated by arrow): *1* — cathode, *2* — anode, *2a* — anode collar, *3* — hollow cathode insert, *4* — extracting electrode, and *5* — accelerating electrode.

diagrammatic layout is presented in Fig. 69. The hollow cathodes used to inject plasma into the Penning discharge were shaped as small cylindrical inserts into massive cathode protrusions. Feeding hydrogen and cesium through cathode cavities with small outlet holes 1.2 mm in diameter provided a working substance density gradient between the inside of the hollow cathode and the Penning discharge region. Cesium was fed from an external compact cesium oven containing cesium chromate–titanium pellets. Plasma emission from cathode cavities maintained the stationary Penning discharge with currents up to 10 A and a voltage of 70–120 V at a reduced hydrogen pressure (30 mTorr) in the GDC.

Negative ions formed as a result of fast atom conversion on the anode surface, the optimum anode temperature for H^- beam generation being 250–300°C. The negative ion beam was extracted and accelerated by a three-electrode IOS. An ≈ 0.1-T magnetic field was generated by an external magnet that created force lines of a dome-shaped configuration needed to enhance the high-voltage strength of the IOS.

An experimental model of such a source made possible the generation of a stationary H^- ion beam with up to a 5-mA current [184]. A replica of this device with a negative ion beam current of up to 8 mA [185] developed in 2004 was installed in the BINP tandem accelerator in 2006. The design and parameters of the Penning SPS with hollow cathodes installed in the BINP tandem are described in detail in Ref. [186]. This source was used to generate and accelerate up to 2 MeV a proton beam with a 5.7-mA current [187]. A

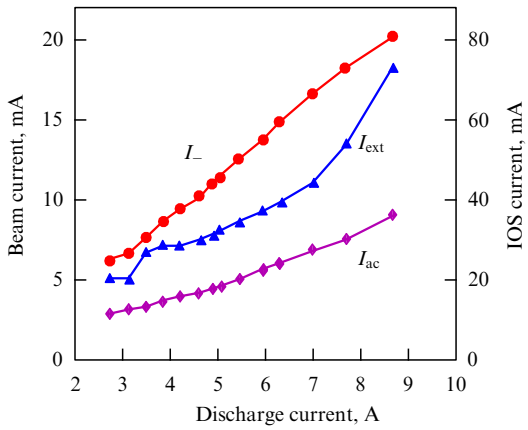

Figure 70. Beam current I_- and IOS electrode currents I_{ext} and I_{ac} versus discharge current.

few modifications to this device prolonged its service life and simplified maintenance operations for more than a decade of its exploitation. The total operation time of the source is now almost 2900 hours with an average running time of about 5 hours per day. The entire operation statistics of the source with the BINP tandem is described in report [188].

To obtain stationary H^- ion beams with enhanced current and ion energies under conditions of long-term continuous work at accelerators, modified versions of the hollow-cathode Penning source were designed and deployed [189, 190]. Their discharge electrodes and IOS electrodes were made more massive, and water-cooling circuits were installed at the periphery of the flanges, supporting the electrodes to improve thermal regulation. Diameters of the emission hole and apertures in IOS electrodes were increased to 3.5 mm. Both sources [189, 190] produced stationary up to 15-mA H^- ion beams with a discharge current of 6–7 A, discharge voltage of 75–85 V, hydrogen feeding rate of 0.15 l Torr s^{-1}, and a magnetic field of $\approx$ 0.1 T.

The dependences of the source emission currents (beam current and currents in the IOS electrode circuits) on the Penning discharge current for the source [190] are presented in Fig. 70. The H^- ion current increased with discharge current and amounted to 15 mA, when the latter was 6–7 A. At an ion beam current of 15 mA, the total current in the extraction circuit was around 40 mA, and in the accelerating electrode circuit it was 25 mA.

Computer-assisted management (automatic control system) allowed maintaining long-term operation of the source following a scenario of beam current stabilization within a predetermined range. A few lengthy test cycles were carried out to evaluate the operational efficiency of the source under continuous (over 100 h) work conditions. An example of the stable beam current supported by the automated management system during continuous testing is presented in Fig. 71.

Further improvement in the hollow-cathode Penning SPS was intended to increase the diameters of the anode emission hole and IOS apertures to 5 mm with modification of the magnetic system [191]. To reduce the electron flux extracted from the plasma together with negative ions through the hole with the enlarged aperture, a collar was placed around the emission hole in the near-anode region (see Fig. 69). The reduction in the accompanying electron flux allowed sputtering of the anode cover and erosion of the IOS extracting electrode to be diminished.

The perfected source ensures long-term operation with the generation of a stationary H^- ion beam having a 25-mA current and emission current density higher than 0.125 A cm^{-2} at a discharge current of $\sim$ 10 A [191]. Further growth in the discharge current did not lead to the beam current saturation, which suggests the possibility of increasing the H^- ion beam current by amplifying the discharge current and enhancing the source electrode cooling. An external view of the 25-mA Penning SPS with hollow cathodes installed at the experimental test bench is shown in Fig. 72.

Beam current ripples and discharge noises of the stationary hollow-cathode Penning source were studied in Ref. [192]. The frequency spectrum of beam and discharge current fluctuations was found to contain several peaks, including the main 0.3–0.4 MHz fluctuation peak. Spectral analysis revealed that beam current fluctuations were due to variations in local plasma density in the discharge, which were related to variations in cathode emissivity and discharge current density redistribution among different cathode regions. This observation was confirmed by the high

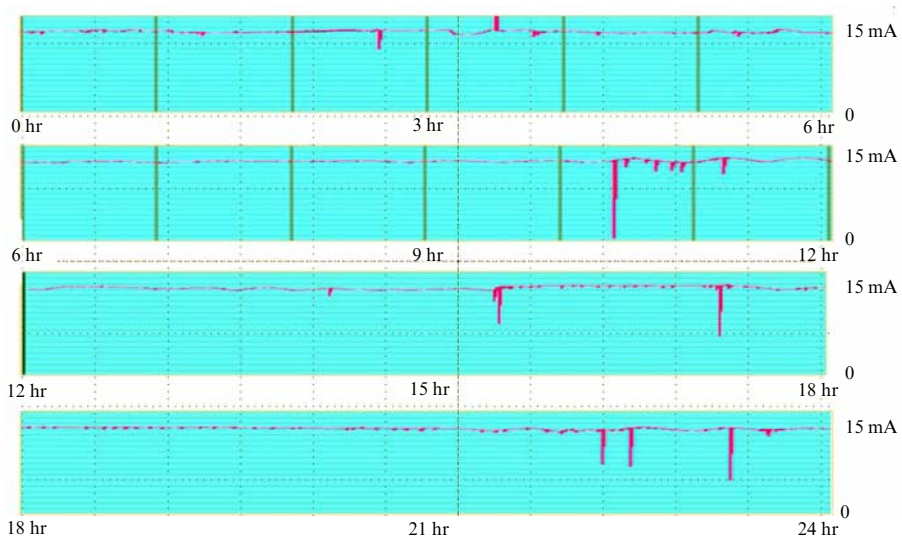

Figure 71. Stable H^- beam current maintained at the 15-mA level during a 24-h test by an automated control system [190].

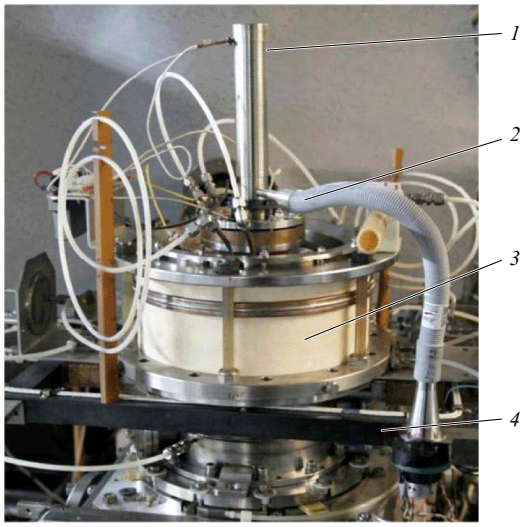

Figure 72. Twenty-five-milliampere SPS with hollow cathodes on the experimental test bench: *1* — heated vessel with cesium-containing pellets, *2* — air cooling to control the cold point temperature of the cesium system and regulate cesium input, *3* — ceramic insulator between flanges of IOS extracting and accelerating electrodes, and *4* — magnetic system with an external magnetic circuit [191].

sensitivity of discharge and beam fluctuations to the cathode cesium coating and their weak dependence on the magnetic field and hydrogen feeding. It was shown that electrode training and conditioning by discharge lower the discharge and beam noises.

References [193, 194] describe conditions and possibilities for the application of stationary sources with the cathode generation of negative ions. A high-current stationary SPS of H^- ions having the semiplanotron and planotron geometries of electrodes were created and tested. Measurements demonstrated that stationary semiplanotron and planotron sources need the discharge with a higher ($\sim$ 100 V) voltage. Negative ions formed at the cathode account for about 30% of the overall composition of the beam extracted from the semiplanotron source, whereas their content in the planotron source does not exceed about 20% of the beam current. The semiplanotron source ensured the highest efficiency of H^- generation at discharge currents of up to 5 A; higher currents overheated the cathode and thereby reduced beam current.

5.8 Quasistationary ion sources with radio-frequency discharge for controlled fusion injectors

In 2009, a detailed plan for the construction of a high-voltage neutral beam injector with a beam energy of 0.5–1 MeV [195] for the Field Reversed Configuration (FRC) device to be used in CF research was developed at BINP. The injector includes a source of negative ions, beam transport and separation section, accelerator and neutralizer (Fig. 73).

The design envisages acceleration of a negative ion beam from an RF ion source up to 120 kV and its transport through the section with deflecting magnets at an applied potential of −880 kV relative to the ground. As the beam passes through this section, it goes off the source axis and focuses into the entrance to the single-aperture accelerator, which further accelerates it to 0.5–1 MeV. The negative ion beam thus accelerated is converted into a beam of high-energy neutral particles that is separated from the accompanying beams of positive and negative ions in the separator chamber wherefrom it is carried out and sent to the target, whereas the accompanying beams of positive and negative ions come after separation into energy recuperators. Work on the final adjustment of all the above operations for the generation, acceleration, and neutralization of negative ion beams is currently underway at BINP in the framework of a project for the creation of a high-energy atom injector.

An experimental bench constructed in 2014 allows developing and testing the stationary high-current SPSs of negative ions (Fig. 74). It consists of a 3.1-m long vacuum tank 2.1 m in diameter equipped with two cryogenic pumps and two deflecting magnets for a parallel shift of the negative ion beam off the source axis towards the accelerator axis before entering the acceleration tube. Beam diagnostics is performed with the aid of a movable Faraday cup-based

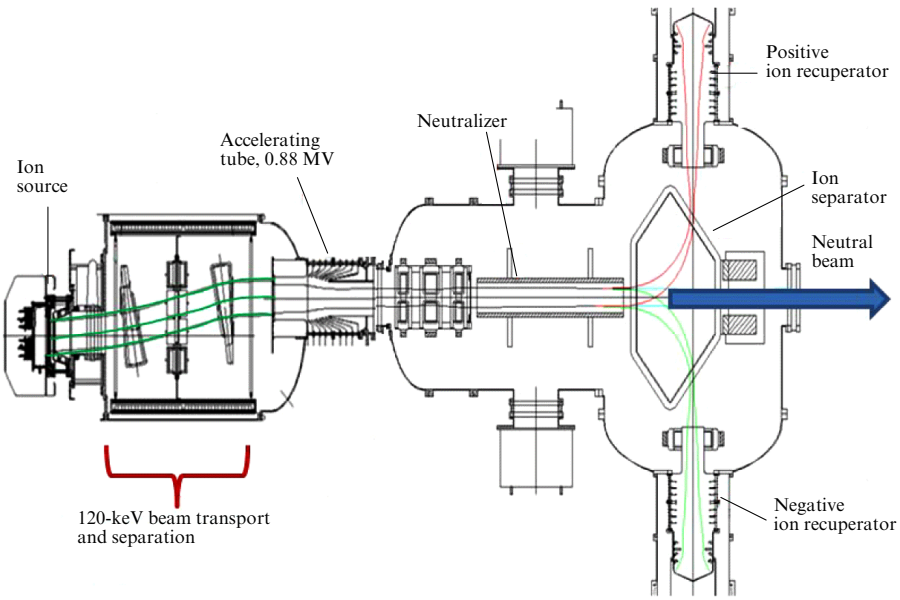

Figure 73. Schematic of the BINP high-voltage injector with negative ion acceleration.

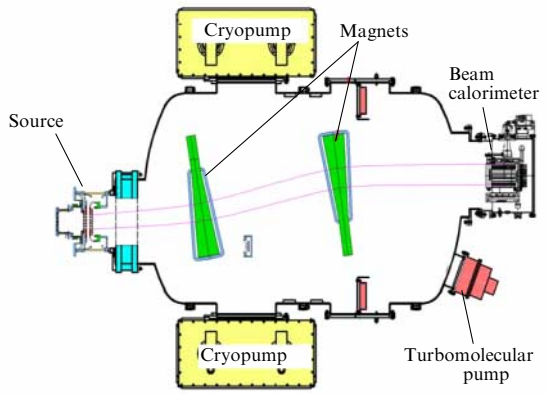

Figure 74. Schematic of an experimental test bench for the generation and transportation of intense negative ion beams.

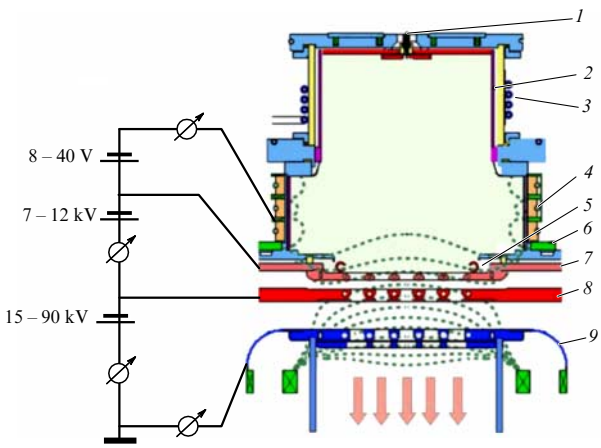

Figure 75. Conceptual diagram of a source and electrical measurement scheme: *1* — spark ignition, *2* — Faraday shield, *3* — RF driver antenna, *4* — magnetic wall of expansion chamber, *5* — cesium distribution tube, *6* — dipole magnetic filter, *7* — plasma electrode, *8* — extracting electrode, and *9* — accelerating electrode. Dotted curves mark magnetic field lines.

collector inside the tank and beam calorimeter mounted on the output flange. A vacuum section with deflecting magnets responsible for the displacement of the source and accelerator axes is needed to clean the ion beam before its injection into the accelerator from the primary particles leaving the source and from secondary particles produced in the course of a beam formation. The displacement of above-mentioned axes protects the ion source from back-streaming positive ions from the accelerator. Intense tank evacuation by two cryopumps reduces negative ion stripping and promotes the formation and multiplication of secondary particles in the beam transport region and the accelerator.

A surface-plasma source of negative ions with an RF plasma generator is being developed for the BINP injector to extract negative ions from the large-area emitter [196]. A conceptual diagram of the source is presented in Fig. 75. Its main elements include the RF driver, an expansion chamber, a plasma electrode functioning as a negative ion emitter, ion-optical, magnetic, and cesium feeding systems, and an electrode thermal stabilization system (not shown in Fig. 75).

The plasma is created in the driver's cylindrical chamber by an inductive RF discharge in hydrogen, which is fed with the aid of a valve through the spark ignition unit. The RF discharge was initiated by the spark ignition over the insulator surface. The inductive 4-MHz discharge was produced by an external 3.5-winding antenna. The rear flange of the driver chamber supports permanent magnets intended to enhance discharge efficiency and reduce plasma diffusion from the discharge region to the flange butt-end. A molybdenum Faraday shield with slits is installed inside the ceramic driver to protect it from erosion by the plasma. The RF driver operates under 0.3–0.5-Pa hydrogen pressure inside the chamber to maintain the discharge at a power of up to 36 kW deposited onto the plasma.

The plasma generated in the driver spreads into the expansion chamber with a peripheral multipole magnetic field induced by permanent magnets, and its particles bombard the plasma electrode that makes up the lower boundary of the expansion chamber. The plasma electrode is actually an emitter of negative ions generated by the conversion of fast plasma particles on its surface. To enhance the generation of negative ions, the plasma electrode surface is exposed to cesium vapors introduced into the source through a distribution–accumulation tube (*5* in Fig. 75) while heating the outside vessel with cesium-containing pellets.

Negative ions produced at the emitter are extracted and merged into a beam by a three-electrode multiaperture ion-optical system. To enhance the electric strength of the high-voltage IOS gaps, thermal stabilization of electrodes is applied, whereby IOS electrodes are first heated and thereafter cooled with a hot coolant during a working pulse. Following recommendations based on experience with pulsed planotron SPSs (see Section 5.3) and stationary hollow-cathode SPSs (see Section 5.7), the magnetic field lines in the IOS region are bent toward the plasma and extracting electrodes to prevent electron accumulation [197]. Magnetic field lines in the central plane of the source are shown in Fig. 75 by dotted curves. Most accompanying electrons extracted together with negative ions are deflected by the transverse magnetic field generated in the IOS to be absorbed on the walls of the extracting electrode.

Photographs of multiaperture electrodes of the ion-optical system of the source are presented in Fig. 76. Twenty-five conical holes with a drift diameter of 16 mm each are drilled in the plasma electrode (Fig. 76a) to extract newly formed negative ions. The extracting electrode (Fig. 76b) has conical holes 14 mm in diameter to enable the passage of the extractable beam. The 108-mm long and 16-mm wide slits in the accelerating electrode (Fig. 76c) are aligned along their length co-axially with the conical holes of two other electrodes, and normally to the IOS magnetic field lines.

Heating and cooling electrodes with a hot cooler are necessary to maintain operation of the source in the hydrogen–cesium regime with cesium feeding. The plasma electrode is heated to optimize its cesium coating and stimulate negative ion generation, whereas the elevated temperature (100–250°C) of the extracting elec-

Figure 76. IOS electrodes: (a) plasma, (b) extracting, and (c) accelerating.

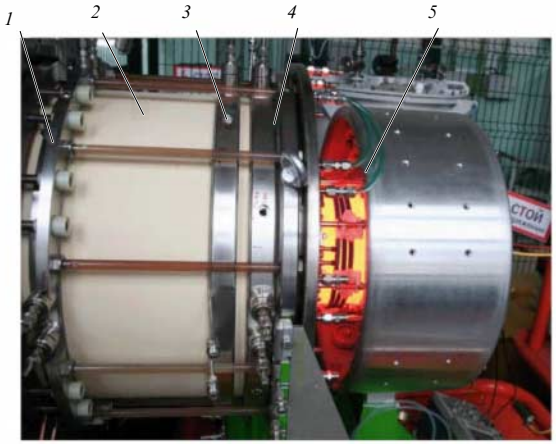

Figure 77. External view of a RF source during discharge pulse: *1* — accelerating electrode flange, *2* — ceramic insulator, *3* — extracting electrode flange, *4* — plasma electrode flange, and *5* — RF driver.

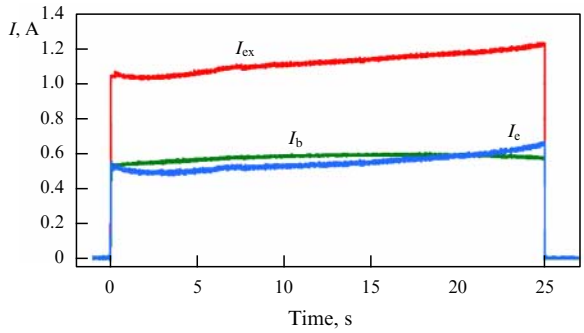

Figure 78. Oscillograms of emission currents of the source in long pulses: I_{ex} — current in extracting voltage rectifier circuit, I_b — IOS output beam current, and I_e — current of accompanying electrons. RF driver with Faraday shield: RF discharge power $P_{RF} = 17$ kW, extracting voltage $U_{ex} = 7$ kV, accelerating voltage $U_{ac} = 75$ kV, and hydrogen pressure in discharge chamber 0.35 Pa.

trode improves the high-voltage strength of the IOS. Heating prevents cesium accumulation at the edges of the IOS electrodes and its uncontrolled desorption under the effect of bombardment by accelerated negative ions, accompanying electrons, and back-streaming positive ions. Preliminary heating of the plasma and extracting electrodes to 150–250°C and their cooling with a hot coolant during pulse passing are secured by pumping the high-temperature coolant through channels drilled in the IOS electrodes using a commercial thermal stabilization system (Lauda).

IOS electrode heating and cooling by pumping a hot coolant, the use of an IOS transverse magnetic field with bent lines of force, and cesium feeding directly onto the emitter surface through the distribution/accumulation tube are conceptually new elements introduced in the construction of an RF source designed at BINP. Studies performed on the BINP experimental bench demonstrated the working efficiency of these innovations [198, 199]. They stabilized the work of the source in the hydrogen–cesium regime with low cesium consumption and required a high-voltage strength of IOS gaps. Stable 1.2-A H^- ion beams at the exit from the IOS had an energy of 90 keV in 2-s pulses with the RF discharge power of 34 kW and initial hydrogen pressure of 0.4 Pa. Emission current density of the beam during extraction was 28 mA cm^{-2}. The current of accompanying electrons did not exceed 1 A. The size of the H^- ion beam transported to a distance of 1.6 m was 30×25 cm^2. Figure 77 displays an external view of the RF source with the switched-on RF discharge.

To protect the ceramic driver of the source operating in the long-pulse (up to 25 s) regime from overheating and erosion by fast plasma particles, a metallic Faraday shield with slits was installed inside the driver, which decreased the power deposited in the plasma. It was revealed that the involvement of the Faraday shield increased the positive plasma potential by augmenting electron diffusion to the metallic Faraday shield [199]. The increased plasma potential of the RF discharge enhanced optimal bias voltage U_{PG} at the plasma electrode needed to suppress the accompanying electron flow.

Typical emission current oscillograms illustrating the work of the source with the Faraday shield in 25 s pulses are presented in Fig. 78. Clearly, the current I_b of the H^- ion beam being formed remained stable during a pulse. The total current I_{ex} in the extraction circuit characterizing the sum of currents of the ion beam and accompanying electrons was two times higher than the negative ion beam current. Difference current $I_e = I_{ex} - I_b$ corresponding to the current of accompanying electrons remained unaltered during most of a 25 s pulse but experienced an approximately 20% rise by the end.

Stability of the current of the newly formed negative ion beam suggests stability of plasma parameters in the region adjacent to the plasma electrode and cesium coating of the negative ion emitter during a 25 s pulse, while the current amplification of accompanying electrons at the end of the pulse appears to be due to a rise in plasma potential in the expansion chamber as a result of depletion of its cesium coating [196].

In a source operating without a Faraday shield, the maximum power deposited in the plasma increased to 36 kW at a 20% lower hydrogen feeding, while the required optimum voltage U_{PG} applied to the plasma electrode decreased twice. The maximum current of the negative ion beam at the exit from the source in the absence of a Faraday shield was proportional to the power introduced into the discharge ($I_b = 1.2$ A).

It was established that the distributed delivery of cesium to the preliminarily heated plasma electrode through the holes of the distribution/accumulation tube maintains the high negative ion emission rate, which may persist for a long time without additional administration of cesium into the tube. Long-term preservation of the cesium coating at the plasma electrode necessary for ion generation is provided by cesium release from the discharge-heated distribution/accumulation tube and by its recondition from compounds synthesized in chemical reactions in the plasma. Specifically, a single outflow of 0.5 g of cesium maintained the work of the source for 32 days and the production of a beam comprising 2500 long pulses [200].

Heating IOS electrodes by a hot coolant considerably simplified their training and increased the electric strength of IOS high-voltage gaps [197]. Figure 79 illustrates this procedure as exemplified by a source extracting gap training during ion beam extraction. Preliminary high-voltage electrode training in a vacuum facilitated the maintenance of high voltage (12 kV). At the beginning of beam extraction

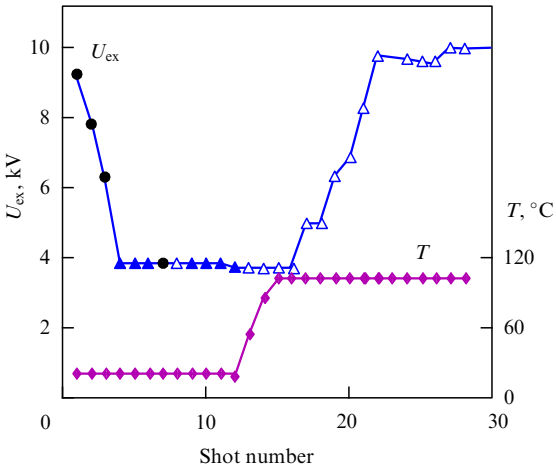

Figure 79. Speedup of IOS extracting gap conditioning by heating plasma and extracting electrodes: U_{ex} — extracting gap voltage, light triangles — pulses without breakdowns, dark triangles — pulses with breakdowns and voltage recovery, dots — pulses with breakdowns without voltage recovery, and T — electrode temperature.

(pulses 1–12, Fig. 79), breakdowns occurred in 11 shots out of 12, despite a marked consecutive decrease in applied voltage. Heating extracting and plasma electrodes significantly intensified the training of the extracting gap and made it possible to reach a nominal extracting voltage of 10 kV during 10 subsequent 2-s training pulses. Analogous dependences characterizing a speedup of the electrode training procedure and an increase in the electric strength of IOS high-voltage gaps, namely the accelerating gap, were obtained in the case of training by high-voltage pulses in a vacuum and electrode training with ion beam acceleration [197].

A rise in the electric strength of IOS high-voltage gaps in the source using cesium is due to its enhanced redistribution rate associated with electrode heating. The amount of cesium adsorbed at IOS electrode edges exposed to beam particles depends on the relationship between cesium deposition rate at the IOS electrodes and the rate of its transport towards the periphery of the IOS electrodes. Most cesium is accumulated at IOS electrodes in the pauses between pulses, depending on its amount and distribution in the plasma chamber, the duration of interpulse intervals, electrode temperature, and shielding gas pressure in the source. Electrode heating exponentially enhances surface diffusion and thermal desorption; it also prevents cesium accumulation at the edges of IOS electrodes in the case of its weak inflow from the plasma chamber. Such a situation is realized in the BINP RF source under consideration, in which intense generation of negative ions occurs with small cesium consumption [200]. Cesium escapes faster from the edges of heated IOS electrodes due to its sputtering by accelerated beam particles and positive ion counterflows.

Investigations into the transport of negative ion beams gave evidence that it was possible to transport around 80% of the negative ion beam obtained from the source through the section with deflecting magnets over a 3.5-m distance (the calorimeter inlet window being 30×30 cm^2). The negative ion beam was readily separated from the stripped fast atoms and accompanying particle flows formed during transportation [201].

6. Conversion targets for high-energy negative ion beams

Today, the injection of beams of fast hydrogen isotope atoms provides an important tool for plasma maintenance and heating in thermonuclear traps with magnetic confinement. Beam energies required for the purpose amount to hundreds of keV and may reach a few MeV in the future [202–204]. High-energy neutral beams can be obtained only by neutralizing accelerated ions in special conversion targets. A variety of gas or metal vapor targets were examined to convert a beam of positive ions of hydrogen isotopes into an atomic beam. However, the efficiency of neutralization decreases to below 0.2 at H^+ ion energies in excess of 100 keV (for D^+, over 200 keV). Therefore, the use of hydrogen negative ions is preferred, starting from an energy of 75 keV per nucleon [205]. In this case, the yield of atoms in metal vapor targets can be as high as 0.65 in the chosen particle energy range.

BINP researchers proposed to rely on a plasma target for negative ion beam conversion [3]. In this case, the atom yield resulting from the conversion of a negative ion beam into an atomic beam depends on the ratio between the detachment cross section of a weakly bound electron from a negative ion and the ionization cross section of the resultant atom: $\gamma = \sigma_{-10}/\sigma_{01}$. Then, the cross section of double ionization of a negative ion in a single collision is considered to be much smaller than cross sections of above processes ($\sigma_{11} \ll \sigma_{01}, \sigma_{-10}$). Therefore, the atom output from a target with optimal linear density is $N^0_{\rm opt} = 1/\gamma^{1/\gamma-1}$. The theoretical dependence of charge component fractions of the beam on σ_{-10}/σ_{01} is plotted in Fig. 80.

For the majority of gases, the ratio of cross sections is 2.5–3.5 and atom yield ranges 0.52–0.55 [206, 207]. The involvement of alkali metal vapor targets allows reaching $N^0_{\rm opt} = 0.6$ [208]. For a fully ionized plasma, the cross section of electron detachment from a negative ion markedly increases due to the absence of shielding of the long-range Coulomb potential for impact parameters of collisions smaller than the Debye radius. In the Born approximation, the dependence of the electron loss cross section on the relative velocity of colliding particles has the form $\sigma \sim \ln(mu^2/I)/(Iu^2)$, where m is the electron mass, and I is the electron affinity of the atom or the

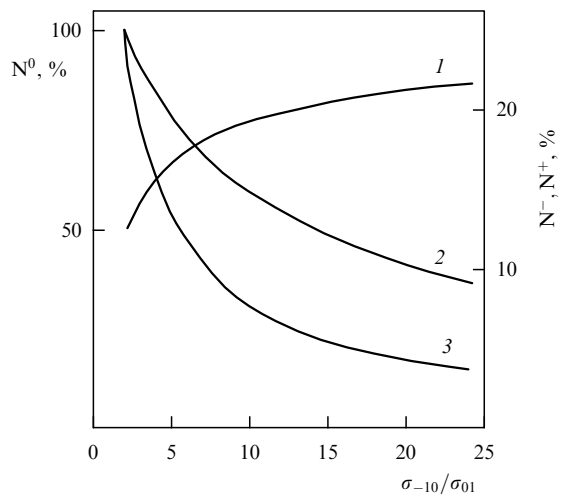

Figure 80. σ_{-10}/σ_{01} dependence of beam charge component fractions at optimal target thickness: *1* — atoms, *2* — negative ions, and *3* — protons.

atomic ionization potential. In other words, the cross-section ratio for targets from completely ionized hydrogen plasma weakly (logarithmically) depends on the collision energy as a result of fulfillment of the condition $mu^2/I \gg 1$; in fact, the cross-section ratio is roughly 20. For this cross-section ratio, atomic yield at an energy of several hundred keV or higher (when the applicability condition for the Born approximation is certainly satisfied) must be ~ 0.85.

In the experiments of G I Dimov and G V Roslyakov with lithium and magnesium plasma jets [209, 210], the yield of atoms amounted to almost 0.8 at a negative ion beam energy of 0.5–1 MeV. The yield proved to be somewhat higher for a lithium plasma target, and its variation over the entire energy range was $\sim 1\%$. Atomic yield for the magnesium plasma target was significantly smaller, and it tended to decrease with increasing beam energy. The difference between atomic yields for the energies of 970 and 370 keV was $\approx 2\%$. The lower atomic yield in magnesium plasma was attributable to the fact that the impact parameters of beam atom–ion collisions were commensurate with the size of the electron shell of Mg ions; it resulted in an appreciable increase in the atom ionization cross section upon collision [209, 210]. Direct measurements of cross-section ratios σ_{-10}/σ_{01} and $\sigma_{-11}/\sigma_{-10}$ in the lithium and magnesium plasmas [210] fully confirmed this conjecture.

It appears that a completely ionized hydrogen plasma provides the best working medium for plasma conversion targets (disregarding the possibility of using a plasma with multiply charged ions).

Table 2 presents cross-section values with the respective calculated optimal target thicknesses and atom yields. For the purpose of calculations, cross section $\sigma^{\mathrm{e}}_{-10}$ was assumed to be equal to $\sigma^{\mathrm{p}}_{-10}$. A certain nonmonotone behavior of the calculated target thickness and atomic yield arises from the scatter of experimental values of the respective cross sections.

The departure of target thickness from optimal values and the presence of unionized impurities in the plasma are the main causes behind the reduction in atomic yield. In the case of deviation of the target thickness from an optimal value ξ, a change in the yield of atoms is expressed as

$$\Delta N^0_{\mathrm{opt}} = -\frac{N^0_{\mathrm{opt}}}{2}\left(\frac{\Delta\xi}{\xi}\right)^2 \gamma\,\frac{\ln^2\gamma}{(\gamma-1)^2}\,.$$

For hydrogen plasma, the target thickness inhomogeneity may be significant: a $\pm 20\%$ inhomogeneity leads to an $\sim 1\%$ decrease in the atomic yield. Decreased atomic yield in the case of incomplete ionization of the target material is associated with lowering an effective cross-section ratio taking account of beam particle collisions with atoms and molecules. Figure 81 presents the calculated dependence of the maximum atomic yield in the target on the content of unionized impurity. Evidently, the impurity being molecular hydrogen, the plasma yield decreases but insignificantly, even at a relatively low degrees of ionization.

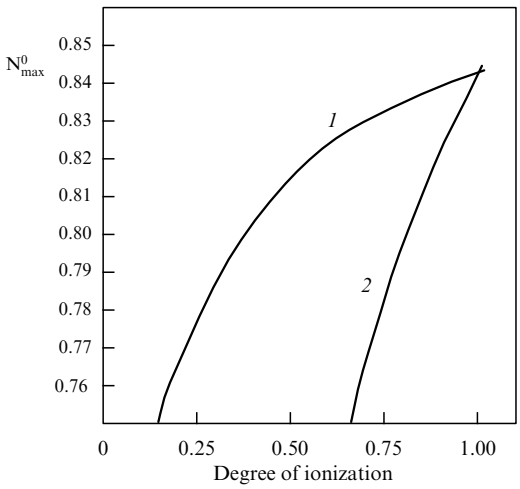

Figure 81. Calculated dependence of maximum atom yield from the target on its degree of ionization: *1* — molecular hydrogen admixture, and *2* — molecular nitrogen admixture.

When an electron is detached from a negative ion, the resulting atom may be either in the ground or in one of the excited states. It does not lead to further appreciable ionization of beam excited atoms, because the deactivation cross section of metastable atoms in collisions under these conditions exceeds the ionization cross section by an order of magnitude.

Experiments with a jet of hydrogen plasma [217] gave evidence of $84.5 \pm 0.5\%$ atomic yield at the energy of the hydrogen negative ion beam of around 500 keV. A schematic representation of the experimental design is given in Fig. 82.

Plasma source *1* produced a hydrogen plasma jet moving along magnetic field lines, the field which was created by the curved solenoidal plasma driver *2*. The straight section of the driver served to pump out the accompanying gas and purify plasma from molecular ions produced via dissociative recombination and ionization. After the plasma passed the turn, it entered the next 80-cm long straight section of the driver and functioned as the target for the negative ion beam undergoing conversion. The coil placed at the end of the driver created a field opposite in sign to the solenoid field, resulting in the formation of a cusp configuration, and the plasma jet was sent along the radius into the beam collector with a powerful pumping system. The solenoid magnetic field was roughly 1 kOe and did not appreciably deflect the

Table 2. Conversion target parameters taken from Refs [208–213].

Energy, keV	100	200	300	400	500	600	700	800	900	1000
$\sigma^{\mathrm{e}}_{-10}$	250	160	122	100	80	64	54	51	47	43
σ^{e}_{01}	7.05	6.25	5.0	4.17	3.53	2.96	2.56	2.32	2.11	1.94
σ^{p}_{01}	13.9	8.08	5.67	4.41	3.62	3.1	2.7	2.4	2.17	1.98
$\sigma^{\mathrm{e}}_{-11}$	4.9	4.15	3.2	2.75	2.25	2.0	1.75	1.55	1.4	1.25
Optimal target thickness, 10^{13} cm^{-2}	64	98	132	164	200	242	286	309	337	365
Atom yield, %	85.1	84.7	84.7	85.1	84.3	83.3	83.3	83.9	84.1	84.2

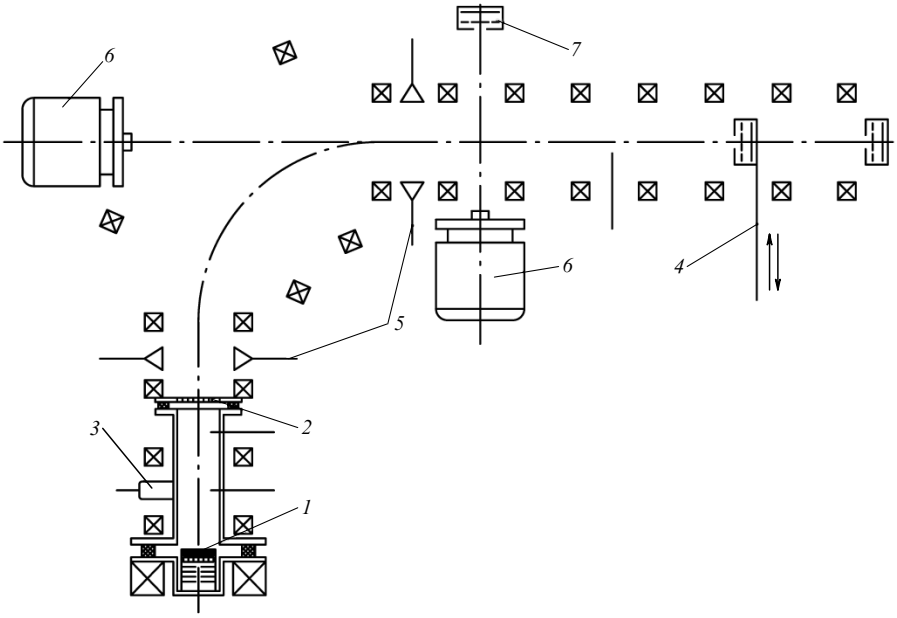

Figure 82. Schematic of an experiment [217]: *1* — plasma source, *2* — plasma driver, *3* — gas feed valve, *4* — diagnostic beam attenuation detector, *5* — microwave probe antenna, *6* — diagnostic beam injector, and *7* — beam detector.

primary negative ion beam with an energy of several hundred keV.

The plasma was generated in a discharge for which an LaB_6 disk 50 mm in diameter served as the cathode heated up to 1400–1500°C by an indirect heating spiral. The role of anode was played by a stainless steel grid installed approximately 35 cm from the cathode. The gas was puffed into the discharge chamber through a pulse valve at a rate of 10^{18} molecules per pulse. Discharge current varied in the range from 0.2 to 1 kA, and cathode voltage from 75 to 150 V, depending on cathode temperature and amount of hydrogen introduced into the discharge. Measurements with a mass spectrometer installed at the exit from the plasma source showed that plasma contained 85% H^+ ions and roughly 15% H_2^+ ions in the routine operating regime (with a plasma density of 10^{13} cm^{-3}). Plasma density in the discharge and plasma driver was measured using mobile Langmuir probes and estimated from the weakening of the atomic beam created by diagnostic injector *4* (see Fig. 82) and from the cut-off of microwave radiation with a wavelength of 7–11 mm. The section average density of the ionized gas across the jet was determined based on the weakening of the proton beam from the diagnostic injector.

Moreover, there were no appreciable losses during jet transport from the source with the aid of the curved solenoid (at densities above 2×10^{13} cm^{-3}). Plasma density after the turn decreased by approximately 20% due to recombination of molecular ions in the jet. Stabilization of the flute instability during plasma jet propagation in the curved solenoid took place due to the plasma jet freezing into the butt-end, where the cathode was located, as shown in special experiments in which the jet was cut off the cathode upon switching on the pulsed coil installed between the plasma source and the curved part of the solenoid to create a field opposite the solenoid field.

Figure 83 shows the characteristic shape of the signals from Langmuir probes placed outside the plasma at the outer and inner radii of the turn and of the current in the coil that cuts off the jet. When the coil field coincided with the direction of the solenoid field, the signals from both probes decreased similarly, perhaps due to a decline in the plasma flow passing through the local magnetic mirror (Fig. 83b). If the cut-off coil induced a counter-propagating field, an ejection of plasma occurred along the radial direction at the jet turning site (Fig. 83c, d). Further measurements demon-

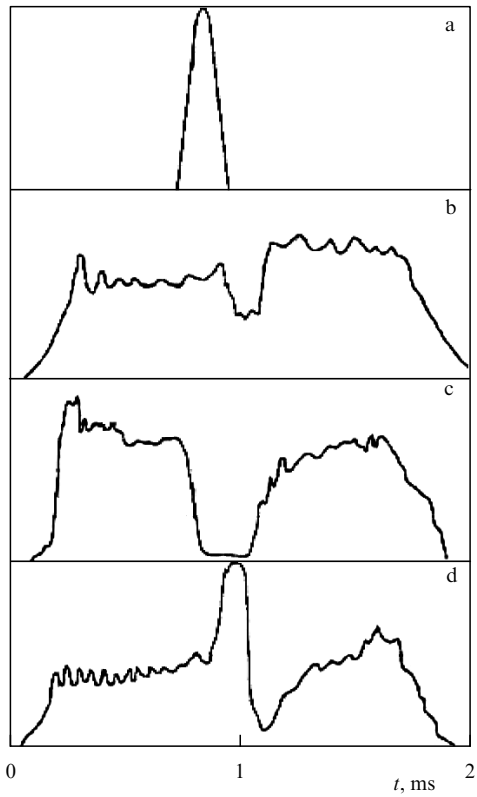

Figure 83. (a) Cut-off coil current; characteristic shape of time dependences of probe signals, (b) cut-off coil field direction coincides with that of solenoid field, and (c, d) cut-off coil field pointed away from the solenoid field.

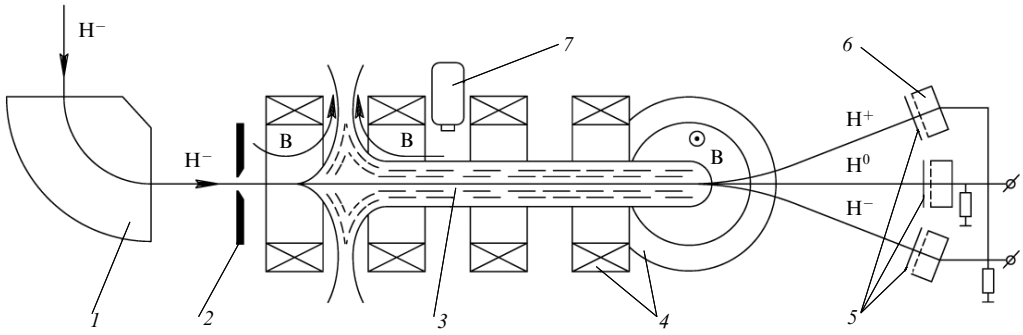

Figure 84. Schematic diagram of target conversion coefficient measurements: *1* — analyzing magnet, *2* — collimator, *3* — plasma target, *4* — solenoid, *5* — stripping films, *6* — Faraday cups, and *7* — gas valve.

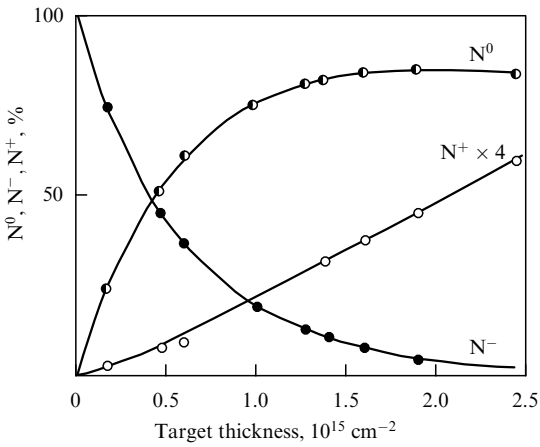

Figure 85. Beam charge components plotted versus target thickness.

strated that the jet moved in the curved solenoid field without appreciable losses or radial dispersion. The degree of plasma ionization after the turn was close to 100%.

Measurements of the conversion coefficient in the target were performed for a negative ion beam with a pulse duration of 0.3 ms and an energy of 500 keV coming from a Van de Graaff accelerator (Fig. 84). The negative ion beam from the accelerator passed through analyzing magnet *1* and collimator *2*. After passage through plasma target *3* in solenoid *4*, the beam diverged in the magnetic field of the bent section into charge components H^-, H^0, and H^+. Their currents were measured using Faraday cups *6* after stripping by 3500-Å thick lavsan (Dacron in the USA) films. The coefficient of conversion of all charge components of the beam to protons was roughly 0.999, which made unnecessary a calibration of signals from the atomic beam detector.

The results of the measurement of the yield of charge components from the weakening of the negative ion beam depending on the target linear thickness are presented in Fig. 85. The fraction of atoms reaches a maximum value of $(84.5 \pm 0.5)\%$ at a 2×10^{15} cm^{-2} target thickness, in agreement with the theory.

The development of an alternative variant of the plasma target with plasma confinement in the magnetic field of a multipole configuration is currently underway at BINP. This variant, unlike the jet flow target, may help to reduce energy expenditures for plasma generation. The vacuum chamber of the plasma trap used in the experiments was 120 cm long with a diameter of 20 cm. The butt-ends of the chamber had 10-cm holes for the passage of the beam undergoing neutralization.

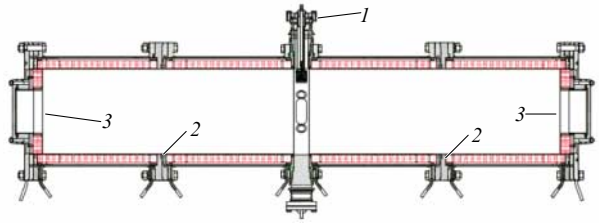

Figure 86. Schematic of a plasma target trap: *1* — cathodes, *2* — magnets, and *3* — holes for a beam passage.

The plasma is generated in the trap by gas ionization induced by electrons emitted from the cathodes in its central section. The trap had a total of six cathodes 17 mm in diameter made of LaB_6 and fitted with heaters. The cathodes were evenly arranged around the circumference at a certain distance from the beam passage region, so that electrons emitted from the cathode were injected into the trap in the radial direction. The total cathode current ranged 200–500 A, discharge voltage 100–400 V, and maximum discharge power was 200 kW. A schematic of the trap is presented in Fig. 86.

The multipole axially symmetric magnetic field of the trap was generated by permanent magnets installed from the outside on the thin-wall vacuum chamber. The field was strengthened by an iron yoke. The field change period was 1.5 cm, and its strength on the wall of the vacuum chamber was ~ 7 kG. The trap consisted of two parts, in each of which, a ~ 100-G paraxial longitudinal magnetic field was formed oppositely directed in its right and left halves. Annular magnets generated a magnetic field in the holes at the ends of the trap opposite that in the central region of the respective part of the device. It was expected that opposite magnetic fields would effectively curb the escape of plasma particles into the end holes due to generalized angular momentum conservation in the axially symmetric magnetic field. The multipole plasma target was tested on a bench schematically depicted in Fig. 87. Vacuum tanks were attached on either side of the trap for gas pumping and installation of diagnostic equipment.

Plasma density and its profile were determined with the aid of movable Langmuir probes; its density and degree of ionization were measured by probing plasma with a 5–10-keV atomic beam. The beam to be injected had to pass through the target plasma and reach a magnetic analyzer, where it was divided into three charge components, viz. hydrogen atoms, protons, and hydrogen negative ions. Charged beam compo-

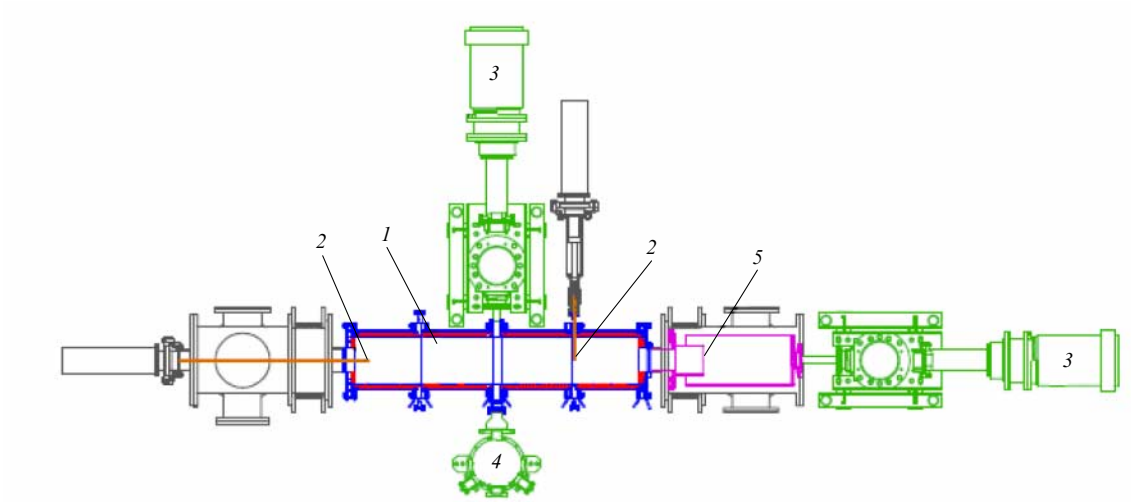

Figure 87. Schematic of a plasma target test bench (top view): *1* — plasma target, *2* — probes, *3* — diagnostic neutral beam injector, *4* — passed beam analyzer, and *5* — plasma flow density meter.

nents were registered by Faraday cups, and the atomic component by a secondary emission detector. The diagnostic beam and analyzer can be arranged both at the ends of the trap and along the radius in its central part. Plasma density in the trap and the degree of its ionization could be determined independently based on variations in charge component currents. One of the vacuum tanks contained a specially designed collector to measure the plasma flow.

Plasma density showed a linear dependence on the discharge power. At 200 kW, the plasma density in the central region of the trap amounted to $n_i = 2.2 \times 10^{13}$ cm^{-3}. The electron temperature was equal to 3–5 eV. Plasma density profiles in the radial and axial directions (near the outlet hole), shown in Fig. 88, suggest that the plasma was confined in the central region of the trap. Its density fell dramatically on approaching the walls of the vacuum chamber (Fig. 88a), but remained virtually constant along the trap axis.

Plasma densities measured by charge exchange of an atomic beam fairly well agree with probing data. Plasma density in the central section of the trap is $n_i > 2 \times 10^{13}$ cm^{-3}. The degree of plasma ionization in the central section measured by the charge-exchange method as applied to an atomic beam is $50^{+10\%}_{-5\%}$.

Measurements of the full plasma flow outgoing from the hole intended for the beam to be neutralized demonstrated the efficiency of bounding the flow into the hole by the oppositely directed magnetic field. The plasma flow into the hole was almost 30 times smaller than the unbounded one. Further experiments are designed to enhance plasma ionization in the target and increase the efficiency of its generation.

One promising neutralization technique for negative ion beams involves the use of a photon target based on the electron photodetachment reaction [218]. The quantum energy is higher than the electron affinity energy but lower than the ionization potential of the hydrogen atom, which allows, in principle, coefficients of negative ion beam conversion close to 100% to be obtained. The degree of neutralization of a negative ion beam in the photon target is given by the expression [219]

$$\eta = \frac{J_0}{J_-} = 1 - \exp\left(-\frac{\sigma c P}{\hbar\omega d V_i}\right), \qquad (6.1)$$

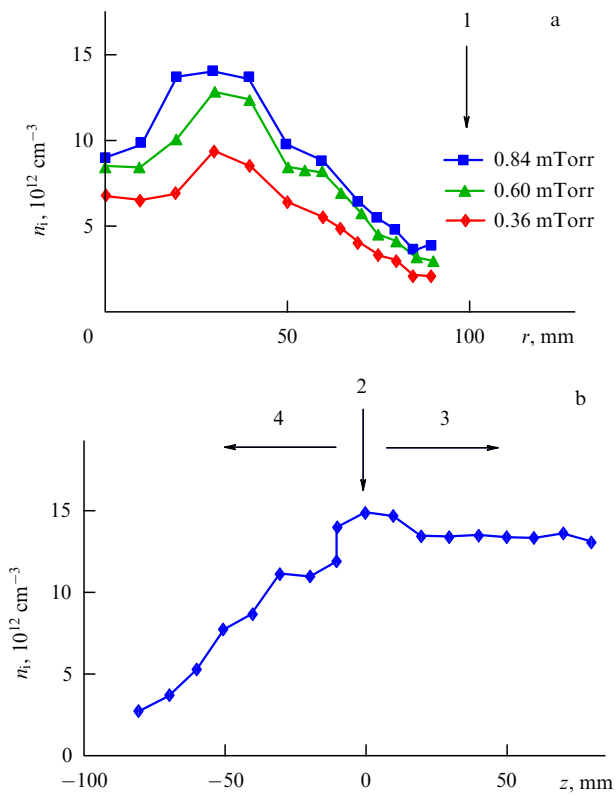

Figure 88. Plasma density profile: (a) in the radial direction, and (b) along the axis near the outlet; *1* — vacuum chamber surface, *2* — butt-end surface of vacuum chamber, *3* — interior of the trap, and *4* — area around the hole for beam passage.

where J_0, J_- are the neutral atom and negative ion currents, respectively, c is the speed of light, σ is the photodetachment cross section, P is the radiation power density inside the trap, V_i is the particle velocity, $\hbar\omega$ is the photon energy, and d is the length of the photon-occupied region.

In view of the small photodetachment cross section, photons have to cross the negative ion beam many times to ensure a high-degree neutralization (above 90%). It is achieved by the employment of a mirror system confining radiation within itself. A variety of scenarios have been

proposed for the purpose [219–222] based on different variants of the Fabry–Perot cavity. Modern technologies make it possible, in principle, to create such photon targets, but a large number of challenging technical problems remain to be solved. Specifically, high-reflectivity (above 0.999) mirrors resistant to incident radiation of several hundred kilowatts per cm^2 and requiring intense cooling are needed. Moreover, thermal stabilization of the entire mirror system must be ensured and rigorous demands on the quality of laser radiation met to fulfill the phase synchronism condition for a large number of passes. The current state of research on resonant photon targets is overviewed in Refs [222, 223].

An alternative approach covers nonresonant photon accumulation [224, 225]. Such a concept of the photon trap reduces to a system of reflective surfaces capable of multiple beam reflection. The basic principle behind the device is well described in terms of a mathematical billiard system [226] with a wide enough range of billiard trajectories stable in the phase space. The energy density in this system increases in proportion to the beam lifetime. The integral lifetime in a photon trap is largely determined, as it is in a resonant photon accumulator, by photon losses due to reflections and photon escape time from the system, because the mirrors cannot form a closed surface. The essential difference between this and resonant accumulators is the absence of stringent conditions imposed on the phase relationships between the large number of rays in its interior and radiation input through a highly reflective surface, rather than through one or several small holes. Long-term retention of photons is ensured by conservation of certain adiabatic invariants. The efficiency of photon accumulation is virtually independent of the quality of injected radiation, which allows considering a relatively cheap commercial high-efficiency optical fiber laser a potential radiation source.

The nonresonant photon accumulation concept proposed in Ref. [224] suggests conservation inside the trap of some adiabatic invariants bounding the photon-occupied region instead of exact phase relationships between the rays at different stages of evolution. Such accumulation is analogous to the confinement of charged particles in open magnetic traps, as proposed by G I Budker [227].

Let us consider the two-dimensional configuration of the mirrors. Figure 89 shows that a photon acquires an additional horizontal momentum in the direction of the height maximum between the mirrors after each new reflection. At small deviations from vertical motion, the photon tends toward the central 'equilibrium' position.

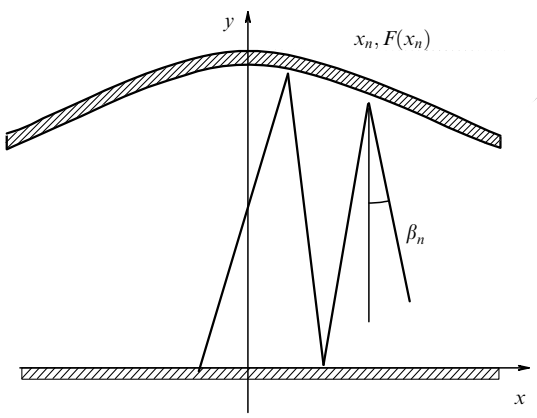

Figure 89. Schematic diagram of a quasiplanar photon trap.

Let us define the photon position immediately after its n-th reflection by the abscissa of the reflection point x_n, its height $F(x_n)$, and the angle β_n between the vertical line and photon velocity (see Fig. 89). The horizontal movement is then described by the following set of equations:

$$x_{n+1} - x_n = \big(F(x_{n+1}) + F(x_n)\big) \tan \beta_n \,, \tag{6.2}$$

$$\beta_{n+1} - \beta_n = 2\,\frac{\mathrm{d}F(x_{n+1})}{\mathrm{d}x} \,. \tag{6.3}$$

Linearization of the (6.2), (6.3) system to study stability gives

$$x_{n+1} - x_n = 2F(0)\beta_n \,, \tag{6.4}$$

$$\beta_{n+1} - \beta_n = 2\,\frac{\mathrm{d}^2F(0)}{\mathrm{d}x^2}\, x_{n+1} \,. \tag{6.5}$$

Combining expressions (6.4) and (6.5) leads to the following linear recurrent relationship:

$$x_{n+2} - 2x_{n+1} + x_n = 4F(0)\,\frac{\mathrm{d}^2F(0)}{\mathrm{d}x^2}\, x_{n+1} = -4F(0)\,\frac{x_{n+1}}{R} \,, \tag{6.6}$$

where R is the radius of curvature of the upper mirror. The stability condition of equation (6.6) is easy to find as

$$F(0) < R \,. \tag{6.7}$$

Evidently, the fulfillment of inequality (6.7) conserves the adiabatic invariant

$$F(x)\cos\beta = \text{const} \,, \tag{6.8}$$

limiting the region occupied by photons.

The possible geometry of a photon accumulator based on this principle is presented in Fig. 90. Each mirror consists of a cylindrical part conjugated with spherically shaped mirrors docked at the ends. Clearly, the radii of both cylindrical and spherical mirrors are equal. End mirror may have a different shape provided that it ensures a gradual decrease in the distance between the upper and lower mirrors during movement from the center of the trap. Photon motion along the z-axis in such a system is essentially anharmonic. It was shown in Ref. [228] that the lifetime of radiation injected into such an accumulator is largely determined by the reflectivity of the mirrors. Radiation storing efficiency thus achieved proved sufficient for experiments on neutralization of hydrogen and

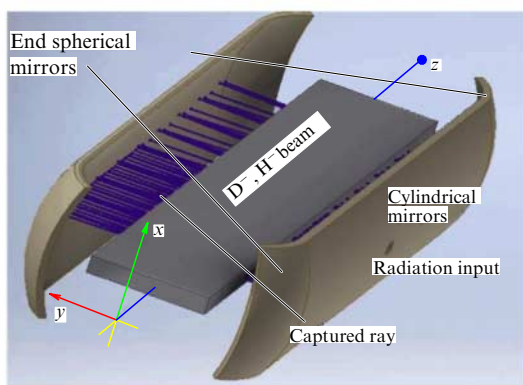

Figure 90. Schematic of an elongated adiabatic photon trap.

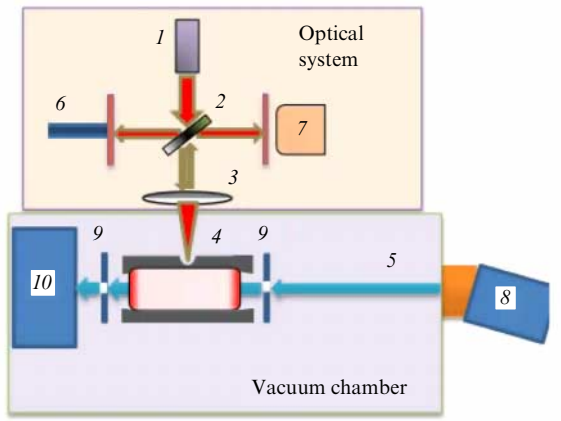

Figure 91. Schematic diagram of measuring the negative ion beam neutralization coefficient: *1* — laser radiation, *2* — beam splitter, *3* — lens, *4* — photon accumulator, *5* — vacuum chamber, *6* — light guide, *7* — CCD, *8* — magnet, *9* — diaphragms, and *10* — analyzer.

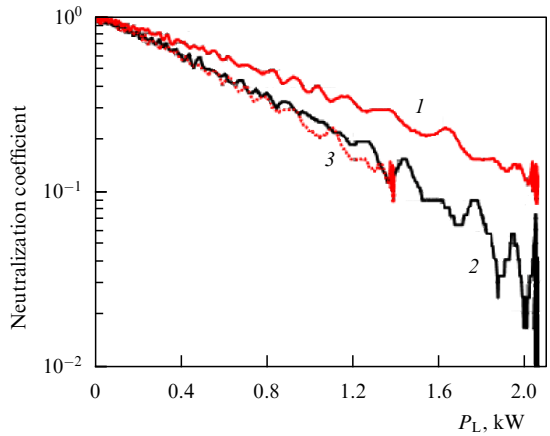

Figure 92. Neutralization coefficient plotted vs laser radiation power P_L. Curves *1, 2* correspond to hydrogen and deuterium ions, and curve *3* is $\sqrt{U_D m_H/(m_D U_H)}$ times horizontally compressed curve *1*.

deuterium negative ion beams with a particle energy of $\sim$ 10 keV [229, 230].

The experimental setup is schematically depicted in Fig. 91. Laser radiation *1* passes through beam splitter *2* and is focused by lens *3* onto the inlet of photon accumulator *4* inside vacuum chamber *5*. The input angular spread determined mostly by the focal length is about 3°. An antireflective beam splitter directs a minor part of the injected radiation to light guide *6* for monitoring input radiation power. The use of a charge-coupling device (CCD) *7* ensures precise control of the laser ray and its direction exactly into the inlet hole.

H^- and D^- beams were generated using the DINA-4A injector [231]. The ion beam from the injector passed through the gas target after which negative ions were separated from other charge fractions by magnet *8*. A narrow negative ion beam cut out by diaphragms *9* was sent to the photon target and reached magnetic analyzer *10* at the exit from it. The two-channel design made possible simultaneous registration of positive and negative ions in the beam behind the photon target. The beam energy varied from 6 to 12 keV. Pulse duration was $\sim$ 150 μs.

Experiments reported in Ref. [229] yielded dependences of negative ion current on the injected radiation power (Fig. 92). Curves *1* and *2* for H and D ions correspond to the

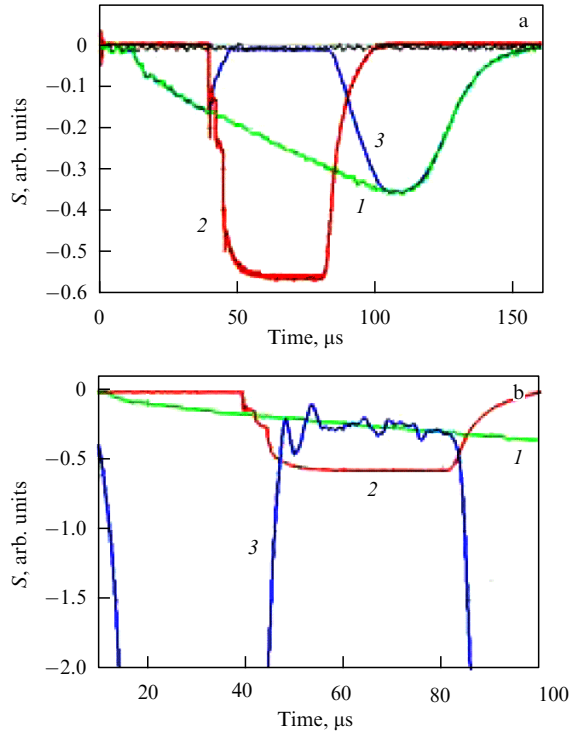

Figure 93. Oscillograms of the signals from negative ion beam neutralization. Curve *1* — variation of D^- current without neutralization, curve *2* — data from the laser pumping monitor, and curve *3* — D current at laser switch-on.

exponential dependence, which excludes all ionization mechanisms besides photodetachment.

Maximum degree of neutralization was observed in experiments with $\sim$ 6-keV deuterium ions and more accurate adjustment of the beam axis to the center of the optical target [228]. Typical oscillograms obtained in these experiments are presented in Fig. 93a. In Fig. 93b, curve *1* at the time interval of $\approx 45-85$ μs and curve *3* extended in the vertical direction with the aid of an *ad hoc* scaling factor are practically superimposed. The best coincidence of the curves was obtained with the scaling factor of 50 ± 4 corresponding to a $98\% \pm 0.2\%$ degree of neutralization. The fraction of positive particles at the exit from the neutralizer was below the noise level equivalent to 0.1% of the signal amplitude.

Results of the above experiments provide convincing evidence of the possibility of efficient radiant energy accumulation from a low-quality photon beam unsuitable for traditional approaches with the use of Fabry–Perot cells. Reference [233] presents a conceptual project of a nonresonant neutralizer for higher than 90% neutralization at a total injected radiation power of 310 kW for the powerful neutral injection systems currently under design and construction [232]. Industrial high-performance optical fiber lasers may serve as radiation sources [234]. The biggest technological challenge to be addressed is the manufacture of highly reflective (0.9995) mirrors having a large (0.5×8 m^2) area. Such mirrors can be composed of smaller segments with minimal gaps between them.

An advantage of such an approach is that it does not require a powerful narrow-band master laser emitting ultrahigh-quality radiation, nor does it need an expensive complex system for stabilizing and adjusting resonator elements.

7. Conclusion

An important distinctive feature of research on ion sources and neutral beam injectors based at BINP is that these studies were from the very beginning intended to facilitate the solution to specific problems in the framework of general institutional programs. The internationally recognized scientific value of these studies (charge exchange injection, breakthrough design of open plasma traps [235–237], etc.) has always had a positive impact on the choice of approaches to the development of ion sources and injectors, as well as on the level of achievements in this field. Immediate plans for further work on ion sources include the creation of continuous atomic beam injectors with a power up to 10 MW to promote implementation of the BINP program aimed at the construction of open plasma traps of the next generation.

The plans envisage the development of a stationary gas discharge multiple mirror trap (GDMT) based on the concept of multimirror end solenoids for the further reduction of plasma longitudinal losses, in comparison with the losses in a gas-dynamic trap [238, 239]. Certainly, the device must have a superconducting magnet system to reach stationary conditions with microwave heating time and duration of heating by atomic beam injection on the order of 100 s. The primary objective of the GDMT experiment is to validate the concept of the stationary multimirror thermonuclear D – T reactor. Given that the problem of stability under high plasma pressure and temperature has been successfully solved, GDMT will possibly be used as a basic component of 'low-neutron' schemes of fusion reactors with the use of such fuel components as $D-He^3$, He^3-He^3, and $p-B^{11}$.

Acknowledgments

The authors thank V G Dudnikov for furnishing us with materials partly used in writing Section 1. The important contribution from the BINP staff members V V Anashin, I A Kotel'nikov, V Ya Savkin, A S Donin, A V Burdakov, S V Polosatkin, A A Lizunov, A A Listopad, and A S Medvedko in different periods of ion source physics research is gratefully acknowledged. Special thanks are due to them for enlightening discussions of various aspects of these studies. The authors wish to express deep gratitude to B Schweer, A Kreter, W Ulemann (Forschungszentrum Informatik, FZJ, Germany), A Smirnov, S Putvinsky, A Dunaevsky (TAE, USA), A Karpushov (École polytechnique fédérale de Lausanne (EPFL, Switzerland), and G Fiksel (University of Wisconsin, USA) for fruitful discussions. Staff members of the Research and Development Department, BINP, V V Mishagin, V V Kobets, A I Gorbovsky, V Kh Amirov, V P Belov, A N Vil'kin, L P Rukhlyad, V S Khrestolyubov, A Yu Protopopov, N G Vasil'eva, O M Dergacheva, F K Klyaus, A V Sitnikov, R A Nemirovskaya, and B Ya Kremyansky have been able to perform a titanic work to accomplish the Herculean task of designing ion sources and injectors. The study was supported by the Russian Science Foundation (project 14-50-00080).

References

1. Budker G I, Dimov G I, in *Trudy Mezhdunarodnoi Konf. po Uskoritelyam, Dubna, 21–27 August, 1963* (Eds A A Kolomenskii et al.) (Moscow: Atomizdat, 1964) p. 933
2. Dimov G I, Thesis for Doct. Phys.-Math. Sci. (Novosibirsk: Budker Institute of Nuclear Physics, SB USSR Acad. Sci., 1968)
3. Dimov G I, Preprint No. 304 (Novosibirsk: Budker Institute of Nuclear Physics, SB USSR Acad. Sci., 1969)
4. Donally B L, Thoeming G *Phys. Rev.* **159** 87 (1967)
5. Faircloth D, arXiv:1302.3745
6. Laurence G P, Beauchamp R K, McKibben J L *Nucl. Instrum. Meth.* **35** 357 (1965)
7. Ehlers K W, Gavin B F, Hubbard E L *Nucl. Instrum. Meth.* **22** 87 (1963); Ehlers K W *Nucl. Instrum. Meth.* **32** 309 (1965)
8. Belchenko Yu I et al., in *Trudy Mezhdunarodnoi Konf. po Uskoritelyam Zaryazhennykh Chastits Vysokikh Energii, Protvino, July 1977* Vol. 1 (Serpukhov, 1977) p. 287
9. Dimov G I, Preprint No. 46 (Novosibirsk: Budker Institute of Nuclear Physics, SB USSR Acad. Sci., 1977)
10. Davydenko V I, Roslyakov G V, Savkin V Ya *Vopr. Atom. Nauki Tekh. Termoyad. Sintez* (2) 67 (1983)
11. Davydenko V I, Ivanov A A, in *Fusion Physics* (Eds M Kikuchi, K Lackner, M K Tran) (Vienna: International Atomic Energy Agency, 2012) p. 435
12. Sasao M et al. *IEEE Trans. Plasma Sci.* **33** 1872 (2005)
13. Listopad A et al. *Rev. Sci. Instrum.* **83** 02B707 (2012)
14. Hess W R et al., in *Proc. of the 24th EPS Conf. on Controlled Fusion and Plasma Physics* Vol. 21A, Pt. I (1997) p. 189
15. Kislyakov A I, Krupnik L I *Sov. J. Plasma Phys.* **7** 478 (1981); *Fiz. Plazmy* **7** 866 (1981)
16. Bel'chenko Yu I et al. *Sov. Phys. Dokl.* **18** 814 (1974); *Dokl. Akad. Nauk SSSR* **213** 1283 (1973)
17. Belchenko Y I, Dimov G I, Dudnikov V G *Nucl. Fusion* **14** 113 (1974)
18. Zhiltsov V A et al. *Nucl. Fusion* **40** 509 (2000)
19. Hanada M et al. *Rev. Sci. Instrum.* **75** 1813 (2004)
20. Ivanov A A, Roslyakov G V *Zh. Tekh. Fiz.* **50** 2300 (1980)
21. Gabovich M D *Fizika i Tekhnika Plazmennykh Istochnikov Ionov* (Physics and Technology of Plasma Ion Sources) (Moscow: Atomizdat, 1972)
22. Meshkov I N *Transportirovka Puchkov Zaryazhennykh Chastits* (Transport of Charged Particle Beams) (Novosibirsk: Nauka, 1991)
23. Brown I G (Ed.) *The Physics and Technology of Ion Sources* (New York : Wiley, c1989); Translated into Russian: *Fizika i Tekhnologii Istochnikov Ionov* (Moscow: Mir, 1998)
24. Gabovich M D, Pleshivtsev N V, Semashko N N *Ion and Atomic Beams for Controlled Fusion and Technology* (New York: Consultants Bureau, 1989); Translated from Russian: *Puchki Ionov i Atomov dlya Upravlyaemogo Termoyadernogo Sinteza i Tekhnologicheskikh Tselei* (Moscow: Energoatomizdat, 1986)
25. Alvarez L W *Rev. Sci. Instrum.* **22** 705 (1951)
26. Budker G I, Skrinsky A N, in *Orsay Symposium on Colliding Beams* (1966)
27. VAPP NAP Group Report, in *Proc. of the VIII Intern. Conf. on High Energy Accelerators* (Geneva: CERN, 1971)
28. Dimov G I, Sukhina B N *Prib. Tekh. Eksp.* (1) 16 (1968)
29. Budker G I et al. *At. Energ.* **19** 507 (1965)
30. Dimov G I et al. *Prib. Tekh. Eksp.* (4) 30 (1967)
31. Dimov G I et al. *Zh. Tekh. Fiz.* **38** 997 (1968)
32. Dimov G I, Roslyakov G V *Prib. Tekh. Eksp.* (2) 33 (1974)
33. Dimov G I, Roslyakov G V *Prib. Tekh. Eksp.* (3) 31 (1974)
34. Budker G I et al., Preprint No. 510 (Novosibirsk: Budker Institute of Nuclear Physics, SB USSR Acad. Sci., 1977)
35. Budker G I, Dimov G I, Dudnikov V G, in *Proc. of the Intern. Symp. on Electron and Positron Storage Ring* Rep. VIII, 6.1 (France, Sakley, 1966)
36. Budker G I, Dimov G I, Dudnikov V G *Sov. Atomic Energy* **22** 441 (1967); *At. Energ.* **22** 348 (1967)
37. Dudnikov V G, Thesis for Cand. Phys.-Math. Sci. (Novosibirsk: Budker Institute of Nuclear Physics, SB USSR Acad. Sci., 1974)
38. Dimov G I, Chupriyanov V E *Particle Accelerators* **14** 155 (1984)
39. Dimov G I, Shamovskii V E, Chupriyanov V E *Sov. Phys. Tech. Phys.* **16** 1662 (1971); *Zh. Tekh. Fiz.* **41** 2098 (1971)
40. Chirikov B V *At. Energ.* **36** 1239 (1966)
41. Dimov G I *Rev. Sci. Instrum.* **67** 3393 (1996)
42. Budker G I et al., in *Proc. of the VI Intern. Conf. on High Energy Accelerators, 1967*

43. Budker G I *Plasma Physics and the Problem of Controlled Thermonuclear Reactions* Vol. 3 (Ed. M A Leontovich) (New York: Pergamon Press, 1959) p. 1; Translated from Russian: in *Fizika Plasmy i Problema Upravlyaemykh Termoyadernykh Reaktsii* Vol. 3 (Ed. M A Leontovich) (Moscow: Izd. AN SSSR, 1958) p. 3
44. Feinberg E L (Ed.) *Vospominaniya o I.E. Tamme* (The Memoirs of I.E. Tamm) 3rd ed. (Moscow: IzdAT, 1995) p. 166
45. Golovin I N et al. *Sov. Phys. Usp.* **4** 323 (1961); *Usp. Fiz. Nauk* **73** 685 (1961)
46. Barnett et al., in *Izbrannye Doklady Inostrannykh Uchenykh na II Zhenevskoi Konf. po Mirnomu Ispol'zovaniyu Atomnoi Energii* (Selected Reports of Foreign Scientists at the 2nd Geneva Conf. on the Peaceful Uses of Atomic Energy) (Moscow, 1959) p. 302
47. Sweetman B *Nucl. Fusion Suppl. Conf. Proc.* (Saltsburg, 1962)
48. Luk'yanov S Yu *Goryachaya Plazma i Upravlyaemyi Termoyadernyi Sintez* (Hot Plasma and Controlled Nuclear Fusion) (Moscow: Nauka, 1975)
49. Davydenko V I et al. *AIP Conf. Proc.* **1771** 030025 (2016)
50. Barry L A, in *Symp. on Plasma Heating in for Devices, Varenna-Italy, Bologna, 1974*, p. 151
51. Coensgen F N et al., in *VII Eur. Conf. on ol. Fusion and Plasma Physics, Losanne, 1975*
52. Andrews M L et al. *Phys. Rev. Lett.* **27** 1428 (1971)
53. Rostoker N, Binderbauer M W, Monkhorst H J *Science* **278** 1419 (1997)
54. Tuszewski M *Nucl. Fusion* **28** 2033 (1988)
55. Gibson A, in *Tokamak Experiments. Proc. of the 11th Intern. Conf. on Plasma Physics and Controlled Nuclear Fusion Research* (Kyoto, 1986); *Nucl. Fusion* **27** 481 (1987)
56. Coensgen F H et al., in *Proc of the 6th Intern. Conf. on Plasma Physics and Controlled Nuclear Fusion Research* (Berchtesgaden, 1976); in *Proc of the 6th Intern. Conf. on Plasma Physics and Controlled Nuclear Fusion Research* Vol. 3 (Vienna, 1977) p. 135
57. Simonen T C et al. *Phys. Rev. Lett.* **50** 1668 (1983)
58. Binderbauer M W et al. *Phys. Plasmas* **22** 056110 (2015)
59. Mirnov V V, Ryutov D D *Pis'ma Zh. Tekh. Fiz.* **5** 678 (1979)
60. Davydenko V I et al. *Sov. Phys. Tech. Phys.* **28** 160 (1983); *Zh. Tekh. Fiz.* **53** 258 (1983)
61. Davydenko V I et al., Preprint 1982-049 (Novosibirsk: Budker Institute of Nuclear Physics, SB USSR Acad. Sci., 1982)
62. Davydenko V I et al., in *Tezisy Dokladov 6 Vsesoyuz. Konf. po Plazmennym Uskoritelyam i Ionnym Inzhektoram* (Proc. of the 6th All-Union Conf. on Plasma Accelerators and Ionic Injectors)
63. Davydenko V I et al. *Prib. Tekh. Eksp.* (6) 39 (1986)
64. Davydenko V I, Roslyakov G V, Khavin N G *Prib. Tekh. Eksp.* (5) 21 (1981)
65. Kel'man V M, Yavor S A *Elektronnaya Optika* (Electronic Optics) (Leningrad: Nauka, 1968) p. 132
66. Derevyankin G E, Dudnikov V G, Zhuravlev P A *Prib. Tekh. Eksp.* (5) 168 (1970)
67. Roslyakov G V *Prib. Tekh. Eksp.* (2) 167 (1981)
68. Davydenko V I et al., Preprint No. 163 (Novosibirsk: Budker Institute of Nuclear Physics, SB USSR Acad. Sci., 1989)
69. Davydenko V I et al. *Plasma Phys. Rep.* **23** 396 (1997); *Fiz. Plazmy* **23** 427 (1997)
70. Dimov G I et al. *Zh. Tekh. Fiz.* **38** 6 (1968)
71. Ivanov F F et al. *Rev. Sci. Instrum.* **71** 3728 (2000)
72. Deichuli P P et al., Preprint No. 037 (Novosibirsk: Budker Institute of Nuclear Physics, 2003)
73. Deichuli P P et al. *Rev. Sci. Instrum.* **77** 03B514 (2006)
74. Davydenko V I et al., in *Trudy Vsesoyuznogo Soveshchaniya po Otkrytym Lovushkam* (Proc. of the All-Union Conf. on Open Traps) (Moscow: Energoatomizdat, 1989) p. 24
75. Deichuli P P et al. *Rev. Sci. Instrum.* **75** 1816 (2004)
76. Fiksel G et al. *Bull. Am. Phys. Soc.* **46** (8) (2001)
77. Ivanov A A et al. *Plasma Phys. Rep.* **28** 196 (2002); *Fiz. Plazmy* **28** 221 (2002)
78. Ivanov A A et al., Preprint 2002-41 (Novosibirsk: Budker INP, 2002)
79. Prokhorov I A et al. *Fusion Sci. Technol.* **63** 349 (2013)
80. Sorokin A, Belov V, Davydenko V *Rev. Sci. Instrum.* **81** 02B108 (2010)
81. Deichuli P P et al. *Rev. Sci. Instrum.* **83** 02B114 (2012)
82. Karpushov A N, Alberti S, Chavan R *Fusion Eng. Design* **96–97** 493 (2015)
83. Deichuli P P, Ivanov A A, Stupishin N V *Rev. Sci. Instrum.* **79** 02C106 (2008)
84. Davydenko V I, Ivanov A A, Shul'zhenko G I *Plasma Phys. Rep.* **41** 930 (2015); *Fiz. Plazmy* **41** 1004 (2015)
85. Roslyakov V G, Thesis for Doct. Phys.-Math. Sci. (Novosibirsk: Budker Institute of Nuclear Physics, SB USSR Acad. Sci., 1987)
86. Deichuli P P et al. *Rev. Sci. Instrum.* **86** 113509 (2015)
87. Anderson J K et al. *Trans. Fusion Sc. Technol.* **59** 27 (2011)
88. Boers J E, in *Proc. IEEE Particle Accelerator Conference* (New York: American Physical Society, 1995) p. 2312
89. Karpushov A N et al. *Fusion Eng. Design* **123** 468 (2017)
90. Spädtke P, KOBRA3-INP, INP, Junkernstr. 99, 65205 (Wiesbaden, Germany, 2004)
91. Menon M M et al. *Rev. Sci. Instrum.* **56** 242 (1985)
92. Stirling W L, Tsai C C, Ryan P M *Rev. Sci. Instrum.* **48** 533 (1977)
93. Panasenkov A A, Romanov V I, Seregin V S, Preprint IAE-3375 (Moscow: IAE, 1980); Ehlers K W, Kunkel W B, in *Proc. of the Intern. Conf. on Ion Sources* (Vienna: SGAE, 1972) p. 259; Speth E et al., in Beaumont B et al. (Eds) *Proc. of the 20th Symp. on Fusion Technology, Marseille, 1998* (Saint Paul Lez Durance, 1998) p. 27; PVA TePla AG, https://www.pvatepla.com/
94. Davydenko V I, Ivanov A A *J. Plasma Fusion Res.* **3** 456 (2000)
95. ANSYS, https://www.ansys.com/
96. Alinovsky N I et al. *Tech. Phys.* **54** 1350 (2009); *Zh. Tekh. Fiz.* **79** (9) 10 (2009)
97. Alinovsky N I et al., in *RUPAC* (Russia, 2008)
98. Astrelin V T et al. *J. Nucl. Mater.* **396** 43 (2010)
99. Prikhodko V V et al. *AIP Conf. Proc.* **1771** 050014 (2016)
100. Sorokin A V et al. *AIP Conf. Proc.* **1771** 030026 (2016)
101. Semashko N N et al. *Inzhektory Bystrykh Atomov Vodoroda* (Injectors of Fast Hydrogen Atoms) (Moscow: Energoatomizdat, 1981) p. 124
102. Ivanov A A et al. *Rev. Sci. Instrum.* **85** 02B102 (2014)
103. Belchenko Yu I et al. *Rev. Sci. Instrum.* **87** 02B316 (2016)
104. Bender E D *Vopr. Atom. Nauki Tekh. Termoyad. Sintez* (4) 41 (1987); Bender E D, Kuznetsov G F, Savkin V Ya *Prib. Tekh. Eksp.* (2) 144 (1987)
105. Deichuli P P et al. *Rev. Sci. Instrum.* **75** 1822 (2004)
106. Combs S K, Milora S L, Foster C A *Rev. Sci. Instrum.* **56** 1526 (1985)
107. Naumov V G, Semashko N N *Vopr. Atom. Nauki Tekh. Termoyad. Sintez* (1) (1980)
108. Euringer E, Lochter M, Pfister U, in *IEEE 13th Symp. on Fusion Engineering* Vol. 2 (1989) p. 991
109. Deichuli P P, Khrestolyubov V S, in *XLI Mezhdunarodnaya Zvenigorodskaya Konf. po Fizike Plazmy i UTS, Zvenigorod, 2014* (XLI Intern. Zvenigorod Conf. on Plasma Physics and Controlled Thermonuclear Reactions, Zvenigorod, 2014)
110. Dimov G I, Roslyakov G V, Savkin V Ya *Prib. Tekh. Eksp.* (4) 29 (1977)
111. Roslyakov G V, Savkin V Ya *Prib. Tekh. Eksp.* (1) 148 (1978)
112. Dimov G I, Roslyakov G V *Prib. Tekh. Eksp.* (1) 29 (1974)
113. Dimov G I, Roslyakov G V, Savkin V Ya *Prib. Tekh. Eksp.* (4) 29 (1977)
114. Abdrashitov G F et al., in *Proc. XVIII Symp. on Fusion Techn.* Vol. 1 (Karlsruhe, Germany, 1994) p. 601
115. Davydenko V I, Morozov I I, Roslyakov G V *Fiz. Plazmy* **7** 464 (1981)
116. Davydenko V I, Roslyakov G V, Savkin V Ya, Preprint 1983-014 (Novosibirsk: Budker Institute of Nuclear Physics, SB USSR Acad. Sci., 1983)
117. Korepanov S A et al. *Rev. Sci. Instrum.* **75** 1829 (2004)
118. Waksman J et al. *Phys. Plasmas* **19** 122505 (2012)
119. Shikhovtsev I V et al. *Rev. Sci. Instrum.* **75** 1844 (2004)
120. Hintz E, Schweer B *Plasma Phys. Control Fusion* **37** A87 (1995)
121. Davydenko V I, Ivanov A A *Rev. Sci. Instrum.* **75** 1809 (2004)

122. Davydenko V I et al. *Diagnostika Plazmy* (Diagnosis of Plasma) Issue 5 (Moscow: Energoatomizdat, 1986) p. 147
123. Davydenko V I, Dimov G I, Roslyakov G V *Sov. Phys. Dokl.* **28** 685 (1983); *Dokl. Akad. Nauk SSSR* **271** 1380 (1983)
124. Berezovskii E L et al. *Pis'ma Zh. Tekh. Fiz.* **8** 1382 (1982)
125. Berezovskii E L et al., in *Diagnostika Plazmy* (Diagnosis of Plasma) Issue 5 (Moscow: Energoatomizdat, 1986) p. 157
126. Abdrashitov G F, Davydenko V I, Deichuli P P *Rev. Sci. Instrum.* **72** 594 (2001)
127. Bender E D et al. *Prib. Tekh. Eksp.* (6) 78 (1996)
128. Den Hartog D J et al. *Rev. Sci. Instrum.* **77** 10F122 (2006)
129. Ivanov A A et al. *Rev. Sci. Instrum.* **71** 3728 (2000)
130. Davydenko V I *Rev. Sci. Instrum.* **68** 1418 (1997)
131. Davydenko V I, Ivanov A A, Shul'zhenko G I *Plasma Phys. Rep.* **41** 930 (2015); *Fiz. Plazmy* **41** 1004 (2015)
132. Listopad A A et al. *Rev. Sci. Instrum.* **83** 02B707 (2012)
133. Karpushov A N et al. *Fusion Eng. Des.* **66–68** 899 (2003)
134. Stupishin N V et al. *AIP Conf. Proc.* **1771** 050012 (2016)
135. Davydenko V I, Ivanov A A, Karpushov A N *Plasma Phys. Control. Fusion* **36** 1805 (1994)
136. Savkin V Ya, Lizunov A A *Rev. Sci. Instrum.* **88** 076109 (2017)
137. Zelenski A et al. *Rev. Sci. Instrum.* **73** 888 (2002)
138. Kolmogorov A V et al. *Rev. Sci. Instrum.* **85** 02A734 (2014)
139. Zelenski A et al. *Rev. Sci. Instrum.* **87** 02B705 (2016)
140. Belchenko Yu I, Dimov G I, Dudnikov V G *Zh. Tekh. Fiz.* **43** 1720 (1973)
141. Belchenko Yu I, Dimov G I, Dudnikov V G *Izv. Akad. Nauk SSSR. Ser. Fiz.* **37** 2573 (1973)
142. Belchenko Yu I, Thesis for Cand. Phys.-Math. Sci. (Novosibirsk: Budker Institute of Nuclear Physics, SB USSR Acad. Sci., 1974)
143. Belchenko Yu I, Dudnikov V G, in *3 Vsesoyuz. Soveshch. "Vzaimodeistvie Atomnykh Chastits s Tverdym Telom"* (All-Union Meeting "Interaction of Atomic Particles with a Solid") Pt. 3 (Khar'kov: Izd. KhGU, 1976) p. 180
144. Belchenko Y I, Dimov G I, Dudnikov V G, Preprint No. 77-56 (Novosibirsk: Budker Institute of Nuclear Physics, SB USSR Acad. Sci., 1977); in *Proc. Symp. on Production and Neutralization of Negative Hydrogen Ions and Beams, Brookhaven, 1977*; Preprint BNL 50727 (New York: BNL, 1977) p. 79
145. Dudnikov V G, Thesis for Doct. Phys.-Math. Sci. (Novosibirsk: Budker Institute of Nuclear Physics, SB USSR Acad. Sci., 1977)
146. Belchenko Y I *Rev. Sci. Instrum.* **64** 1385 (1993)
147. Bacal M, Wada M *Appl. Phys. Rev.* **2** 021305 (2015)
148. Kishinevskii M E, Preprint No. 76-18 (Novosibirsk: Budker Institute of Nuclear Physics, SB USSR Acad. Sci., 1976)
149. Geerlings J J et al. *Surface Sci.* **157** 151 (1985)
150. Los J, Geerlings J J C *Phys. Rep.* **190** 133 (1990)
151. Bender E D, Dimov G I, Kishinevskii M E, Preprint No. 75-09 (Novosibirsk: Budker Institute of Nuclear Physics, SB USSR Acad. Sci., 1975)
152. Bender E D, Kishinevskii M E, Morozov I I, Preprint No. 77-47 (Novosibirsk: Budker Institute of Nuclear Physics, SB USSR Acad. Sci., 1977)
153. Belchenko Y I, Dimov G I, Dudnikov V G *Sov. Phys. Tech. Phys.* **20** 40 (1975); *Zh. Tekh. Fiz.* **45** 68 (1975)
154. Dudnikov V, in *Proc. of the Foutrh All-Union Conf. on Charged Particle Accelerators, Moscow, 1974* Vol. 2 (Moscow: Nauka, 1975) p. 323
155. Belchenko Yu I, Savkin V Y *Rev. Sci. Instrum.* **75** 1704 (2004)
156. Dimov G I, Derevyankin G E, Dudnikov V G *IEEE Trans. Nucl. Sci.* **24** 1545 (1977)
157. Derevyankin G E, Dudnikov V G *AIP Conf. Proc.* **111** 376 (1984)
158. Belov A S et al. *Rev. Sci. Instrum.* **63** 2622 (1992)
159. Allison P W *IEEE Trans. Nucl. Sci.* **24** 1584 (1977)
160. Sidlow R et al. *Proc. of EPAC* **92** 1005 (1992)
161. Ehlers K W, Leung K N *Rev. Sci. Instrum.* **51** 721 (1980)
162. Mori Y et al. *Nucl. Instrum. Meth. Phys. Res. A* **301** 1 (1991)
163. Wengrow A B et al. *Rev. Sci. Instrum.* **69** 989 (1998)
164. Belchenko Yu I et al. *Pis'ma Zh. Tekh. Fiz.* **3** 693 (1977)
165. Belchenko Yu I, Davydenko V I *Rev. Sci. Instrum.* **77** 03B702 (2006)
166. Antsiferov V V et al., Preprint No. 88-116 (Novosibirsk: Budker Institute of Nuclear Physics, SB USSR Acad. Sci., 1988)
167. Antsiferov et al. *AIP Conf. Proc.* **210** 427 (1990)
168. Apolonskii A N et al. *Pis'ma Zh. Tekh. Fiz.* **6** 86 (1980)
169. Belchenko Yu I, Dudnikov V G, Preprint No. 78-95 (Novosibirsk: Budker Institute of Nuclear Physics, SB USSR Acad. Sci., 1978)
170. Belchenko Yu I, Dudnikov V G *J. Physique Coloq.* **40** C7-501 (1979)
171. Belchenko Yu I, Dudnikov V G, Preprint No. 80-34 (Novosibirsk: Budker Institute of Nuclear Physics, SB USSR Acad. Sci., 1978)
172. Belchenko Yu I, Dudnikov V G, in *Proc. XV Intern. Conf. on Phenomena in Ionized Gases* Pt. II (Minsk, 1981) p. 883
173. Belchenko Yu I *Sov. J. Plasma Phys.* **9** 703 (1983); *Fiz. Plazmy* **9** 1219 (1983)
174. Belchenko Yu I, Kupriyanov A S *Rev. Phys. Appl.* **23** 1889 (1988)
175. Kupriyanov A S, Thesis for Cand. Phys.-Math. Sci. (Novosibirsk: Budker Institute of Nuclear Physics, SB RAS, 1994)
176. Belchenko Yu I, Kupriyanov A S *Rev. Sci. Instrum.* **61** 484 (1990)
177. Belchenko Yu I, Kupriyanov A S *Rev. Sci. Instrum.* **65** 1179 (1994)
178. Belchenko Yu I, Dimov G I *Vopr. Atom. Nauki Tekh. Termoyad. Sintez* (1) 42 (1984)
179. Belchenko Yu I, Dimov G I *AIP Conf. Proc.* **111** 363 (1984)
180. Bashkeev A A, Dudnikov V G *AIP Conf. Proc.* **210** 329 (1990)
181. Belchenko Yu I, Kupriyanov A S *AIP Conf. Proc.* **287** 255 (1992)
182. Belchenko Yu I, Bacal M *Rev. Sci. Instrum.* **66** 1204 (1994)
183. Belchenko Yu I, Kupriyanov A S *Rev. Sci. Instrum.* **69** 929 (1998)
184. Belchenko Yu I, Grigoryev E V *Rev. Sci. Instrum.* **73** 939 (2002)
185. Belchenko Yu I, Savkin V Y *Rev. Sci. Instrum.* **75** 1704 (2004)
186. Belchenko Yu I et al. *Rev. Sci. Instrum.* **79** 02A521 (2008)
187. Ivanov A A et al. *Tech. Phys. Lett.* **42** 608 (2016); *Pis'ma Zh. Tekh. Fiz.* **42** (12) 1 (2016)
188. Belchenko Yu I et al. *AIP Conf. Proc.* (2018), to be published
189. Belchenko Yu I et al. *Rev. Sci. Instrum.* **77** 03A527 (2006)
190. Belchenko Yu, Sanin A, Ivanov A *AIP Conf. Proc.* **1097** 214 (2009)
191. Belchenko Yu I et al. *Rev. Sci. Instrum.* **85** 02B108 (2014)
192. Belchenko Yu I, Savkin V Ya *AIP Conf. Proc.* **1390** 401 (2011)
193. Belchenko Yu I, Sanin A L, Sotnikov O Z *Rev. Sci. Instrum.* **85** 02B116 (2014)
194. Belchenko Yu I, Sanin A L, Sotnikov O Z *Yad. Fiz. Inzhiniring* **6** (1–2) 1 (2015)
195. Ivanov A A et al. *Rev. Sci. Instrum.* **85** 02B102 (2014)
196. Belchenko Yu I et al. *Rev. Sci. Instrum.* **87** 02B316 (2016)
197. Belchenko Yu I et al. *Rev. Sci. Instrum.* **87** 02B120 (2016)
198. Abdrashitov G À et al. *AIP Conf. Proc.* **1655** 040002 (2015)
199. Belchenko Yu I et al. *Rev. Sci. Instrum.* **87** 02B119 (2016)
200. Belchenko Yu I et al. *Rev. Sci. Instrum.* **87** 02B133 (2016)
201. Ivanov A A et al. *AIP Conf. Proc.* **1771** 030012 (2016)
202. Dimov G I, Zakaidakov V V, Kishinevskii M E *Fiz. Plazmy* **2** 597 (1967)
203. Steward L D, in *Proc. of the 3rd Intern. Symp. on Production and Neutralization of Negative Ions and Beams, Brookhaven, 1983* p. 594
204. Logan B G et al. *Sov. J. Plasma Phys.* **4** 301 (1978); *Fiz. Plazmy* **4** 542 (1978)
205. Staten H Stanley, in *Proc. of the 3rd Intern. Symp. on Production and Neutralization of Negative Ions and Beams, Brookhaven, 1983* p. 587
206. Allison S K *Rev. Mod. Phys.* **30** 1137 (1958)
207. Tawara H, Russek A *Rev. Mod. Phys.* **45** 178 (1973)
208. D'yachkov B A *Zh. Tekh. Fiz.* **38** 1259 (1968)
209. Dimov G I, Roslyakov G V *Nucl. Fusion* **15** 551 (1975)
210. Dimov G I, Ivanov A A, Roslyakov G V *Zh. Tekh. Fiz.* **50** 2300 (1980)
211. Dance D F, Harrison M F A, Rundel R P *Proc. R. Soc. A* **299** 525 (1967)
212. Peart B, Walton D S, Dolder K T *J. Phys. B* **3** 1346 (1970)
213. Peart B, Walton D S, Dolder K T *J. Phys. B* **4** 88 (1971)
214. Fite W L, Brakmann R T *Phys. Rev.* **112** 1141 (1958)
215. Gilbody H B, Ireland J V *Proc. R. Soc. London A* **277** 137 (1964)
216. Hooper J W et al. *Phys. Rev.* **121** 1123 (1961)
217. Dimov G I, Ivanov A A, Roslyakov G V *Sov. J. Plasma Phys.* **6** 513 (1980); *Fiz. Plazmy* **6** 933 (1980)
218. Chaibi W et al. *AIP Conf. Proc.* **1097** 385 (2009)

219. Fink J H, Frank A M, Lawrence Livermore Nat. Lab. Report UCRL-16844 (1975)
220. Fink J H, in *Production and Neutralization of Negative Ions and Beams: 3rd Int. Symp., Brookhaven, 1983* p. 547
221. Vanek V et al., in *Proc. of the 3rd Int. Symp. on Production and Neutralization of Negative Ions and Beams, Brookhaven, 1983* p. 568
222. Kovari M, Crowley B *Fusion Eng. Design* **85** 745 (2010)
223. Simonin A et al. *AIP Conf. Proc.* **1390** 494 (2011)
224. Popov S S et al., in *Tezisy XLII Mezhdunarodnoi Konf. po Fizike i UTS* (Theses of the XLII Intern. Conf. on Plasma Physics and Controlled Thermonuclear Reactions) (Moscow: ZAO NTTs PLAZMAIOFAN, IOF RAN, 2015) p. 395
225. Popov S S et al., arXiv:504.07511
226. Kozlov V V, Treshchev D V *Billiardy. Geneticheskoe Vvedenie v Dinamiku System s Udarami* (Billiards. Genetic Introduction to Dynamics of Systems with Strokes) (Moscow: Izd. MGU, 1991) p. 168
227. Budker G I *Plasma Physics and the Problem of Controlled Thermonuclear Reactions* Vol. 3 (Ed. M A Leontovich) (New York: Pergamon Press, 1959) p. 1; Translated from Russian: in *Fizika Plazmy i Problema Upravlyaemykh Termoyadernykh Reaktsii* Vol. 3 (Ed. M A Leontovich) (Moscow: Izd. AN SSSR, 1958) p. 3
228. Popov S S et al., arXiv:1703.10777
229. Atlukhanov M G et al. *AIP Conf. Proc.* **1771** 030024 (2016)
230. Popov S S et al. *AIP Conf. Proc.* **1869** 050005 (2017)
231. Belchenko Yu I et al. *Rev. Sci. Instrum.* **61** 378 (1990)
232. Hemsworth R et al. *Nucl. Fusion* **49** 045006 (2009)
233. Popov S S et al. *AIP Conf. Proc.* (2018), in print
234. IPG.IRE-POLUS, http://www.ipgphotonics.com/ru/products/lasers/nepreryvnye-lazery-vysokoy-moshchnosti/1-mikron/yls-sm-110-kvt
235. Ivanov A A, Prikhodko V V *Phys. Usp.* **60** 509 (2017); *Usp. Fiz. Nauk* **187** 547 (2017)
236. Beklemishev A D *Fusion Sci. Tech.* **59** 90 (2011)
237. Yurov D V, Prikhod'ko V V *Phys. Usp.* **57** 1118 (2014); *Usp. Fiz. Nauk* **184** 1237 (2014)
238. Postupaev V V et al. *Fusion Eng. Des.* **106** 29 (2016)
239. Beklemishev A D *Phys. Plasmas* **22** 103506 (2015)